JIMMA UNIVERSITY

JIMMA INSTITUTE OF TECHNOLOGY

FACULTY OF MECHANICAL ENGINEERING

DESIGN OF MECHANICAL SYSTEMS STREAM

Multi-body Dynamic Modeling and Analysis of Wind Turbine Gearbox at Adama II Wind Farm

A THESIS SUBMITTED TO THE SCHOOL OF GRADUATE STUDIES OF JIMMA UNIVERSITY IN PARTIAL FULFILLMENT OF THE REQUIREMENTS FOR AWARD OF DEGREE OF MASTERS IN DESIGN OF MECHANICAL SYSTEMS.

BY: MEKDES TSEGAYE

Jimma, Oromia, Ethiopia

September 2021

JIMMA UNIVERSITY

JIMMA INSTITUTE OF TECHNOLOGY

FACULTY OF MECHANICAL ENGINEERING

DESIGN OF MECHANICAL SYSTEMS STREAM

Multi-body Dynamic Modeling and Analysis of Wind Turbine Gearbox at Adama II Wind Farm

A THESIS SUBMITTED TO THE SCHOOL OF GRADUATE STUDIES OF JIMMA UNIVERSITY IN PARTIAL FULFILLMENT OF THE REQUIREMENTS FOR AWARD OF DEGREE OF MASTERS OF SCIENCE IN MECHANICAL ENGINEERING.

(DESIGN OF MECHANICAL SYSTEMS)

BY: MEKDES TSEGAYE

Main Advisor: Prof. Hirpa G. Lemu

Co-Advisor: Addisu K/mariyam

Jimma, Oromia, Ethiopia

September 2021

DECLARATION

I, the undersigned, declare that this thesis entitled “Multi-body Dynamic Modeling and Analysis of Wind Turbine Gearbox at Adama II Wind Farm.” is my original work, and has not been presented by any other person for an award of a degree in this or any other University, and all sources of materials used for the thesis have been duly acknowledged.

Mekdes Tsegaye _____ _____

Name Signature Date

APPROVAL

As a member of the examining board of open defense, we have checked and evaluated the Master Thesis prepared and presented by Mekdes Tsegaye entitled "*Multi-body Dynamic Modeling and Analysis of Wind Turbine Gearbox at Adama II wind Farm*". Thus, we hereby certify that this work fulfills the requirement of the Degree of Master of Science in Mechanical Engineering (Design of Mechanical System).

1. Department Chairman: Mr. Iyasu Tafese (MSc)

Signature: _____ Date: _____

2. Main Advisor: Prof. Hirpa G. Lemu (PhD)

Signature: _____ Date: _____

3. Co-Advisor: Mr. Addisu K/Mariam (MSc)

Signature: _____Date: _____

4. Internal examiner:

Signature: _____Date: _____

5. External examiner:

Signature: _____Date: _____

STATEMENT OF THE AUTHOR

First, I declare that this thesis is my confide work and that all sources of materials used for this thesis have been duly acknowledged. This thesis has been submitted in partial fulfillment of the requirements of MSc. degree at Jimma Institute of Technology and is deposited at the University Library to be made available to borrowers under the rules of the library. I solemnly declare that this thesis is not submitted to any other institution anywhere for the award of any academic degree, diploma, or certificate.

Brief quotations from this thesis are allowable without special permission provided that accurate acknowledgment of the source is made. Requests for permission for extended quotation from or reproduction of this manuscript in whole or in part may be granted by the head of the major department or the Dean of the School of Graduate Studies when in his or her judgment the proposed use of the material is in the interests of scholarship. In all other instances, however, permission must be obtained from the author.

Name: Mekdes Tsegaye Reda Signature: ……

Place: Jimma Institute of Technology, Jimma

Date of Submission: ……

ACKNOWLEDGEMENT

Above all, I would like to thank the Almighty God for his immeasurable guidance in my entire life. I am indebted to many individuals for their encouragement and help while conducting this study. It is a pleasure to convey my gratitude to all of them. First of all, I thank my main advisor Prof. Hirpa G. Lemu for his support in all aspects of my research work. Equally, my gratitude goes to my co-advisor Mr. Addisu K/Mariam as he added valuable, and constructive comments for the successful accomplishment of the research work.

I am very grateful to the Jimma Institute of Technology for its provision of the necessary support and study leave. I highly appreciate the entire staff of Adama Wind Farm-2 for their special support during the data collection process.

This is a good opportunity to appreciate my family for their moral and material support in my stay at Jimma University since my undergraduate study. Moreover, my heartfelt thanks also go to my friends and work colleagues of JiT for the special support that they gave to me during my research work.

ABSTRACT

Wind turbines are the most developed renewable energy prospects that are used to capture kinetic energy from the wind and generate electricity. Modern large-scale wind turbines are subjected to different sorts of failures, such as main bearings, gearboxes, and generators. Moreover, downtime loss will make a huge impact on the cost of energy. Thus, the rapid development of the wind power industry requires a gearbox with higher performance. The dynamic characteristics of gearboxes study before and during the operation will decrease operation and maintenance (O&M) costs, both of which would greatly reduce the economic benefit of wind power. The study of dynamic characteristics of wind power gearbox works on the prevention of failures in the wind turbine. The existence and application of modeling and analysis software will reduce the task and increase the accuracy.

This thesis presents, the influence of variation of input rotational speed on the vibration signal of SE7715 wind turbine drive train at Adama Wind Farm II. The dynamic model of the gearbox transmission system is built into the ADAMS for simulation. The wind turbine gearbox vibration signal is simulated to monitor the technical conditions of rotating components at three different load cases with input rotational speeds at 10 rpm, 15 rpm, and 20 rpm. The gears vibration signal of angular acceleration and gear force are considered in the simulation and the results are analyzed through Fast Fourier Transform (FFT) by using ADAMS.

Depending on the simulation results, the vibration signal peak points of load case 3 (20 rpm) is greater than other load cases and these indicate the vibration signal is dependent on the variation of input rotational speed. As the rotational speed increases the vibrational signal also becomes higher. The results also show the influence of input rotational speed on the gear force at the three load cases, at the highest input rotation speed (20 rpm), the amplitude of gear force is higher than the other load cases and at 10 rpm input rotational speed, the amplitude is lower than other load cases. Therefore, input rotation variation has a great effect on vibration signal of gears and gear force.

KEYWORDS: Wind turbine**,** Dynamic analysis, Vibration signal, Fast Fourier Transform (FFT)

Table of Contents

List of Tables

List of Figures

Nomenclature

A	swept area
C_u	damping coefficient of gears
E	Modulus of elasticity
f_m	gear mesh frequency
I_u	moment of inertia of gears
K_u	time varying-mesh stiffness values of gears
m_u	mass of gears
N	number of teeth of gears
n	rotational speed
P	power
r	rotor radius
r_{bu}	base radius of gears
r_u	pitch radius of gears
T	period
v_d	dynamic transonic speed
v_s	static transonic speed
V_u	equivalent transverse displacement of gears
V_j	relative displacement of gear meshes

Acronyms

AC	Alternating current
ADAMS	Automatic dynamic analysis of mechanical systems
MBD	Multibody dynamics
DOF	Degree of freedom
FFT	Fast Fourier transform
FMM	Finite element modeling
GMF	Gear mesh frequency

GWEC	Global wind energy council
I3	Index3
LPM	Lumped parameter modeling
MD	Multidisciplinary
NVH	Noise, vibration, and harshness
PGT	Planetary gear train
SI1	Stabilized index 1
SI2	Stabilized index 2
WT	Wind turbine

Greek Letters

α	Pressure angle
β	Helix angle
θ_u	Angular displacement of gears
μ_d	Dynamic friction coefficient
ξ	Damping
ρ	Density
τ	Torque
υ	Poison's ratio
ω	Rotational speed

CHAPTER ONE

1. Introduction

1.1 Background

Energy plays a great role in human existence immediately after air, food, shelter and it is also one of the necessities for socio-economic development. This development has changed people's way of life and these changes forced people to extract energy from the existing renewable and non-renewable energy sources [1]. In addition, for the greenhouse effect, global energy crisis, and environmental disasters, there is a worldwide agreement about the development of new and renewable energy. These sources include solar energy, wind energy, geothermal energy, and so on. In the past three decades, wind energy has become the most cost-effective of all currently exploited renewable energy sources [2].

In ancient times, people were fascinated by the wind energy source to use it in their sailing boats on the River Nile. Its first application as a force driving a windmill is estimated in the 7th century A.D. Windmills were used for grinding grain and for pumping water, the horizontal-axis windmill with a rotor perpendicular to the wind direction is believed to be the most widespread type from those ages. Therefore, the usage of windmills became a major source of power since the 14th century. Then the mature windmill design led to increased use of wind energy in the United States from the mid-19th century. Finally, at the end of the 19^{th} century, electricity arose and interest increased in using wind power for its generation. The windmills connected to an electric generator are further called wind turbines [3].

From around 1990, the main driver for the extraction and use of wind turbines was to generate electrical power to lower CO_2 emissions and to help in the climate change. Then from around 2006 the very high oil price and concerns over the security of energy supplies led to a further increase of interest in wind energy and a succession of policy measures were put in place in many countries to encourage its use. In 2007 the European Union declared a policy that 20% of all energy should be from renewable sources by 2020 [1].

Wind energy is one of the most developed renewable energy prospects. The world's wind power industry developed rapidly in recent years, and the total wind power capacity reached 432 GW by the end of 2015. Chinese wind power capacity increases rapidly and becomes the largest one all

over the world. By the end of 2015, the total installed capacity reached 145 GW, accounting for 33.6 % of the world's wind power capacity [4].

The world is using the resource either onshore or offshore to generate electricity. Wind energy has been the fastest-growing renewable energy source in the world for some time. At the end of 2018, the global total wind energy capacity had grown to approximately 590 GW, which is enough to cover about 4% of the world's total electricity. The total global installed capacity of wind turbines during 2001-2018 is shown in the below Figure 1.1.

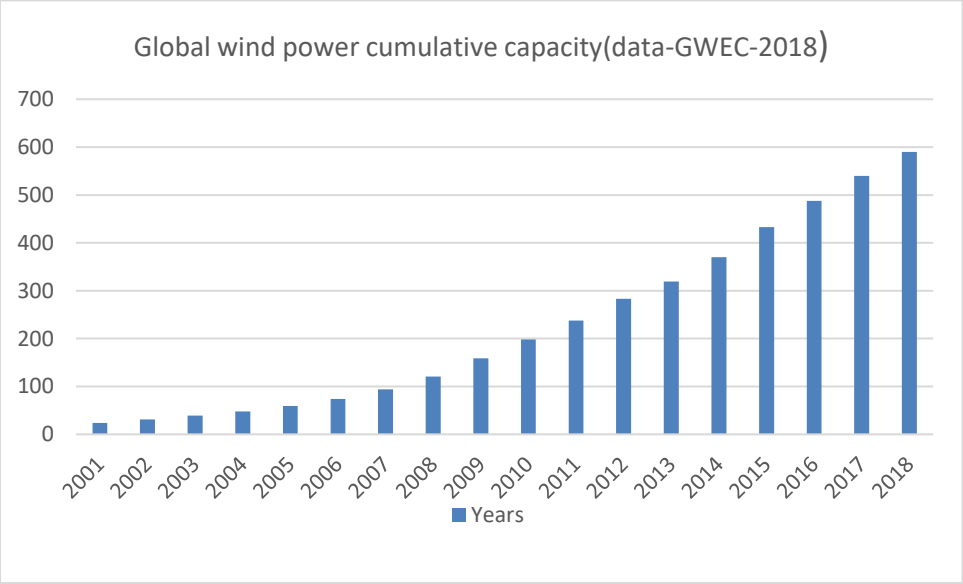

Figure 1.1 Global cumulative installed wind capacity 2001-2018(GWEC-2018)

The world's wind power industry developed rapidly in recent years, in this rapid growth five leading countries were having the major share of the world capacity of wind turbines and wind power i.e., China, USA, Germany, Spain, and India; together they represent a total share of more than 70 % of the global wind energy potential. The global Wind Energy Council (GWEC) released its 2018 report till the end of December; the top ten countries with maximum cumulative wind energy and Chinese wind power capacity increases rapidly and becomes the largest ones all over the world. By the end of 2018, the total installed capacity reached 145 GW (GWEC-2018).

Being dependent on the imported petroleum is also insufficient to fill the gap between the demand and supply of the electrical power of a nation since it costs foreign currency and also the sources of the non-renewable energy are expected to deplete in decades. In contrast, the number of industries is always increasing from time to time, thus a single watt of energy plays a difference in the supply grid system.

A wind turbine is a variable dimension machine, depending on how much energy is desirable. This system is used to complete the electricity produced at an electric power plant/station or for autonomous consumption. Generally, a modern wind turbine consists of three main parts: a rotor on a horizontal axis, a nacelle, and a tower. The unwanted motions that occurred, in one of these parts, are transmitted to the other by the relative motions between the mechanical components such as shafts, gears, bearings… Particularly, in the wind generator, the vibrations originate from the gearbox situated in the nacelle. These unwanted motions are produced when gears and bearings are subjected to irregular loads and when some components are not sufficiently rigid [5].

To come up with the maximum output of the wind energy from a wind farm, since the wind speed is dynamic, dynamic analysis of wind turbine gearbox is crucial to the success of wind energy efficiency. At the time being, due to the unavailability of an experimental laboratory and to save time, the wind turbine gearbox dynamic analysis is conducted in computer programs, which are specifically designed to simulate accurate predictions. Specialized multibody dynamics software like ITI-SIM, SIMPACK, LMS Virtual. Lab Motion and MSC ADAMS allow modeling three-dimensional gear bodies, tooth microgeometry, global and local tooth stiffness [6]. Among the computer programs, MS-ADAMS (Automatic dynamic analysis of mechanical systems) is the most commonly used tool for dynamic modeling and analysis of multi-body systems. ADAMS is a computer program for simulating multi-body dynamics.

This dynamic analysis of wind turbine gearbox using ADAMS will greatly accelerate and facilitate Wind Farm development and prevents early-stage failures. This will present detail about the effect of naturally variable wind speed effects on the gearbox of a wind turbine.

In this Thesis, the data collected from the Adama II site Wind Farm will be used to formulate a multibody dynamic model and simulate the dynamic analysis of the gearbox by ADAMS. The dynamic characteristic of the SANY SE7715 wind turbine gearbox was analyzed under different external excitation conditions (wind speed).

1.2 Problem Statement

Due to the harsh environment, modern large-scale wind turbines are subjected to different sorts of failures, such as main bearings, gearboxes, and generators. Moreover, downtime loss will make huge impact on the cost of energy. Thus, the rapid development of the wind power industry requires a gearbox with higher performance. If the dynamic characteristics of gearboxes are not studied before, and after the operation, the actual utilization of wind turbines will decrease and

operation and maintenance (O&M) costs will increase, both of which would greatly reduce the economic benefit of wind power.

In the meantime, the Ethiopian government is engaged in a variety of projects to generate electrical energy. The electrical energy generated from the abundant wind resource has got an emphasis to fill the gap between the supply and the demand across the country. These projects incur huge capital and require foreign currency; thus, a reasonable study shall be done before and after investing huge capital and human resource. The study shall be carried out with the latest technology and materials to come to a feasible result.

However, it is quite difficult and time taking to undertake the estimation manually. The existence and application of modeling and analysis software will reduce the task and increase the accuracy. As an example, Fig. 1.2 (a) shows the failure statistics of Chinese wind turbines from January 2011 to August 2011, in which 23,600 machine parts have suffered failures in operation and it happened more than 40,000 times. It is also well known to be a similar situation in Europe and North America, including some famous companies. As shown in Fig. 1.2(b), among other failures, massive problems belong to the core parts of the energy transmission chain, i.e., inside the gearboxes and the rotor systems [4]. Since, the gearbox is the major component, the operating of which directly affects the normal operation of wind power system, and therefore, it is of great significance to carry out the dynamic characteristics of wind turbine gearbox because its failure has been the major cause of many reliability problems for the modern wind energy industry since its inception [7].

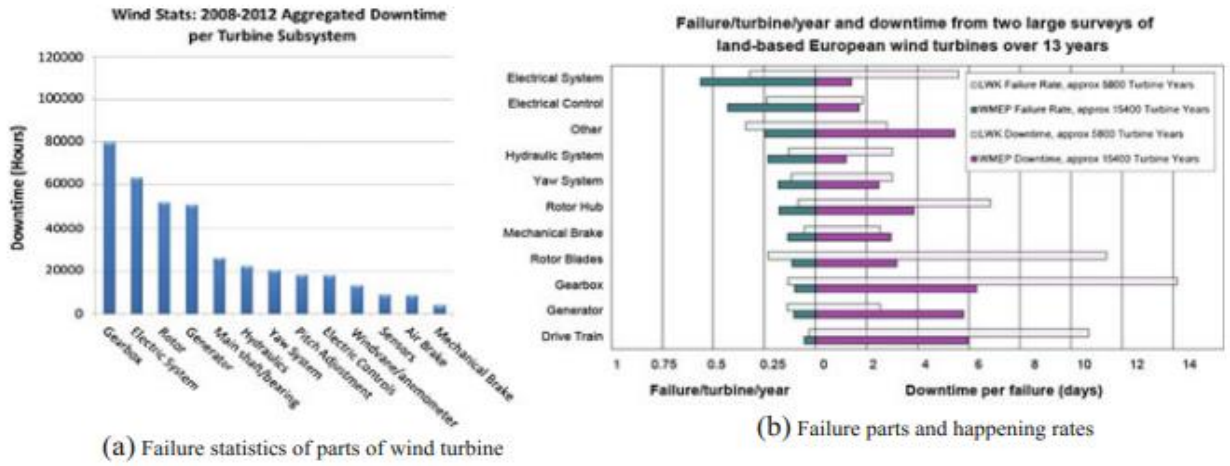

Figure 1.2 Failure statistics of wind turbines [4]

It has been also reported that gearbox failures account for the largest amount of downtime, maintenance, and loss of power production. Reports from wind turbine industries in Germany indicate that these costly failures of gearbox and its components can total 15-20% of the price of the turbine [8].

As described above, the gearbox transmission system is one of the mechanical systems where mechanism dynamic modeling and simulation is important because wind turbine components are always affected by uncertain (stochastic) loads in nature. Due to these loads, the chances of failures are higher for critical components, such as a gearbox. Among other areas, the gearbox in wind turbines is commonly known to be the weakest link because it is exposed to highly dynamic and variable loads [9].

In Adama Wind Farm II, the wind turbine's performance should have to be understood before any catastrophic failure happen, analyzing the dynamic characteristics of wind turbine gearbox components before and after installation is an important procedure to maximize energy production by preventing pre-failure.

1.3 Objectives of the study

The main objective of this project is to analyze the multi-body dynamics of the gear train system for the wind turbine gearbox under dynamic loads at the Adama II site.

The specific objectives of this thesis

- To formulate a mathematical model for the planetary gear train system of wind turbine gearbox by using lumped-mass parameter modeling
- To demonstrate the impact of input rotational speed variation on the acceleration and angular acceleration vibration signal of all gears by using MSC ADAMS software
- To analyze the influence of input rotational speed variation on the dynamic gear force by using MSC ADAMS software and
- To analyze angular acceleration and gear force vibration signals of all gears by Fourier transform

1.4 Significance of the study

Ethiopia without its gas or oil reserves is turning to its significant renewable energy potential to fuel its economic development including damming the Blue Nile and the southern Omo River. However, the flow of the region's rivers is subject to rainfall that is erratic to make hydropower less reliable than other sources of clean energy. Ethiopia has an abundance of hydroelectric energy sources, but during the dry season and when droughts happen the level of the dam decreases so that the wind turbines are immune to the dry spells.

Since, the downtime and cost associated with the gearbox of a wind turbine is high, studying the dynamic characteristics of the gearbox decreases the pre-failure of the gearbox components. It can help to understand gearbox dynamics. In addition, the cost to do dynamic simulation is negligible compared with that of doing experiments. Hence, the study of dynamic characteristics of wind power gearbox works on the prevention of failures in the wind turbine.

1.5 Scope and limitation

This research work mainly focuses on the dynamic analysis of the most affecting external excitation force on the wind turbine gearbox by ADAMS. There are two types of excitations low-frequency excitation and high-frequency excitation. The low-frequency excitation is due to wind fluctuations and the high-frequency excitation is due to static transmission. And in this thesis work, low-frequency excitation is considered. Wind speed causes external (low-frequency) excitation fluctuation.

The considered input rotational speeds are 10 rpm, 15 rpm, and 20 rpm. The work only focuses on finding the effect of rotational speed variation on the vibrational signal of the planetary gear, and the speed-up gear train. Then a comparison between the effects of rotational speed difference has been made. The multi-body dynamic simulation in this work doesn't consist of the changes in the internal excitation forces' effect on the gears and bearings. And it also doesn't contain environmental factors such as humidity because of it needs experimental verification.

1.6 Structure of the study

Following this introduction, the thesis is divided into six sections. The second chapter presents literature reviews on the wind turbine components, multi-body modeling analysis, lumped parameter modeling method & analysis of the gearbox by ADAMS software. Chapter Three

presents the methodologies of this thesis including the study design, study area, study variables, data collection, processing, and analysis, describes multi-body models, and the methods followed on ADAMS. Then under Chapter Four detailed mathematical model of the gearbox is presented. Chapter Five presents the results of the model by ADAMS software. Chapter Six presents vibration signal analysis through Fourier transform along with a discussion leading to the conclusion and recommendation part in Chapter Seven.

CHAPTER TWO

2. Review of Relevant Literatures

2.1 Wind turbine drivetrain concepts

A wind turbine consists of a turbine rotor, a gearbox, a generator, a power electronic system, and a transformer for grid connection, as shown in Fig 2.1, in which wind turbines capture the power from wind through turbine blades and convert it to mechanical power. Since wind speed is mostly lower, the gearbox is important to be able to convert its lower speed to the higher rotating speed into the generator, whose gearbox plays the role of accelerator [10].

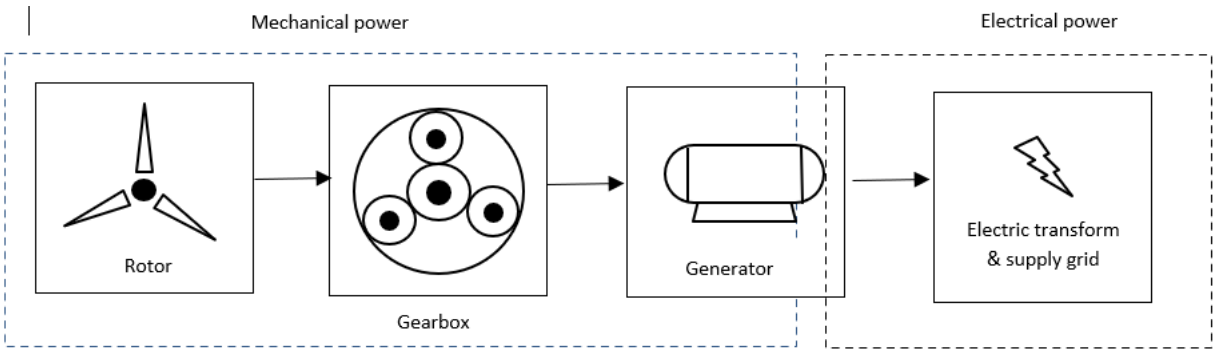

Figure 2.1 General composition of a wind turbine [10]

A Wind turbine is a variable dimension machine, depending on how much energy is desirable. This system is used to complete the electricity produced at an electric power plant/station or for autonomous consumption. It consists of three main parts: a rotor on a horizontal axis, a nacelle, and a tower [5].

Fig 2.2. Presents in detail a modern wind turbine and a cross-section through its nacelle. The nacelle of a wind turbine refers in general to all the components installed on top of the tower, except for the rotor blades and the rotor hub. The nacelle enclosure protects these components against rain, dust, salt, and other harmful particles or objects in the air. All components are connected to a bedplate [3]. The rotation of the support frame around the longitudinal axis of the tower is called “yawing” and is driven by the yaw drives. These drives turn the complete nacelle in the yaw bearing and keep the rotor always directed towards the wind.

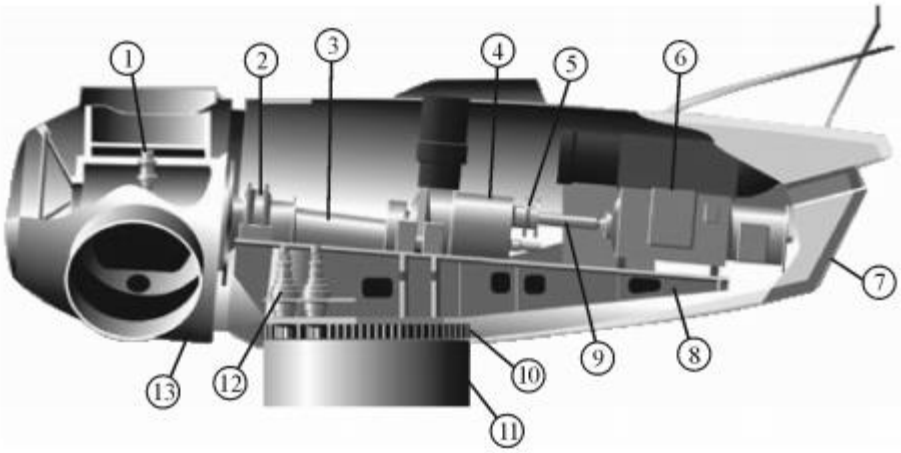

Figure 2.2 Wind turbine nacelle [3]

1. Pitch drive 2. Main bearing 3. Main shaft 4. Gearbox 5. Brake disk
6. Generator 7. Nacelle enclosure 8. Bedplate 9. Coupling 10. Yaw bearing
11. Tower 12. Yaw bearing 13. Rotor hub

The generator is part of the drive train in a wind turbine and generates usually a three-phase alternating current (AC), this current goes through a transformer which raises the voltage to the level required by the local electrical grid. Generally, the wind turbine drivetrain converts high torque on the main shaft to low torque on the high-speed shaft to meet the electromechanical requirements of the generator [7].

2.2 Structure Description of Gearbox in Wind Turbine

The structure of the gearbox in a wind turbine depends on the type of generator and the size of power needed. For a small power wind turbine, a conventional gear set is most preferable, as shown in Figure 2.3 (a) two stages gear set, due to it is simple structure and lower manufacturing cost. For medium power, however, megawatt level wind turbine, single-stage PGT, and multi-stage PGT, or combined PGT with conventional gear set, as shown in Figure 2.3 (b), (c), (d), (e), are usually applied in the wind turbines, because PGT offers the advantage of compactness and large load capacity. A new configuration of gearbox compound epicycle gear train combined a deferential gear train with a star wheel shown in Figure 2.3 (f), is created, which can raise the power density greatly due to the configuration with closed PGT and multi-planet gears have the characteristic of power divided [10].

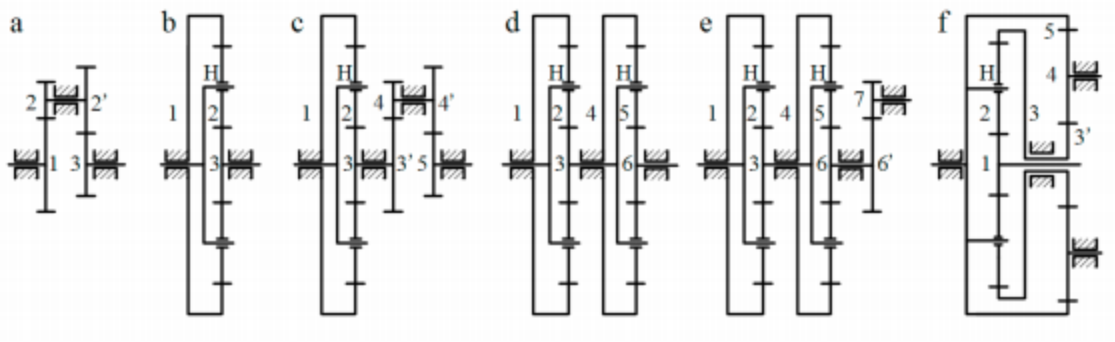

*Figure 2.3 The configuration of gear boxes (a) 2 conventional gear set; (b) 1 PGT; (c) PGT and 2 conventional gear set; (d) 2 stage PGT; (e) 2PGT and 1 conventional gear set; (f) compound epicycle gear tr*ain [10]

Qingkai et al. also mentioned three types of gearboxes used in wind turbines, such as cylindrical gearboxes, planetary growth boxes, and combined gearboxes. The wind turbine gearbox is mainly composed of the housing shell, gear pairs, shafts, and bearings. The housing shell of the gearbox should be sufficiently rigid to withstand the forces without deformation. The gears and the shafts are important in the transmission chain of a wind turbine [4].

2.3 Modeling Methods for Dynamic Analyses

Many researchers focus on the dynamics of the gear transmission system. Zhu et al. show how the dynamic performance of a megawatt wind turbine drive train significantly influences the operation of an entire machine by subjecting it to theoretical and experimental dynamic analysis [11].

Najad et al. states that the dynamic behavior of wind turbine gearbox is determined using three techniques namely pure torsional, rigid multi-body modeling, and flexible multi-body modeling. And when the number of planet gears is greater than three, planetary gears can have unequal load sharing among themselves [12].

2.3.1 Pure Torsional Modeling and analysis

Joris et al. presented 3 types of multibody models for the investigation of the internal dynamics of a drive train in a wind turbine. The first approach was limited to the analysis of torsional vibrations only. They also presented a rigid multibody model with a special focus on the representation of the bearings and gears in the drive train. This generic model implementation can be used for parallel as well as planetary gear stages with both helical and spur gears. And they also offered some examples for different gear stages that describe the use of the presented formulations [13].

Todorov et al. were established a dynamic multi-body model where the wind turbine includes a rotor, a drive train, and an electrical generator. The drive train has a three-stage gearbox which

contains two high-speed parallel gear stages and a low-speed planetary gear stage. The model consists of 10 bodies and has 8 degrees of freedom taking into account the stiffness of the engaged tooth pairs. In this model, the aerodynamic torque is applied as an external load. The calculation permits obtaining natural frequencies, mode shapes, time series of torsional oscillations, and amplitude-frequency characteristics for an industrial wind turbine. Their results show that transient loads in the gearbox are very high and need special attention [14].

Xing and Moan examined in detail the modeling and analysis of an important wind turbine gearbox component, the planet carrier, in a multi-body setting. The planet carrier studied in this work comes from the 750kW wind turbine gearbox. There results from this comprehensive study provide an insight into the proper modeling of a wind turbine planet carrier in a multi-body setting [15]. Jin et.al were also assessed the gearbox dynamic behavior through three multibody models based on modal and dynamic behaviors. Three gearbox models of different complexity are presented, i.e., torsional rigid multi-body model, 6-DOF rigid multi-body model, and flexible multibody model [12].

Daneshi et al. presented a dynamic model of a single-stage planetary gearbox. The model includes non-linearities such as time-varying mesh stiffness, transmission error, and damping force. Simulation results clearly show that electromagnetic torque and stator current of generator contains mesh and rotating related frequencies of the gears in its spectra [16].

Li and Chen presented a method to simulate a wind turbine gearbox system with the multi-body drivetrain dynamic analysis software. The dynamic performance of the wind turbine gearbox is very important for measuring the integrated vibration and noise of the whole drivetrain system of a wind turbine [17]. Al-Hamadani et al. were also presented system modeling of dynamic loads experienced by key mechanical components within wind turbine gearbox under different operational conditions by using MATLAB/Simulink. Two operational conditions of WTs are considered; normal operation and shutdown, using torque spectrums measured from a field operating wind turbine. The torsional dynamic loads under these conditions differ significantly; during normal operation, the maximum torque ratio is below the recommended value however it exceeds the recommended level during a shutdown [18]. Helsen et al. focus on the gearbox modal behavior assessment using three more complex modeling techniques of varying complexity: the purely torsional model, rigid six degrees of freedom with discrete flexibility, and flexible multibody technique. They discussed both simulation and experimental results. Furthermore, the

interaction between the structural modes of the planet carrier, and planetary ring flexibility with the overall gearbox modes is investigated, resulting in the definition of two new mode categories: the planet carrier modes and planetary ring modes [19].

Zhu et al. also proposed the drive train of a megawatt wind turbine dynamic model in which the blades, the hub, the main shaft, and the speedup gearbox are assumed as flexibilities. The external excitation due to the measured load spectrum and the internal excitations due to the time-varying mesh stiffness, the transmission errors, and the meshing impacts within the gearbox are considered to predict the dynamic response of the system. Results show that the most vibration energy occurs at the speed-up gearbox, followed by the generator, and then the main shaft. An experimental remote real-time system is developed to monitor the vibration performance of the drive train, with which the accelerations of components are detected. The experimental results are following the theoretical results [20].

2.3.2 Rigid Multi-body Modeling

Zhai et al. show a key component to adjust the speed and torque, Considering the base helix angle, normal pressure angle, position angle, rotation of carrier, and the mesh of the ring gear and planet gear, a coupled dynamic model for high-power wind turbine gearbox transmission system, which consists of two helical planetary stages and one helical gear stage was established using the lumped parameter method. By using the numerical integration method, the results show that the modal frequencies for the system do not coincide with the gear mesh frequencies of the stages. Then, the dynamic mesh forces of the 1st stage in different models are compared and analyzed in the frequency domain. Finally, a comparison of two different modeling techniques are discussed for a wind turbine's drive train with a helical parallel gear stage and two planetary gear stages [21].

For wind turbine gearbox dynamic analysis, Zhao and Ji also studied the dynamic response under different excitation conditions. They proposed a 4 degree-of-freedom (DOF) dynamic model, both the external excitation due to wind and the internal excitation due to the static transmission error were included to represent the gearbox excitation conditions. With the help of the time history and frequency spectrum, the dynamic responses of wind turbine gearbox components are investigated by using the numerical integration method. Furthermore, they observed that the external excitation fluctuation has a large influence on the dynamic responses of both the gears and bearings [7]. Zhao and Ji did this analysis again for the wind turbine gearbox having two planetary gear stages and one parallel gear stage. They found the static transmission error has the least influence [22].

2.3.3 Flexible Multi-body Modeling

Yi et al. show the coupled dynamic model, which contains helical gears-shafts-bearings for a wind turbine gearbox transmission system, was built by considering nonlinear factors of the time-varying mesh stiffness, the external varying load, and the dynamic transmission error. These results provide useful theoretical guidelines for the design of parallel shaft gear systems in wind turbines [23]. Tan et al. also show a rigid-flexible coupling dynamic modeling method and an experimental method to study the modal characteristics of the doubly-fed wind turbine drivetrain at start-up. The proposed model is validated by professional software. The proposed method can be used to guide the drivetrain optimization and the experiment [24].

Bruce et al. developed a multibody dynamic gearbox model, used to determine maximum bearing contact stresses from laboratory-measured shaft torque data during normal operation and shutdown conditions. During normal operation, the maximum contact stress experienced by the planetary stage bearings exceeded recommended levels by 1% and during shut down by 15%. High-speed shaft bearings also exceeded recommended levels during shut down by 18% [25].

Jin et al. assessed the gearbox dynamic behavior through three multibody models of varying complexity, which are assessed based on modal and dynamic behaviors. This work shows that the fully flexible multibody dynamic model can better reflect the operating condition of the wind turbine. However, due to high calculation precision, the fully flexible multibody dynamic model consumes much time [9].

2.4 Multi-body dynamic modeling

As Najad et al. described, a multi-body dynamics system consists of solid bodies, or links, that are connected to each other by joints that restrict their relative motion. I.e. it studies the dynamic behavior of interconnected rigid or flexible bodies, each of which may undergo large translational and rotational displacements. The MBS model is a powerful tool for the load and dynamic response analysis of mechanical systems. A multi-body system is a collection of rigid or flexible bodies connected by joints/constraints and has relative motion between them. Its components are joints, force elements, global/local reference frame, points, markers (location and orientation of an entity), rigid/flexible bodies, and motion [12].

Shi et.al also defined multibody dynamic modeling as the study of the motion of mechanical systems caused by external forces and motion excitations acting on systems. Multibody dynamics

techniques are commonly used to analyze the component loads in general dynamic systems [26]. Dariusz & Natarajan mentioned lumped parameter modeling (LPM) and finite element modeling (FMM) are two commonly used techniques to model gear trains. A lumped parameter model is one in which the components are considered to be solid with the masses concentrated at a set of points. A finite element model discretizes a physical model into disjoint components of simple geometry called finite elements and its system response is obtained by connecting or assembling the collection of all elements [8].

A defining characteristic of all these systems is that they can undergo large overall motion that is comparable to their dimensions. A mechanism constitutes a set of bodies/parts connected or constrained with each other to perform a specified action under the application of force, torque or motion. Multibody dynamic analysis and finite element analysis are used to analyze a system. Their difference is,

Table 2-1 Difference between MBD and FEA

MBD	FEA
System performance, like forces, a, v, T of joints	Structural performance
The system is a usable collection of modeling entities	The system is a coordinate system
Abstract visualization	Precise visualization
Faster	Comparatively slower
Result accuracy is independent of mesh size	Result accuracy is proportional to mesh size
Simple (mass, inertia, CG)	Complicated (general mesh)

2.4.1 Equations governing MBD simulation

The equation of motion is used to describe the dynamic behavior of a multibody system. Each multibody system formulation may lead to a different mathematical appearance of the equations of motion while the physics behind is the same. The motion of the constrained bodies is described using equations that result basically from Newton's second law of motion. The equations are written for a general motion of the single bodies with the addition of constraint conditions.

2.4.2 Multibody dynamic simulation types

There are some types of MBD simulation such as Kinematic simulation, dynamic simulation, static simulation, quasi-static simulation, linear simulation, and complex simulation.

Kinematic simulation: A model with zero DOF is defined as kinematic and position, velocity, and acceleration analyzed through a purely geometric study. Its solutions are uncoupled displacement, velocity, and acceleration. Motion specified needs to be time-based and forces calculated as a consequence of motion. The non-linear algebraic equations solved by Newton-Raphson and the solution of differential equations are relatively robust. Its application is in mechanism design, robot design & task planning, cam profile design.

Dynamic simulation: It is a study of a system as a consequence of applied forces and applies to models with one or more DOF. In a dynamic simulation solution, the applied force affects acceleration, the accelerations are integrated to velocities, the velocities are also integrated to give displacements. Its improving product function and quality across a wide range of industries.

Static simulation: It is a study of the equilibrium conditions of a system at rest. In the static simulation, the system velocities and accelerations are zero, solve the static force balance problem and governing equations are algebraic. Its application is to calculate the force on the system at rest.

Quasi-static simulation: It is the study of the equilibrium conditions of a slowly moving system. In this type of simulation, forces are a function of time or there are motion inputs, velocity and inertia forces are ignorable, solve the static force balance problem at each point in time, and the governing equations are algebraic. It uses in suspension design, stability analysis, steady-state simulations, and so on.

Linear simulation: It is the study of the vibration modes of a system at any operating point and evaluation of the system transfer function at any specified operating point. Linear simulation linearizes equations of motion at a point and solves the eigen value problem to obtain system frequencies and mode shapes. Its application areas are stability analysis, Noise vibration and harshness (NVH), plant models for control system design, etc.

2.4.3 Multi-body dynamics modeling in MD ADAMS

S. Ana mentioned MSC Software as the worldwide leader of multidiscipline simulation solutions that help companies improve quality, save time and reduce costs associated with designing and testing manufactured products. MSC Software works with thousands of companies worldwide to develop better products faster with simulation technology, software, and services. Using this toolkit solution, design engineers achieve higher accuracy during predictive simulations of system

dynamics and loading of components. The results include the total force, the loading of the elements, and their loading conditions [27].

ADAMS is a powerful multidisciplinary (MD) modeling and simulation environment that was developed to build, simulate, refine and optimize diverse mechanical systems [28]. The basic code was originally developed at the University of Michigan with an ADAMS/solver product that solves nonlinear numerical equations from models in text format. Further developments included other modules that allow users to build, simulate and examine results in a single environment. As any simulation tool, ADAMS has a postprocessor module known as Adams/View having a graphical user interface for general modeling. Using this module, it is possible to plot the results and carry out, among others, Fourier analysis on the results. The software package (ADAMS) is getting a wide application and research interest because it represents one of the powerful tools for the implementation of the virtual prototyping process based on the process depicted in Figure 2.4.

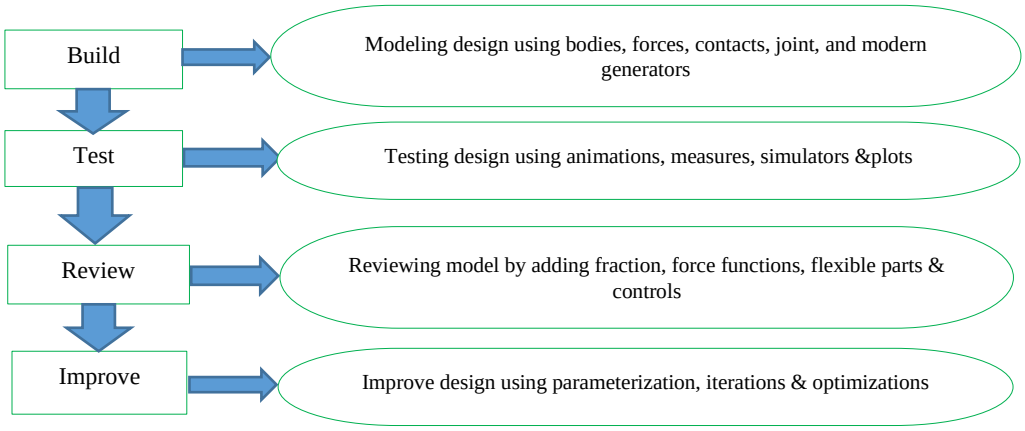

Figure 2.4 The virtual prototyping process in ADAMS

2.5 Literature summary

This chapter reviewed several past works on wind turbine gearbox dynamic analysis including wind turbine drivetrain concepts, the structure of wind turbine gearbox, pure torsional dynamic analysis, rigid multi-body dynamic analysis, and flexible dynamic analysis. Many researchers have been worked on the impact of internal and external excitation forces on the dynamic characteristics of gearbox components found in different types of gearboxes by using different types of software. Therefore, for wind turbine gearbox dynamic analysis, the internal excitation forces have the least influence and observed that the external excitation fluctuation has a large influence on the dynamic responses of both the gears and bearings.

2.6 Research Gap

Taking the above literature concepts into consideration, this thesis aims to conduct a dynamic analysis of the Adama wind turbine gearbox at external excitation force by using MSC ADAMS software. The developed 3D model of the gearbox is simulated by motions and forces and the observed dynamic responses are discussed and analyzed through Fourier transform.

Some gaps are identified based on which aim for further study has been decided. Some are

- Most of the researches are worked for internal and external excitation force influence comparisons and there are less works done on variation of external excitation force.
- Most of the researches are also worked for the application of the specific areas and there is no dynamic analysis worked on the Adama wind turbine gearbox performance.
- Insufficient work has been done on the Adama wind farm mechanical gearboxes.

CHAPTER THREE

3. Methodology

3.1 General methodology

The general methodology used in this thesis is given in the flow diagram in Fig. 3.1.

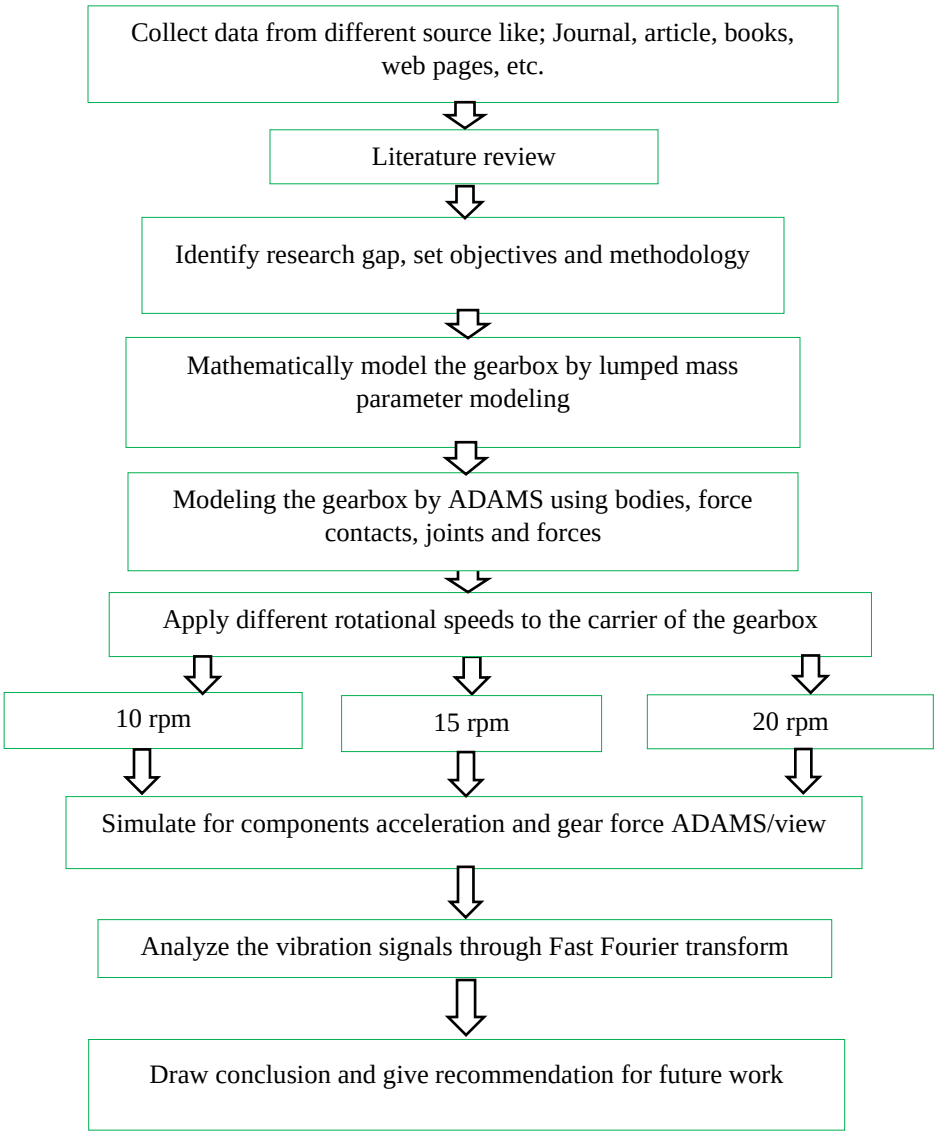

Figure 3.1 Flow diagram of thesis methodology

3.2 Study area

Adama, also known as Nazareth, is a city in central Ethiopia and the previous capital of the Oromia Region. Adama forms a Special Zone of Oromia and is surrounded by Misraq Shewa Zone. It is located at 8.54°N 39.27°E at an elevation of 1712 meters, 99 km southeast of Addis Ababa.

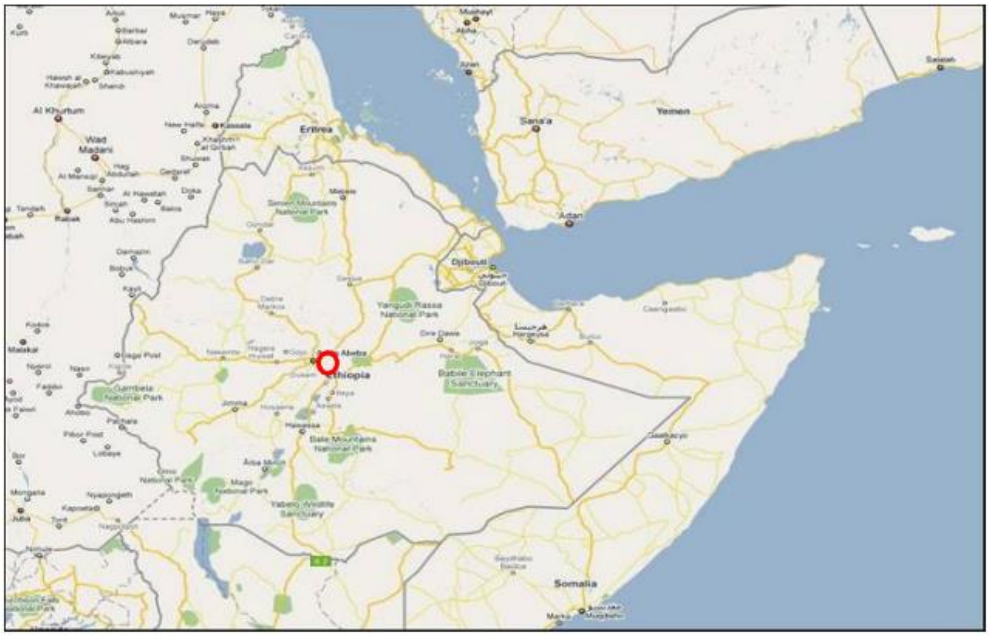

Figure 3.2 Adama Wind Farm [1]

The 153 MW Adama wind farm is the largest in sub-Saharan Africa to date. As shown in Fig. 3.2, there are 102 wind turbines with 70 m high Chinese-built turbines are situated in a range of rocky hills in the Ethiopian highlands in the southeast of the capital Addis Ababa [29].

3.3 Specifications of Adama wind turbine gearbox

In principle, one single wind turbine gearbox could be designed for one specific site. However, this would not lead to a cost-efficient production of wind turbine gearboxes. Therefore, wind turbine gearbox manufacturers offer in general a limited range of products suitable for a broad range of sites. The specifications of each of these wind turbine gearboxes are a summary of the requirements at different sites. However, the generalization of the designs has also limitations.

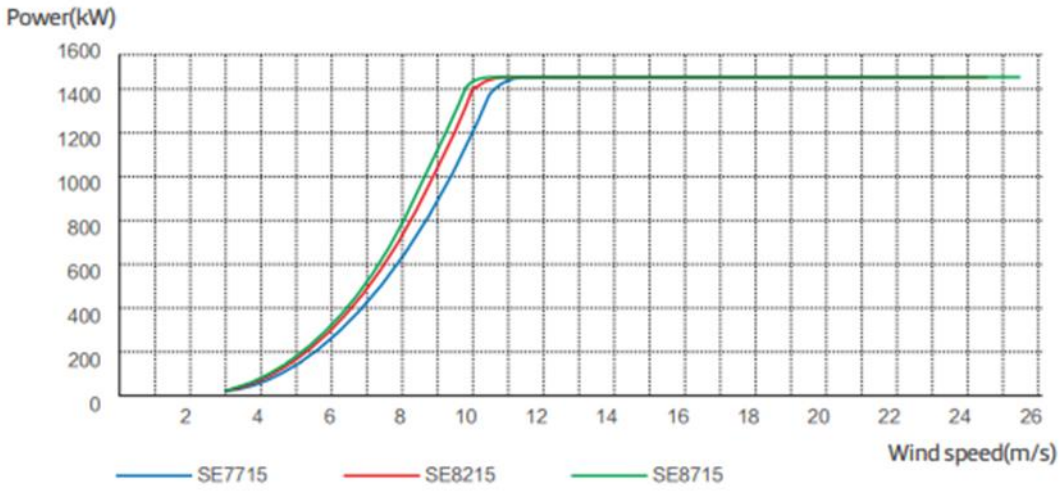

Figure 3.3 Power Curve [30]

The above Fig. 3.3 shows the power curve of three wind turbines which are found in the Adama wind farm. All wind turbines produce about 1.5 MW. The selected wind turbine is SE7715 and its technical specifications are given in Table 3.1.

Table 3-1 Technical specifications of gearbox

Model	SE7715
Wind class	IEC 2
Rated power (kW)	1500
Rotor diameter (m)	77.7
Swept area ($\boldsymbol{m^2}$)	47.36
Rated speed (rpm)	19
Rated wind speed (m/s)	11.5
Cut-in wind speed (m/s)	3
Cut-out wind speed (m/s)	25
Hub-heights (m)	67/70/80
Rotor weight (t)	33
Nacelle weight (t)	56

3.4 Study variables

In this thesis, the analysis will be conducted for different wind conditions such as 10 rpm, 15 rpm, and 20 rpm. The dependent variables are the gear forces, acceleration, and angular acceleration. Generally, vibrations consist of vibration signals in three axes – x, y, and z. The basic parameters which are calculated for vibrations are trajectory, velocity and angular velocity, acceleration, and

angular acceleration [31]. All these aspects are simulated and then analyzed in the MSC.Adams/Postprocessor module.

3.4.1 Wind speed

Wind speed, or wind flow speed, is a fundamental atmospheric quantity caused by air moving from high to low pressure, usually due to temperature change. Wind direction is usually almost parallel to isobars (and not perpendicular, as one might expect), due to Earth's rotation. Wind speed affects weather forecasting, aviation, and maritime operations, construction projects, growth, and metabolism rate of many plant species, and has countless other implications.

The variation of wind speed influences the power production of the farm since the rotational speed of the rotor will also vary as the speed changes from time to time. For instance, in the SE7715 wind turbine, the wind speeds below the cut-in speed, 3 m/s, the rotor will stop rotation. This shows the power output is zero. But, when the wind speed is above 3 m/s the power output increases until the speed rate is 11.5 m/s, that is the rated wind speed. Due to the limitation on the capacity of the wind turbine components, the power ceases to increase in the range between 11.5 m/s and 25 m/s. Finally, the turbine shuts off itself, for a speed above 25 m/s for safety reasons.

3.4.2. Angular acceleration

Angular acceleration refers to the time rate of change of angular velocity. As there are two types of angular velocity, namely spin angular velocity and orbital angular velocity, there are naturally also two types of angular acceleration, called spin angular acceleration and orbital angular acceleration respectively. Spin angular acceleration refers to the angular acceleration of a rigid body about its center of rotation, and orbital angular acceleration refers to the angular acceleration of a point particle about a fixed origin, i.e., the time rate of change of its angular velocity relative to the origin. Spin angular acceleration is independent of the choice of origin, in contrast to the orbital angular acceleration.

3.4.3 Torque

Torque is the measure of force that can cause an object to rotate about an axis. Hence, torque can be defined as the rotational equivalent of linear force, the point where the object rotates is called the axis of rotation.

As any rotating mechanical system, a wind turbine torque (τ) is a function of the transmitted power (P) and the rotational speed (ω), expressed as

$$\tau = {}^{P}/_{\omega} \qquad \textit{Eqn. 3.1}$$

where the power produced by the selected wind turbine is: P = 1500 kW, i.e., 1.5 * 10^6 Nm/s.

For the three rated speed cases considered in this study, the angular speeds are calculated as follows:

Case 1: rated speed, n_2 = 15 rpm → $\omega_2 = n_2 * 2\pi/60$ = 1.571 rad/s

Case 2: rated speed, n_3 = 10 rpm → $\omega_3 = n_3 * 2\pi/60$ = 1.047 rad/s

Case 3: rated speed, n_1 = 20 rpm → $\omega_1 = n_1 * 2\pi/60$ = 2.0106 rad/s

Inserting these values for the angular speeds in Eq. 3.1, the following torques are obtained:

τ_1 =9.549 * 10^5 Nm; τ_2 = 1.432 * 10^6 Nm and τ_3 = 7.539 * 10^5 Nm, respectively.

These torque values are used as inputs for the dynamic analysis of the gearbox in MSC. Adams.

3.4.4 Gear force

Gear force between mating gears develops normal to the contacting surfaces. This normal force can be decomposed into axial force, radial force, and tangential force. The normal force is distributed along the contact line, which moves as the gears rotate. Although the force is distributed, the operating pitch circle can be taken as an approximation to the average location for the point of contact. And by considering the projection of the normal force in the transverse plane, the tangential force is one component; the other component is the radial force. Therefore, in this thesis, the selected gear force for analysis is the radial gear force.

3.5 Methods of modeling the wind turbine gearbox vibrations

Modeling and simulation are the activities related to making models of real-world objects and experimenting with these models. Modeling and simulation (M&S) are the use of models (e.g., physical, mathematical, or logical representation of a system, entity, phenomenon, or process) as a basis for simulations to develop data.

MSC. Adams (Automatic Dynamic Analysis of Mechanical System) is a computing software used for modeling, analyzing, and optimizing mechanical systems called MBS (Multi-Body System). It supports static, kinematic, and dynamic analyses of the model. In other words, this software is based on a physical model describing the model specified by relevant ideal objects (mass, rotational inertia, length, kinds of joints, etc.)

MSC Adams consists of several different modules, such as Adams/View, Adams/Car, Adams/Chassis, Adams/Driveline, etc. In this work a universal module MSC. Adams/View is used for modeling the wind turbine gearbox vibrations and analysis of the results.

The basic steps for modeling and simulating in the MSC Adams/View module are as follows:

- Creating models and bodies - geometrical shapes (length, width, depth, dimension, the distance among shafts, etc.),
- Selecting physical characteristics – rotational inertia, mass, dynamic friction coefficient, etc.,
- Creating structures – kinematics definition (translation, rotation, etc.)
- Run a simulation – make motion forces, observe model behavior,
- Record and analyze results in MSC. Adams Postprocessing

3.5.1 Model of the wind turbine gearbox

Parts of the gearbox define the objects in the model that have mass and inertia properties and can move. All forces and constraints that are defined in the model act on these parts during a simulation. This section explains the creation of parts in the gearbox.

The model of the gearbox describes the three stages of the gearbox and, the first stage is the planetary gear stage that includes three rotating components: planet carrier arm, planet gears, and sun pinion. In this dynamic model, the gearbox housing, planet carrier arm, and bedplate are assumed to be rigid, and it is assumed that there are no relative movements or transmission of forces between gearbox shafts. The planet carrier arm with shafts and bearing supports (revolute joint) the planets, thus the planets can rotate freely with respect to the planet carrier arm, and to reduce the load transmitted at each gear mesh the planets split the input load. A parallel gear stages; in the first and second gear stages, the gears and pinions are also mounted between bearings

(revolute joint). MSC Adams/View was used to model the gears tooth wheels and bearing structures.

This wind turbine gearbox is used to increase rotational speed from a low-speed rotor to a higher-speed electrical generator. The ratio is 90:1, with a rate of 19 rpm input from the rotor to 1,500 rpm output for the generator.

ADAMS provides machinery components that are used to model different types of gears by specifying the common parameters such as module, number of teeth for all gear pairs, face width, and gear tooth thickness. The design parameters of the gearbox considered in this study are given in Table 3-2, while the bearing specifications are given in Table 3-3.

Table 3-2 Basic geometrical data of tooth wheels of the mechanical gearbox of the wind turbine

Name of parts	Number of teeth	Module	Types of gear
Sun gear	21	10	Helical
Planet gear	39	10	Helical
Ring gear	99	10	Helical
Drive gear of 1st stage	82	8	Helical
Driven gear of 1st stage	23	8	Helical
Drive gear of 2nd stage	76	5.5	Helical
Driven gear of 2nd stage	23	5.5	Helical

Table 3-3 Bearing's specifications

Name of bearings	Number
1st stage bearings	SKF NU 1014
2nd stage bearings	SKF NU 208

3.5.2 Selection of physical characteristics

The gears in the gearbox are made from steel SAE-AISI 1045, whose physical properties are: density, $\rho = 786\ \mathrm{Kg}/m^3$, modulus of elasticity, E = 210 GPa, and poison's ratio, v = 0.3. The necessary variables for defining the contact of the gears include static friction coefficient (μ_s), Static transonic speed (V_s), Dynamic friction coefficient (μ_d), and Dynamic transonic speed (V_d). And their values are 0.1, 1 mm/s, 0.08, and 10 mm/s respectively.

3.5.3 Description of the gearbox joints

ADAMS/View provides a variety of idealized joints from which you can choose. Idealized joints are mathematical representations of joints that have physical counterparts, such as a revolute (hinge) or translational joint (sliding dovetail). Idealized joints connect two parts. The parts can be rigid bodies, flexible bodies, or point masses. Idealized joints can be placed anywhere in the model (A). ADAMS/View supports two types of idealized joints: simple and complex. Simple joints directly connect bodies and including translational joints, cylindrical joints, spherical joints, planar joints, etc.

In the working condition of the virtual wind turbine gearbox model simulation, the first assumption is that the tooth wheels are attached to the countershaft with the shaft designated as a "fixed joint". Three shafts in relation to each other are placed by rotation joints designated as "Revolute joint". Single shafts are positioned in ball bearings that are connected with the base of the transmission system. It enables the vibration signal to be transmitted through these bearings to the gearbox.

3.5.4 Simulation conditions

Simulation condition is a process of performing MSC ADAMS/View module during which the wind turbine is replaced by its model. This process aims to obtain information about the examined dynamic system and find whether its behavior corresponds to reality. Simulation is a process during which a virtual gearbox model is created. The model becomes similar to a real gearbox with the properties observed during the operation. In the case of simulation of vibrations, it consists of vibration signals in three axes – x, y, and z. The basic parameters which are calculated for vibrations are trajectory, velocity and angular velocity, acceleration, and angular acceleration [31].

All these aspects are simulated and then analyzed in the MSC Adams/Postprocessor module. The gearbox is used to increase the wind speed from the rotor. In the process of operation, it could suffer from heavy stimulation of the wind turbine rotor, the axles, and other sources such as oil, backlash, and clearance. These stimulations cause complex dynamic load which is the main reason for vibrations, impact, noise, and other signs. The designated operating conditions are based on the working characteristics of the wind turbine gearbox:

i. Three different rotation speeds n = 10 rpm, 15 rpm, and 20 rpm are applied on the carrier of the planetary gear stage for three simulations;

ii. The load torque calculated from the maximum power of the generator used on the wind turbine ($7.54 * 10^5\ Nm$, $9.88 * 10^5\ Nm$, and $1.432 * 10^6\ Nm$)

iii. Other parameters are applied as follows:

- Simulation time (end time) = 1 s,
- Simulation step (step size) = 0,001.

3.6 Analysis of the simulation results

3.6.1 Algorithms for the dynamic simulation

MSC Adams has four types of solvers (the *Gstiff, Wstiff, Dstiff,* and *Constant-BDF*) to solve the Differential-Algebra Equation (DAE) for the multi-body dynamic simulation. All solvers custom multi-step, variable order algorithms and apply one of these three integration formats counting the *Index3 (I3), Stabilized Index 1 (SI1),* and *Stabilized Index 2 (SI2)* [32].

The *Gstiff* and *Wstiff* use a variable step and fixed coefficients. Both solvers calculate faster and with higher accuracy than *Dstiff* and *Constant-BDF*, but when calculating velocity, an error will occur that might stimulate discontinuities in acceleration. For this reason, the error has to be controlled by limiting the maximum step during the simulation.

The *Dstiff* is stable and can be modified according to variable steps without any accuracy loss. But it involves more calculation time than *Gstiff*. Its algorithm is the same as *Wstiff*, but only allows the integration format Index3. The *Constant-BDF* algorithm customs fixed steps, which makes it necessary when *SI2* format is selected with a short step. But the calculation time is slower than *Gstiff* and *Wstiff*. It has also high accuracy with less sensitivity to the discontinuity of the acceleration and force as the *Gstiff* [32].

There are different types of Integration formats, such as *SI1*, *SI2*, and *SI3*. The *SI1* displays all state variables such as displacement, velocity, and Lagrange multiplier by presenting the velocity constrained equations instead of acceleration constrained equations. Therefore, it's accurate but it's sensitive to the models with friction and contact problems. The *SI3* displays displacement errors and other state variables of the differential equations, but not the velocities and constrained reaction forces. Therefore, its accuracy when calculating velocities, acceleration, and constrained reaction forces is less than others. Unlike the *SI1*, the *SI2* can control the errors of Lagrange

multiplier and velocity constrained equations, so accurate results could be obtained for the velocity and acceleration computation.

Therefore, depending on the above discussion about the solvers and integration formats, the *Wstiff* solver with *SI2* integration is adopted for the dynamic simulation of the wind turbine gearbox simulation.

3.6.2 Algorithm analysis of the contact force

Because the function of contact force is periodic, a FFT will be used to decompose it into a sum of simple harmonic functions, namely sines and cosines. Theoretically, the FFT can be defined as follows [11]:

$$x(t) = a_0 + \sum_{n=1}^{\infty}(a_n \cos\frac{2\pi nt}{T} + b_n \sin\frac{2\pi nt}{T}) \quad \textit{Eqn. 3.2}$$

Where x(t) is the function of contact force with period T, a_n and b_n are constants called the coefficients of the transform and given by the Euler formulas.

$$a_0 = \frac{1}{T}\int_{-T/2}^{T/2} x(t)\ dt \quad \textit{Eqn. 3.3}$$

$$a_n = \frac{2}{T}\int_{-T/2}^{T/2} x(t)\ \cos\frac{2\pi nt}{T}dt,\ \ n = 1,2,3,\ldots \quad \textit{Eqn. 3.4}$$

$$b_n = \frac{2}{T}\int_{-T/2}^{T/2} x(t)\ \sin\frac{2\pi nt}{T}dt,\ \ n = 1,2,3,\ldots \quad \textit{Eqn. 3.5}$$

However, in practice, the function of contact force is a set of data with discrete and finite values x_n (n = 1, 2, ...). To perform the analysis using these finite values of discrete data, the discrete Fourier transform (DFT) should be applied:

$$x_n = \frac{1}{N}\sum_{k=0}^{N-1} x_k e^{-j2\pi nk/N}\ , nm = 0,2,2,\ldots N-1 \quad \textit{Eqn. 3.6}$$

Where N is the number, x_n in a constant interval Δt & x_n , is called DFT of the discrete values $x_0, x_1, \ldots x_{N-1}$.

The next equation will transfer correspondingly finite values on the time axis to the discrete spectra on the frequency axis. DFT can also use real numbers instead of complex ones,

$$\begin{cases} A_n = \frac{1}{N}\sum_{k=0}^{N-1} x_k \cos\frac{2\pi nk}{N} \\ B_n = \frac{1}{N}\sum_{k=0}^{N-1} x_k \sin\frac{2\pi nk}{N} \end{cases} \qquad n = 0, 1, 2, \ldots, N-1, \quad \textit{Eqn. 3.8}$$

Where $x_n = A_n + jB_n$.

In this work, a window function is used to change the discrete values to continuous and periodic. Discontinuities are "filled in" by forcing the function of contact force to be equal to zero at the beginning and the end of the calculated period.

MSC Adams/post-processor provides some windowing functions such as *Rectangular* (no window was used), *Gaussian*, *Hamming*, *Blackman*, and *Hanning*.

$$w[n] = 0.723 - 0.498\,cos\frac{2\pi n}{N} + 0.0792\,cos\frac{4\pi n}{N} \qquad \textit{Eqn. 3.9}$$

After many trials, the *Blackman* windowing function was chosen to analyze the results that are found after the simulation.

CHAPTER FOUR

4. Modeling of the Gearbox

4.1 Structure and components of Adama wind farm wind turbine gearbox

At the Adama wind farm-2, there are 102 wind turbines. The selected wind turbine is SE7715. Its gearbox consists of three stages high-speed gear stage which is connected with the generator, intermediate parallel gear stage, and low-speed planetary gear stage that absorbs the aerodynamic loadings from the rotor. So that, by taking the assumption into account the input load for the Adama wind turbine gearbox dynamic model is limited to torsional load only, and this torsional load is going to be applied directly to the planet carrier arm and it transmits the load to the planet gears and the sun pinion.

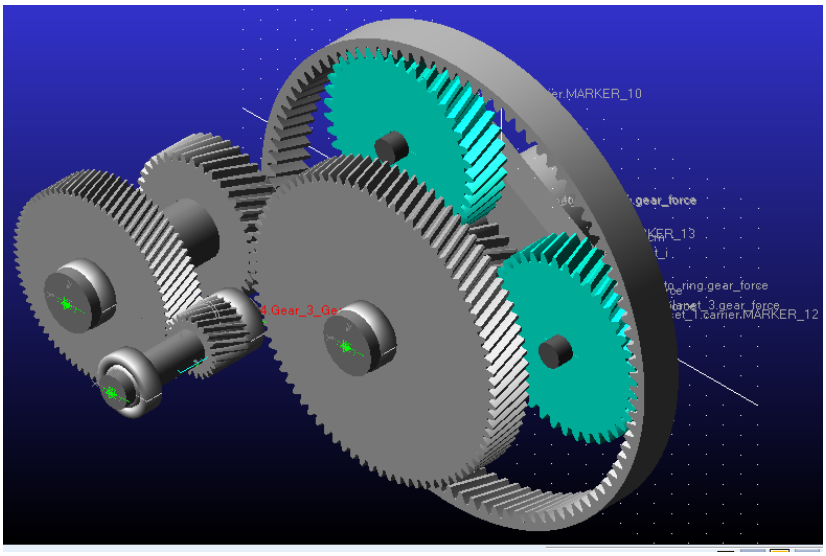

Figure 4.1 ADAMS model of the gearbox

Figure 4.1 is a model of the gearbox that describes the three stages of the gearbox and the first stage is the planetary gear stage that includes three rotating components: planet carrier arm, planet gears, and sun pinion. In this dynamic model, the gearbox housing, planet carrier arm, and bedplate are assumed to be rigid, and it is assumed that there are no relative movements or transmission of forces between gearbox shafts. The planet carrier arm with shafts and bearing supports (revolute joint) the planets, thus the planets can rotate freely with respect to the planet carrier arm, and to reduce the load transmitted at each gear mesh the planets split the input load. A parallel gear stages;

in the first and second gear stages, the gears and pinions are also mounted between bearings (revolute joint).

4.2 Mathematical equation of the gearbox

Wind turbine gearbox components are modeled to predict the dynamic responses.

Assumptions

- The non-torsional loads that are applied to the gearbox are assumed to be uncoupled.
- The gearbox housing, planet carrier arm, and bedplate are assumed to be rigid.
- There are no relative movements or transmission of forces between gearbox shafts.
- There is equal load sharing between planets that rotate freely with respect to the planet carrier arm.
- The low-frequency excitation is considered (wind speed causes the external excitation fluctuation).
- The planet carrier arms are connected with planets by a revolute joint.
- All parallel gears and pinions are also mounted between bearings.

The time-varying gear mesh stiffness, damping, and the static transmission error represent a lumped-parameter model of a ring-planet-sun gear-pair, the gear deformation during tooth meshes. The ring gear, sun gear, planet gear, and parallel gears are all helical gears. Therefore, the helical angle and pressure angle of each gear tooth remaining constant, and are allowed to rotate freely during turbine operation. The geometry of gears is determined by Eqn. 4.1.

$$r_{bu} = r_u \cos \alpha \qquad \textit{Eqn. 4.1}$$

Where r_{bu}-base radius of gears, r_u- pitch radius of gears, and α- pressure angles.

Base radius of the sun gear

$$r_{bs} = r_{us} \cos \alpha \ , \quad r_{us} = N_s * M$$

Where N_s = number of teeth of the sun gear, M = module

$$r_{us} = 21 * 10 = 210\text{mm}$$

$$r_{bs} = 210mm * cos\, 20 = 197.3\ mm$$

Base radius of planet gears

$$r_{bp} = r_{up}\, cos\, \alpha\ ,\ \ r_{up} = N_p * M$$

Where N_p = number of teeth of planet gear, M = module

The pitch radius of planets, $r_{up} = 39 * 10 = 390\, mm$

Then the base radius of the planets, $r_{bp} = 390 * cos\, 20 = 366.48\, mm$

Base radius of gear-1

$$r_{bg1} = r_{ug1}\, cos\, \alpha\ ,\ \ r_{ug1} = N_{g1} * M$$

The pitch radius of gear-1, $r_{ug1} = 82 * 8 = 656\, mm$

Then the base radius of the gear-1, $r_{bg1} = 656 * cos\, 20 = 616.4\, mm$

Base radius of gear-2

$$r_{bg2} = r_{ug2}\, cos\, \alpha\ ,\ \ r_{ug2} = N_{g2} * M$$

The pitch radius of gear-2, $r_{ug2} = 23 * 8 = 184\, mm$

Then the base radius of the gear-2, $r_{bg2} = 184 * cos\, 20 = 172.8\, mm$

Base radius of gear-3

$$r_{bg3} = r_{ug3}\, cos\, \alpha\ ,\ \ r_{ug3} = N_{g3} * M$$

The pitch radius of gear-3, $r_{ug3} = 76 * 5.5 = 418\, mm$

Then the base radius of the gear-3, $r_{bg3} = 418 * cos\, 20 = 392.8\, mm$

Base radius of gear-4

$$r_{bg4} = r_{ug4}\, cos\, \alpha\ ,\ \ r_{ug4} = N_{g4} * M$$

The pitch radius of gear-4, $r_{ug4} = 23 * 5.5 = 126.5\, mm$

Then the base radius of the gear-4, $r_{bg4} = 126.5 * cos\, 20 = 118.9\, mm$

The equivalent transverse displacement of the gearbox components along the line of action, caused by their rotational displacement is,

$$V_u = r_{bu}\theta_u \qquad \textit{Eqn. 4.2}$$

Then the relative displacement of sun-planet gear mesh on the line of action, caused by rotation is,

$$V_{spn\_\theta} = (V_S - V_{pn} - V_c)cos\,\beta_s \qquad \textit{Eqn. 4.3}$$

The relative displacement of sun-planet gear mesh on the line of action caused by the translational motions can be given by:

$$V_{spn\_r} = \{\ X_s\,sin\,\alpha - Y_s\,cos\,\alpha - X_{pn}\,sin\,\alpha - Y_{pn}\,cos\,\alpha - X_c\,sin\,\alpha - Y_c\,cos\,\alpha\ \}\ cos\,\beta_p + (Z_s - Z_{pn} - Z_c)\,sin\,\beta_s \qquad \textit{Eqn. 4.4}$$

By combining (3) and (4), yields the total relative displacement of sun-planet gear mesh on the line of action:

$$V_{spn} = (V_{spn\_\theta} - V_{spn_r}) \qquad \textit{Eqn. 4.5}$$

The same process can be done for planets 2 and 3 but the number of planet gears is three, planetary gears have equal load sharing among themselves. So relative displacement of sun-planet gear 1 mesh is the same as planet gear 2 and 3.

The relative displacement of ring-planet gear mesh on the line of action, caused by rotation, can be written as

$$V_{rpn\_\theta} = (V_{pn} - V_c)cos\,\beta_s \qquad \textit{Eqn. 4.6}$$

The relative displacement of ring-planet gear mesh on the line of action, caused by the translational motions, can be expressed as,

$$V_{rpn\_r} = (X_{pn}\,sin\,\alpha - Y_{pn}\,cos\,\alpha - X_c\,sin\,\alpha - Y_c\,cos\,\alpha)\,cos\,\beta_p + (Z_{pn} - Z_c)\,sin\,\beta_s \qquad \textit{Eqn. 4.7}$$

By taking into account the static transmission error of the ring-planet gear mesh, the total relative displacement is

$$V_{rpn} = V_{rpn\_\theta} - V_{rpn_r} - e_{rp} \qquad \textit{Eqn. 4.8}$$

The relative displacement of the gear pair at the intermediate parallel gear stage, caused by rotation, can be calculated as:

$$V_{s1} = V_1 - V_s \quad \text{Eqn. 4.9}$$

The relative displacement of the gear pair at the intermediate parallel gear stage, caused by rotation, can be expressed by:

$$V_{1,2\_\theta} = (V_2 - V_1)cos\,\beta_g \quad \text{Eqn. 4.10}$$

The relative displacement of gear-pair, caused by the translational motions, is given by:

$$V_{1,2\_r} = (X_2\,sin\,\alpha - Y_2\,cos\,\alpha - X_1\,sin\,\alpha - Y_1\,cos\,\alpha)\,cos\,\beta_p + (Z_2 - Z_1)\,sin\,\beta_s \quad \text{Eqn. 4.11}$$

By considering the static transmission error between the gear and pinion, the total relative displacement is:

$$V_{1,2} = V_{1,2\_\theta} - V_{1,2\_r} - e_{1,2} \quad \text{Eqn. 4.12}$$

The relative displacement between the gears g2 and g3 can be obtained by:

$$V_{2,3} = V_3 - V_2 \quad \text{Eqn. 4.13}$$

For the high-speed parallel gear stage, the relative displacement of the gear mesh on the line of action, caused by rotation, can be written as:

$$V_{3,4\_\theta} = (V_4 - V_3)cos\,\beta_g \quad \text{Eqn. 4.14}$$

The relative displacement of gear pairs on the line of action, caused by the translational motions, can be expressed by:

$$V_{3,4\_r} = (X_4\,sin\,\alpha - Y_4\,cos\,\alpha - X_3\,sin\,\alpha - Y_3\,cos\,\alpha)\,cos\,\beta_p + (Z_4 - Z_3)\,sin\,\beta_s \quad \text{Eqn. 4.15}$$

By including the static transmission error between the gear and pinion, the total relative displacement is:

$$V_{3,4} = V_{3,4\_\theta} - V_{3,4\_r} - e_{3,4} \quad \text{Eqn. 4.16}$$

The gear pairs meshing forces of the wind turbine gearbox can be obtained from the relative displacements of gear meshes V_j (V_j represents V_{rpn}, V_{spn}, $V_{1,2}$ and $V_{3,4}$, $(n = 1,2,3)$. By considering the gear backlash, the meshing forces of gear pairs (e.g., F_{rpn} between the ring-planet gear mesh) can be recalculated by next Equation 4.17, where k_{rp} represent the gear meshing stiffness of the ring-planet gear pairs, and f_{V_j} given and it is the vector form of the nonlinear gear

mesh displacement function (no gear backlash exists on shafts). Damping forces can be calculated similarly;

$$F_{rp_n} = k_{rp} f_{V_j}; n = 1,2,3 \quad \text{Eqn. 4.17}$$

$$f(V_j) = \begin{cases} V_j - b, V_j > b \\ 0, -b \le V_j \le b \\ V_j + b, V_j < -b \end{cases} \quad \text{Eqn. 4.18}$$

The equations of motion of the gearbox components can be obtained by applying Newton's laws. For the planet carrier, the equations of motion are given by:

$$(I_c + 3m_p^2)\ddot{\theta}_c + \sum_{n=1}^{3}(k_{sp} f(V_{spn}) + C_{sp}\dot{V}_{spn}) \cos\beta_s \, r_{bc} + \sum_{n=1}^{3}(k_{rp} f(V_{spn}) + C_{rp}\dot{V}_{spn}) \cos\beta_s \, r_{bc} = T_{in} \quad \text{Eqn. 4.19}$$

$$m_c\ddot{x}_c + \left[\sum_{n=1}^{3}(k_{sp} f(V_{spn}) + C_{sp}\dot{V}_{spn}) + \sum_{n=1}^{3}(k_{rp} f(V_{rpn}) + C_{rp}\dot{V}_{rpn})\right] \cos\beta_s \sin\alpha - k_{cx}x_c - C_{cx}\dot{x}_c = 0$$

$$m_c\ddot{y}_c + \left[\sum_{n=1}^{3}(k_{sp} f(V_{spn}) + C_{sp}\dot{V}_{spn}) + \sum_{n=1}^{3}(k_{rp} f(V_{rpn}) + C_{rp}\dot{V}_{rpn})\right] \cos\beta_s \cos\alpha - k_{cy}y_c - C_{cy}\dot{y}_c = 0$$

$$m_c\ddot{z}_c + \left[\sum_{n=1}^{3}(k_{sp} f(V_{spn}) + C_{sp}\dot{V}_{spn}) + \sum_{n=1}^{3}(k_{rp} f(V_{rpn}) + C_{rp}\dot{V}_{rpn})\right] \sin\beta_s - k_{cz}x_c - C_{cz}\dot{z}_c = 0$$

For the sun pinion, the equations of motion are:

$$I_s\ddot{\theta}_s + \sum_{n=1}^{3}(k_{sp} f(V_{spn}) + C_{sp}\dot{V}_{spn}) \cos\beta_s \, r_{bs} + (k_{sg1}V_{sg1} + C_{sg1}\dot{V}_{sg1}) \cos\beta_s \, r_{bs} = T_{in} \quad \text{Eqn. 4.20}$$

$$m_s\ddot{x}_s + \sum_{n=1}^{3}(k_{sp} f(V_{spn}) + C_{sp}\dot{V}_{spn}) \cos\beta_s \sin\alpha + k_{sx}x_s + C_{sx}\dot{x}_s = 0$$

$$m_s\ddot{y}_s + \sum_{n=1}^{3}(k_{sp} f(V_{spn}) + C_{sp}\dot{V}_{spn}) \cos\beta_s \cos\alpha + k_{sy}y_s + C_{sy}\dot{y}_s = 0$$

$$m_s\ddot{z}_s + \sum_{n=1}^{3}(k_{sp} f(V_{spn}) + C_{sp}\dot{V}_{spn}) \sin\beta_s + k_{sz}x_s + C_{sz}\dot{z}_s = 0$$

For the planet gears, the equations of motion are given by:

$$I_p\ddot{\theta}_{pn} + (k_{rp} f(V_{rpn}) + C_{rp}\dot{V}_{rpn}) \cos\beta_s + k_{sp} f(V_{rpn}) + C_{sp}\dot{v}_{spn}) = 0 \quad \text{Eqn. 4.21}$$

$$m_p\ddot{x}_{pn} + \left[\left(k_{rp} f(V_{rpn}) + C_{rp}\dot{V}_{rpn}\right) - \left(k_{sp} f(V_{spn}) + C_{sp}\dot{v}_{spn}\right)\right] \cos\beta_s \sin\alpha + k_{px}x_{pn} + C_{px}\dot{x}_{pn} = 0$$

$$m_p\ddot{y}_{pn} + \left[\left(k_{rp} f(V_{rpn}) + C_{rp}\dot{V}_{rpn}\right) - \left(k_{sp} f(V_{spn}) + C_{sp}\dot{v}_{spn}\right)\right] \cos\beta_s \cos\alpha + k_{py}y_{pn} + C_{py}\dot{y}_{pn} = 0$$

$$m_p\ddot{z}_{pn} + \left[\left(k_{rp}f\left(V_{rpn}\right) + C_{rp}\dot{V}_{rpn}\right) - \left(k_{sp}f\left(V_{spn}\right) + C_{sp}\dot{v}_{spn}\right)\right] \sin\beta_s + k_{pz}x_{pn} + C_{pz}\dot{z}_{pn} = 0$$

For the gear at the intermediate parallel gear stage g_1, the equations of motion are written as:

$$I_1\ddot{\theta}_1 + \left(k_{1,2}f\left(V_{1,2}\right) + C_{1,2}\dot{V}_{1,2}\right)\cos\beta_g\, r_{b1} + (k_{s1}V_{s1} + C_{s1}\dot{v}_{s1})r_{b1} = 0 \qquad \textit{Eqn. 4.22}$$

$$m_1\ddot{x}_1 + \left(k_{1,2}f\left(V_{1,2}\right) + C_{1,2}\dot{V}_{1,2}\right)\cos\beta_g \sin\alpha - k_{x1}x_1 - C_{x1}\dot{x}_1 = 0$$

$$m_1\ddot{y}_1 + \left(k_{1,2}f\left(V_{1,2}\right) + C_{1,2}\dot{V}_{1,2}\right)\cos\beta_g \cos\alpha - k_{y1}y_1 - C_{y1}\dot{y}_1 = 0$$

$$m_1\ddot{z}_1 + \left(k_{1,2}f\left(V_{1,2}\right) + C_{1,2}\dot{V}_{1,2}\right)\sin\beta_g - k_{z1}z_1 - C_{z1}\dot{z}_1 = 0$$

For the pinion at the intermediate parallel gear stage g_2, the equations of motion are expressed as:

$$I_2\ddot{\theta}_2 + \left(k_{1,2}f\left(V_{1,2}\right) + C_{1,2}\dot{V}_{1,2}\right)\cos\beta_g + k_{2,3}r_{b2} + k_{2,3}v_{2,3} + C_{2,3}\dot{v}_{2,3})r_{b2} = 0 \qquad \textit{Eqn. 4.23}$$

$$m_2\ddot{x}_2 + \left(k_{1,2}f\left(V_{1,2}\right) + C_{1,2}\dot{V}_{1,2}\right)\cos\beta_g \sin\alpha - k_{x2}x_2 - C_{x2}\dot{x}_2 = 0$$

$$m_2\ddot{y}_2 + \left(k_{1,2}f\left(V_{1,2}\right) + C_{1,2}\dot{V}_{1,2}\right)\cos\beta_g \cos\alpha - k_{y2}y_2 - C_{y2}\dot{y}_2 = 0$$

$$m_2\ddot{z}_2 + \left(k_{1,2}f\left(V_{1,2}\right) + C_{1,2}\dot{V}_{1,2}\right)\sin\beta_g - k_{z2}z_2 - C_{z2}\dot{z}_2 = 0$$

For the gear at the high-speed parallel gear stage g_3, the equations are obtained as:

$$I_3\ddot{\theta}_3 + \left(k_{3,4}f\left(V_{3,4}\right) + C_{3,4}\dot{V}_{3,4}\right)\cos\beta_g\, r_{b3} - (k_{2,3}v_{2,3} + C_{2,3}\dot{v}_{2,3})r_{b3} = 0 \qquad \textit{Eqn. 4.24}$$

$$m_3\ddot{x}_3 + \left(k_{3,4}f\left(V_{3,4}\right) + C_{3,4}\dot{V}_{3,4}\right)\cos\beta_g \sin\alpha - k_{x3}x_3 - C_{x3}\dot{x}_3 = 0$$

$$m_3\ddot{y}_3 + \left(k_{3,4}f\left(V_{3,4}\right) + C_{3,4}\dot{V}_{3,4}\right)\cos\beta_g \cos\alpha - k_{y3}y_3 - C_{y3}\dot{y}_3 = 0$$

$$m_3\ddot{z}_3 + \left(k_{3,4}f\left(V_{3,4}\right) + C_{3,4}\dot{V}_{3,4}\right)\sin\beta_g - k_{z3}z_3 - C_{z3}\dot{z}_3 = 0$$

For the pinion at the high-speed parallel gear stageg_4, the equations of motion are obtained as:

$$I_4\ddot{\theta}_4 + \left(k_{3,4}f\left(V_{3,4}\right) + C_{3,4}\dot{V}_{3,4}\right)\cos\beta_g\, r_{b4} = T_{out} \qquad \textit{Eqn. 4.25}$$

$$m_4\ddot{x}_4 + \left(k_{3,4}f\left(V_{3,4}\right) + C_{3,4}\dot{V}_{3,4}\right)\cos\beta_g \sin\alpha - k_{x4}x_4 - C_{x4}\dot{x}_4 = 0$$

$$m_4\ddot{y}_4 + \left(k_{3,4}f\left(V_{3,4}\right) + C_{3,4}\dot{V}_{3,4}\right)\cos\beta_g \cos\alpha - k_{y4}y_4 - C_{y4}\dot{y}_4 = 0$$

$$m_4\ddot{z}_4 + \left(k_{3,4}f\left(V_{3,4}\right) + C_{3,4}\dot{V}_{3,4}\right)\sin\beta_g - k_{z4}z_4 - C_{z4}\dot{z}_4 = 0$$

Substituting the relative displacements of the gear meshes given by equations 4.3 to 4.18 into equations 4.19 to 4.25 yields the transverse and translational displacements of gears.

The damping of the teeth mesh c_j is expressed by

$$c_j = 2\xi\sqrt{k_j m_{gear} m_{pinion}/(m_{gear} m_{pinion})} \qquad \textit{Eqn. 4.26}$$

Where k_j is the mesh stiffness of the gear pair, ξ is the damping ratio of the tooth mesh (varies between 0.03 and 0.17), m_{gear} and m_{pinion}.

4.3 Developing the ADAMS model of the gearbox

In order to describe the gearbox, the input carrier, first stage shaft, second stage shaft, gears, and the bearing structures are constructed by using MSC.Adams. In ADAMS units are set appropriately as millimeters, newton, kilograms, and seconds (MMGS). The density/material of each part is defined. The material properties for the components are defined in Table 4-1. AISI 1045 Steel is used for all components in the assembly.

Table 4-1 Material Properties

Material	**SAE-AISI 1045**
Mass density	$7.86 * 10^{-6}\ Kg/mm^3$
Stiffness	$210\ GPa$
Poison's ratio	0.3

Since this study is on rigid multi-body dynamic analysis, the mesh stiffness of the gears doesn't vary with time. Therefore, the AISI 1045 steel stiffness value is used as an input for gearbox components.

4.3.1 Joints and Constraints

Wind turbine gearbox contains housing, shaft splines, shaft keys/keyways, as well as bearings to locating the parts in the proper location. These additional features will add higher-order dynamics to the system. There are a variety of methods to model, analyze or compensate for such system dynamics, pure model is created with simple revolute joints connecting each part relative to each other. The revolute joint for the full system is defined in Table 4-2.

Table 4-2 Joint properties in ADAMS

Stage	**Type**	**Body 1**	**Body 2**	**Location (centered)**
1	Lock	ring	Ground	ring center
	Revolute	Carrier	Ring	carrier Pin axis
		Planet 1	Carrier	carrier Pin axis
		Planet 2	Carrier	carrier Pin axis
		Planet 3	Carrier	carrier Pin axis
2	Lock	Support	Ground	Ground
	Revolute	Gear 1	Support	Ground
		Pinion 1	Support	Ground
3	Lock	Support	Ground	Ground

	Revolute	Gear 2	Support	Ground
		Pinion 2	Support	Ground

In a rigid joint, revolute joint dynamics is simplified to a single rotational degree of freedom, which doesn't allow for any flexibility or compliance between the gears and the shaft in which they are joined to. These joint locations mean the location of the shaft and bearing between the gear body and its central shaft. Without bearing dynamics, the gear spinning only around the central axis of the axis shaft and there is no movement outside the plane. It is determined that under standard operations, a uniform lateral load to the gear teeth over a cycle produces negligible out of the bending moments of the plane.

Table 4-2 also shows, the lock joints created between the ring gear and the first stage support. The lock-joint on the support is used to show gears that would be realistically supported by the housing. The ring gear is designed to be fixed with the chosen gear ratio.

4.3.2 Contact and interactions

The interactions between the gear teeth are modeled in ADAMS as a contact force between each body. The contact force represents the gear teeth mesh and must be created between each meshing or contacting body in the system. The body contact forces are shown in Table 4-3.

Table 4-3 . Solid-body contacts in Adams

Stage	**Body 1**	**Body 2**
Stage 1	Sun gear	Planet gear 1
		Planet gear 2
		Planet gear 3
	Ring gear	Planet gear 1
		Planet gear 2
		Planet gear 3
Stage 2	Intermediate gear (gear 1)	Intermediate pinion (pinion 1)
Stage 3	Output gear (gear 2)	Output pinion (pinion 2)

Table 4-3 shows the contact location between each meshing body in the system. These contact forces are modeled as an Impact type contact. The necessary input variables for defining the contact of the gears include static friction coefficient (μ_s), Static transonic speed (V_s), Dynamic friction coefficient (μ_d), and Dynamic transonic speed (V_d). And their values are 0.1, 1 mm/s, 0.08, and 10 mm/s respectively.

4.3.3 Gear force function in Adams

The gear pairs meshing forces of the wind turbine gearbox can be obtained from the relative displacements of gear meshes V_j (V_j represents V_{rpn}, V_{spn}, $V_{1,2}$, and $V_{3,4}$, $(n = 1,2,3)$.

$$F_{rp_n} = k_{rp} f_{V_j}; n = 1,2,3$$

$$f(V_j) = \begin{cases} V_j - b, V_j > b \\ 0, -b \le V_j \le b \\ V_j + b, V_j < -b \end{cases}$$

In order to model this force in Adams the STEP5 function is used. It is used most often to represent a smooth transition between two functions.

CHAPTER FIVE

5. Result and Discussion

5.1 Introduction

The dynamic model of a wind turbine gearbox was developed by MSC ADAMS to determining the dynamic characteristics of the system for the different types of input rotational speeds. In this chapter, the gearbox components such as the planetary gear train, the first and second speedup gear stages, and the bearings dynamic characteristics are demonstrated under the selected external excitation (wind speeds). To analyze the dependence of a vibration signal on the rotational speed of the planet carrier, the selected three input carrier revolutions are (10, 15, and 20 rpm).

The wind load acting on the rotor blade is nonstationary. Since the type of load in a wind turbine is nonlinear nonstationary, huge fluctuation in angular velocity, angular acceleration, and gear forces of the gearbox components are noticed from the time domain responses.

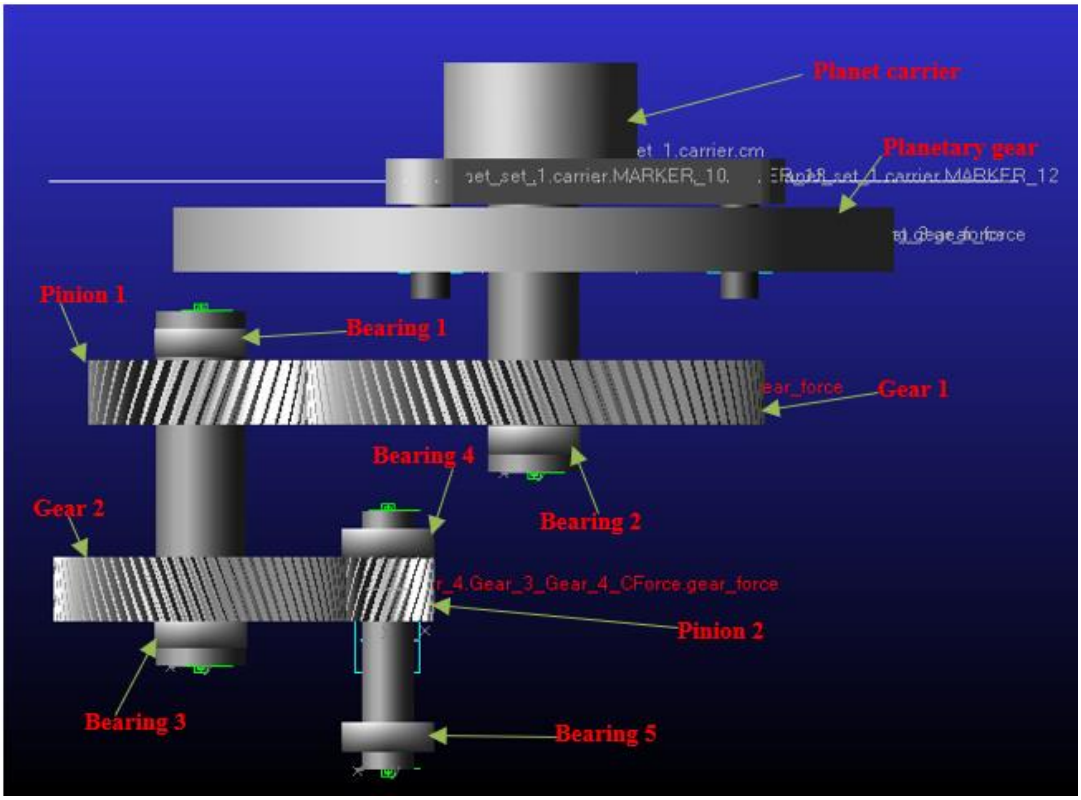

Figure 5.1 Drive train components

5.2 Impact of Input Rotational Speed on the Vibrational Signal of Gears

In order to analyze the dependence of a vibration signal on the number of revolutions, the planet carrier rotational speeds are selected i.e., 10, 15, and 20 rpm. This number of results is adequate for expressing the dependence. to express the simulation results, the selected acceleration values in vertical axis y which is perpendicular to the axis of mechanical gearbox rotation.

Graphical solutions were obtained through dynamic analysis by using ADAMS/view. The gear model in this study calculated all values from the inputted gears geometry. To capture a sufficient number of mesh frequencies. To analyze the dependence of a vibration signal on the number of revolutions, their planet carrier rotational speeds are selected i.e., 10, 15, and 20 rpm. These results are adequate for expressing the dependence. To express the simulation results, the acceleration values in vertical axis y are selected because it is perpendicular to the axis of mechanical gearbox rotation.

5.2.1 Load Case-1 (rotational wind speed 15 rpm and $\tau_1 = 9.549 * 10^5\ Nm$)

The rotational vibration acceleration of all gears at input rotational speed in the time domain is shown in the following sections. The obtained vibration signals of first stage speed-up gears, second stage speed, and planetary gears are all the output of the ADAMS at the rotational speed of 15 rpm and torque 9.549 * 10^5 Nm discussed.

5.2.1.1 First stage speed-up gears

This sub-section shows translation and angular acceleration vibration signals of the first stage of the speed-up gear train at the input rotational wind speed and torque. As shown in Fig. 5.2(a) the translational acceleration of the gear1 increased and decreased periodically with time.

The radial acceleration of the first stage gears is shown in Fig. 5.2(a), the first gear with a rotational speed of 15 rpm has maximum radial acceleration ($4.53 * 10^{-7} mm/s^2$) under load case 1. The pinion 1 also has maximum radial acceleration ($1.479\ mm/s^2$) as depicted in Fig. 5.3(a). As the rotational speed of the pinion increase, the radial acceleration is also higher.

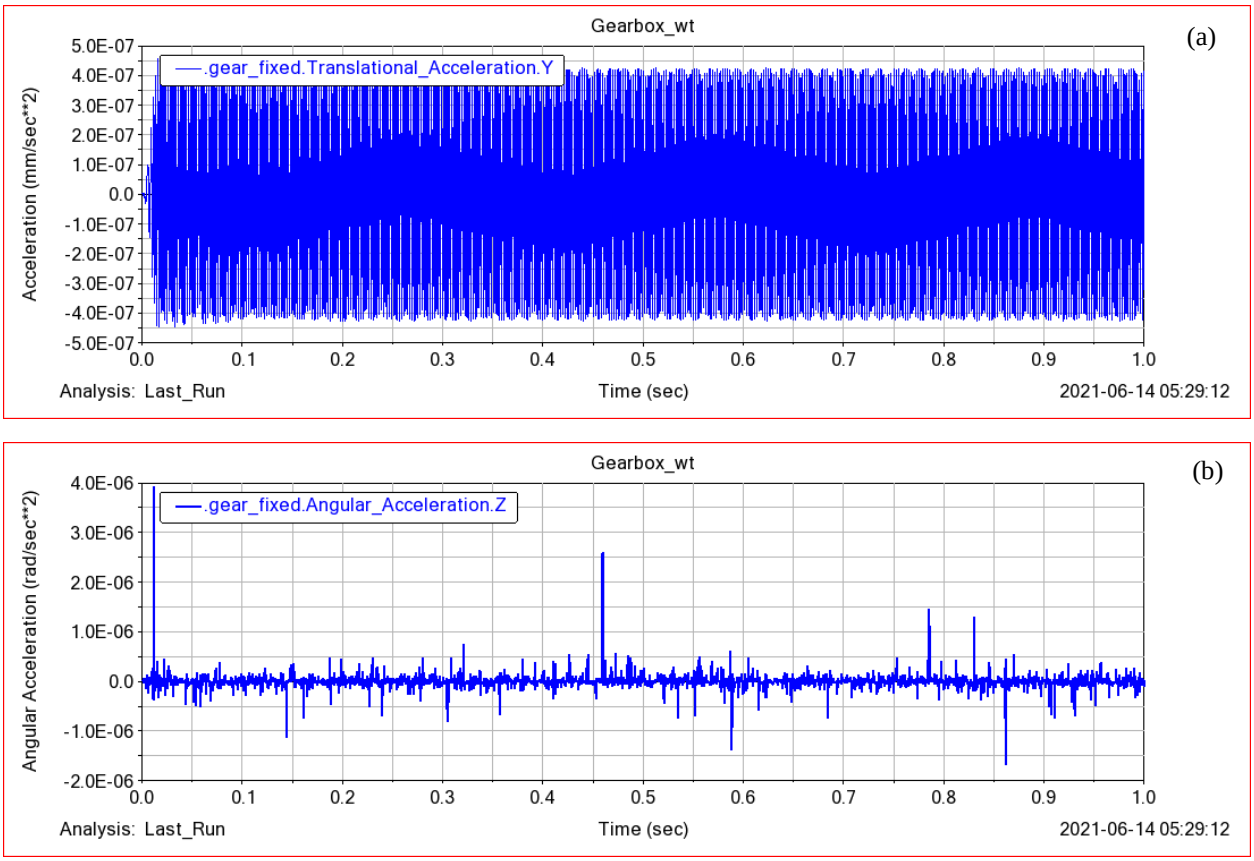

Figure 5.2(a) The translation acceleration of the gear-1 (b) Angular acceleration of the gear-1

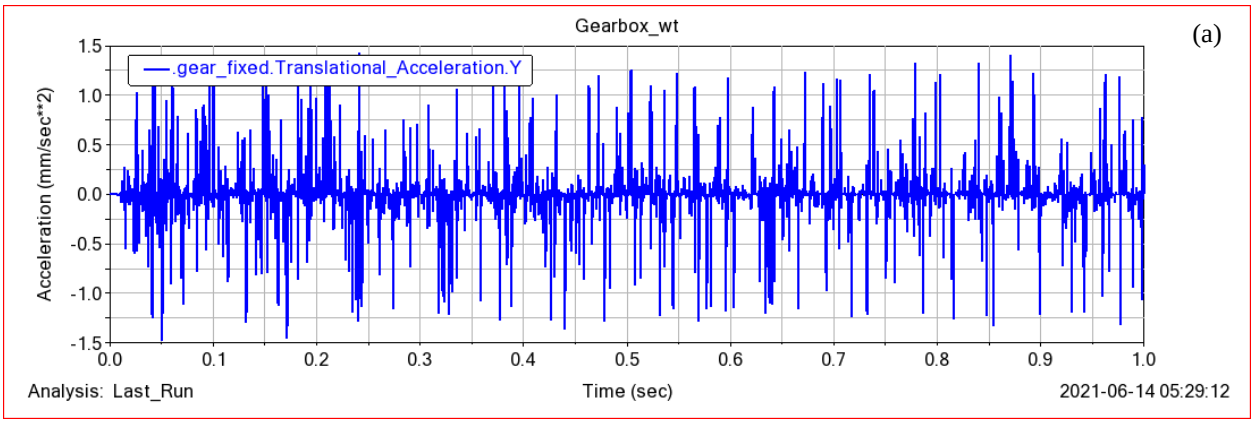

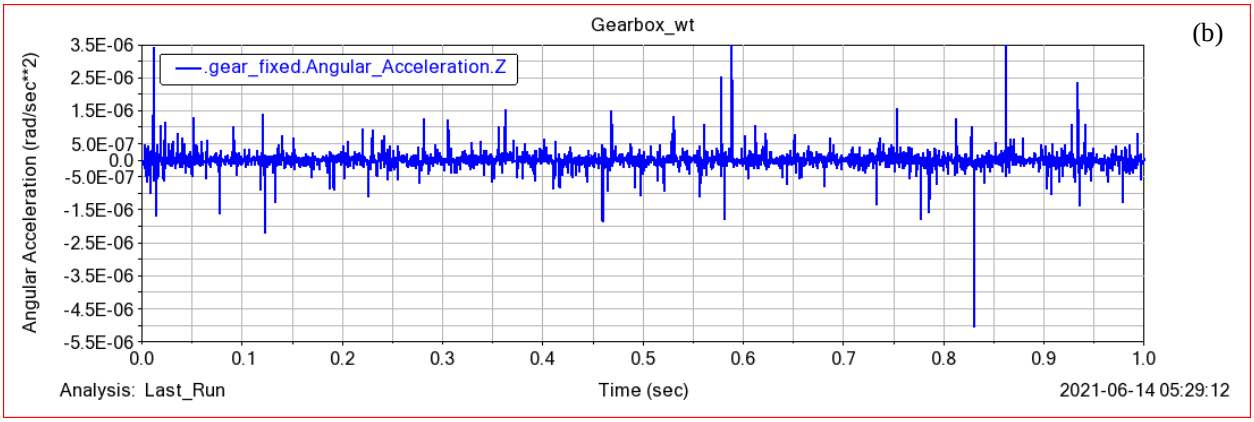

Figure 5.3(a) The translation acceleration of the gear-2 (b) Angular acceleration of the gear-2

The above Figs. 5.2(b) and 5.3(b) also show that the vibration signal of the angular acceleration of gear 1 and gear 2 in the time domain. Angular acceleration along the rotational axis is produced mainly due to the geometrical effect. As shown in Fig. 5.2 (b), the angular acceleration of gear 1 at 15 rpm and load case 1 has a maximum point of $3.97 * 10^{-7}\ rad/s^2$ and in Fig 5.3 (b) the maximum angular acceleration point of the first stage pinion is $3.49 * 10^{-6}\ rad/s^2$. Gear 2 is subjected to the constant angular velocity, but there is an acceleration due to gear 1. The gear-2 will accelerate and decelerate frequently due to the jamming effect, which means there is no free play.

5.2.1.2 Second stage speed-up gears

The radial accelerations of the second stage gears are shown in Figs. 5.4(a) and 5.5(a), respectively while the figures for angular acceleration are depicted in Figs 5.4 (b) and 5.5 (b). As given in Fig. 5.4(a) and (b), the gear-3 with 15 rpm has a maximum radial acceleration of $1.119 * 10^{-5}\ mm/s^2$ under load case 1, and the maximum angular acceleration of gear-3 is $3.486 * 10^{-6}\ rad/s^2$.

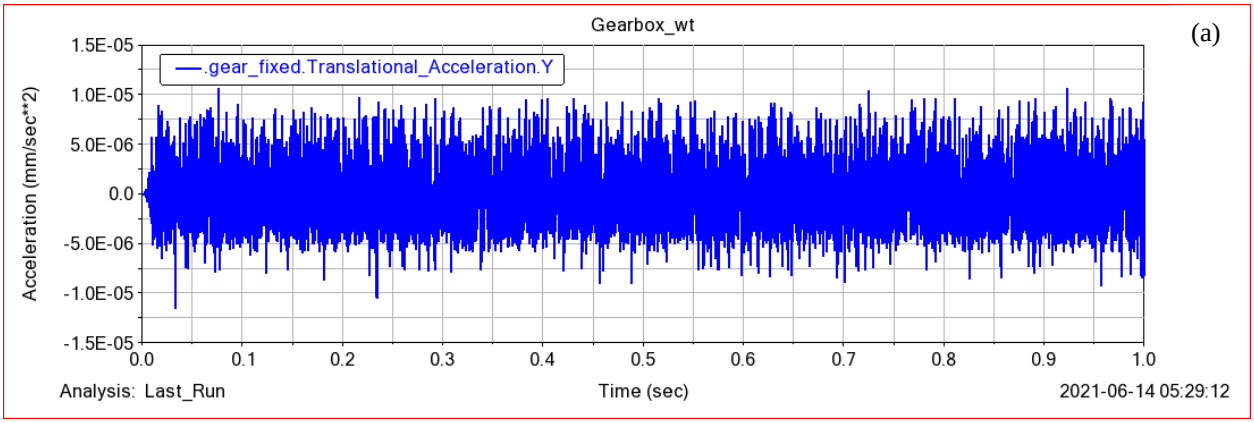

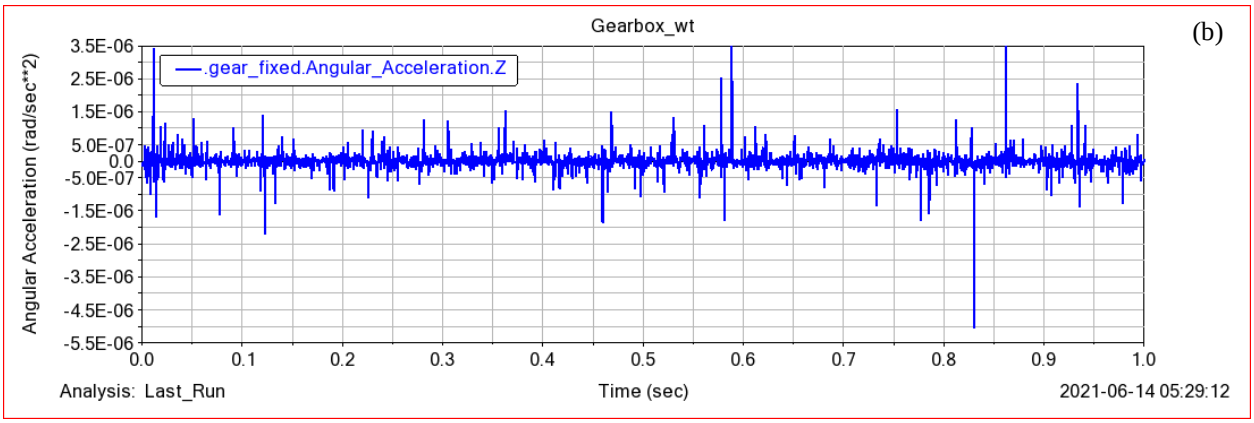

Figure 5.4(a) The translation acceleration of the gear-3 (b) Angular acceleration of the gear-3

As shown in Figs 5.5(a) and 5.5(b), the second stage pinion has a maximum radial acceleration of $25.56\,mm/s^2$ and maximum angular acceleration of $2.67 * 10^{-5}\,rad/s^2$. The angular acceleration of gear-4 along the axis of rotation is higher than gear-3. Since the rotational speed of the pinion is higher. In addition, the angular acceleration is less than the tangential acceleration of the pinion.

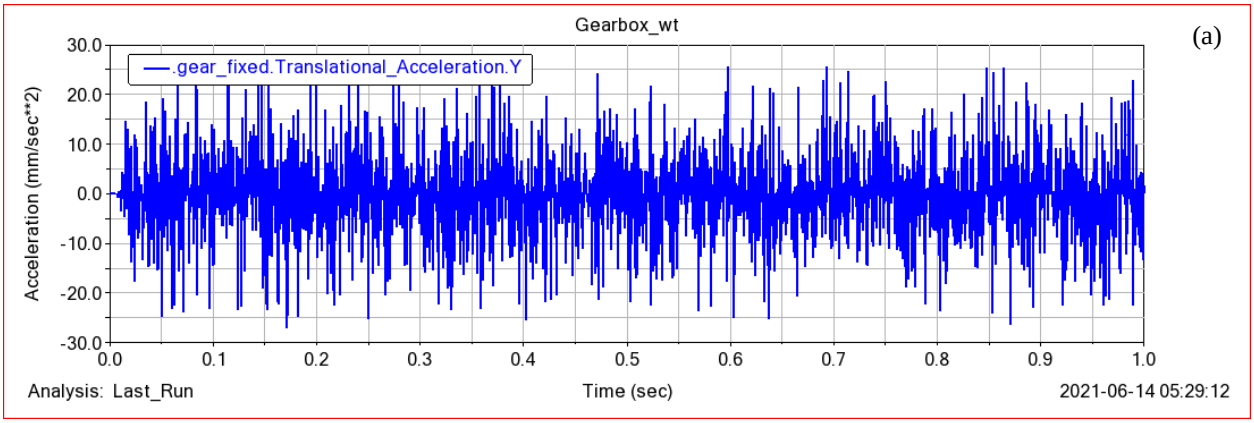

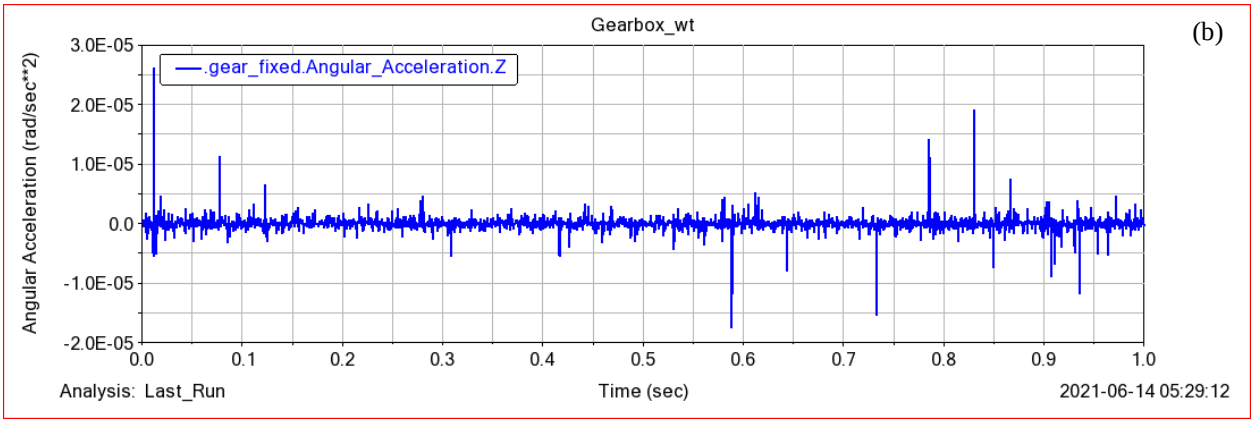

Figure 5.5(a) The translation acceleration of the gear-4 (b) Angular acceleration of the gear-4

5.2.1.3 Planetary gears

In this sub-section, the rotational vibration signals of the planet gears and sun gear are shown graphically. The obtained signals are non-linear. The vibration signal is nonstationary from the fact that at a wind turbine site, the wind load acting on the rotor blade is nonstationary. So, a huge fluctuation in vibration acceleration is noticed from the time domain responses.

Fig 5.6(a) and 5.6(b) show that the vibration signal of radial acceleration and angular acceleration of the planet gear 1 in the time domain. As shown in Fig. 5.6(a), the angular acceleration of the planet gear 1 at 15 rpm and case 1 load has a maximum point of $3.98 * 10^5\ mm/s^2$ and in fig 5.6(b) the maximum angular acceleration point of the planet gear 1 is $4.99 * 10^6\ rad/s^2$.

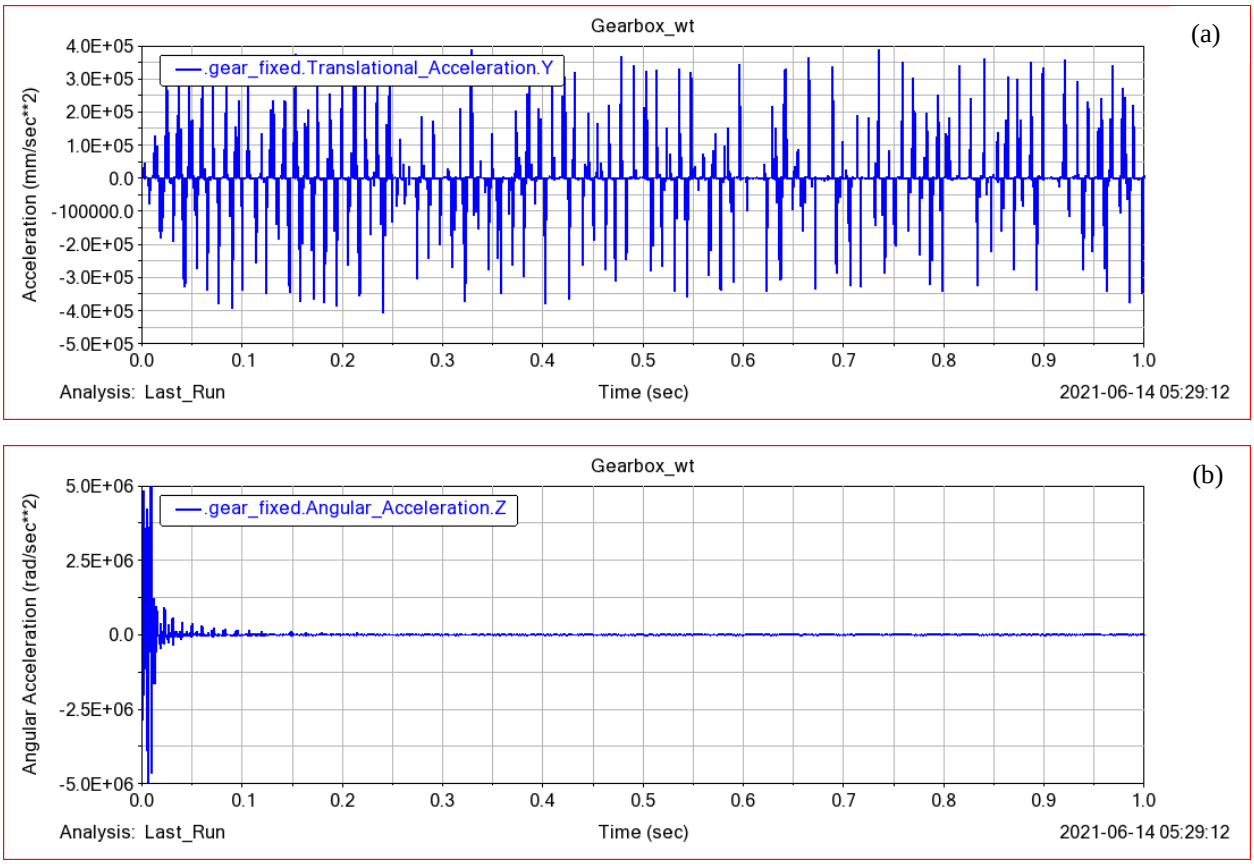

Figure 5.6(a) The translation acceleration of the planet gear-1 (b) Angular acceleration of the planet gear-1

As can be seen in Fig 5.7(a) and (b), the vibration signal of radial acceleration and angular acceleration of the planet gear 2 in the time domain history the angular acceleration of the planet gear 2 has a maximum point of $4.25 * 10^5\ mm/s^2$ and maximum angular acceleration point is

$5.99 * 10^6\ rad/s^2$ respectively. Since, acceleration of the gear is the measure of vibration of the gears, the obtained values from case 1 are optimum when compared with case 2 and case 3.

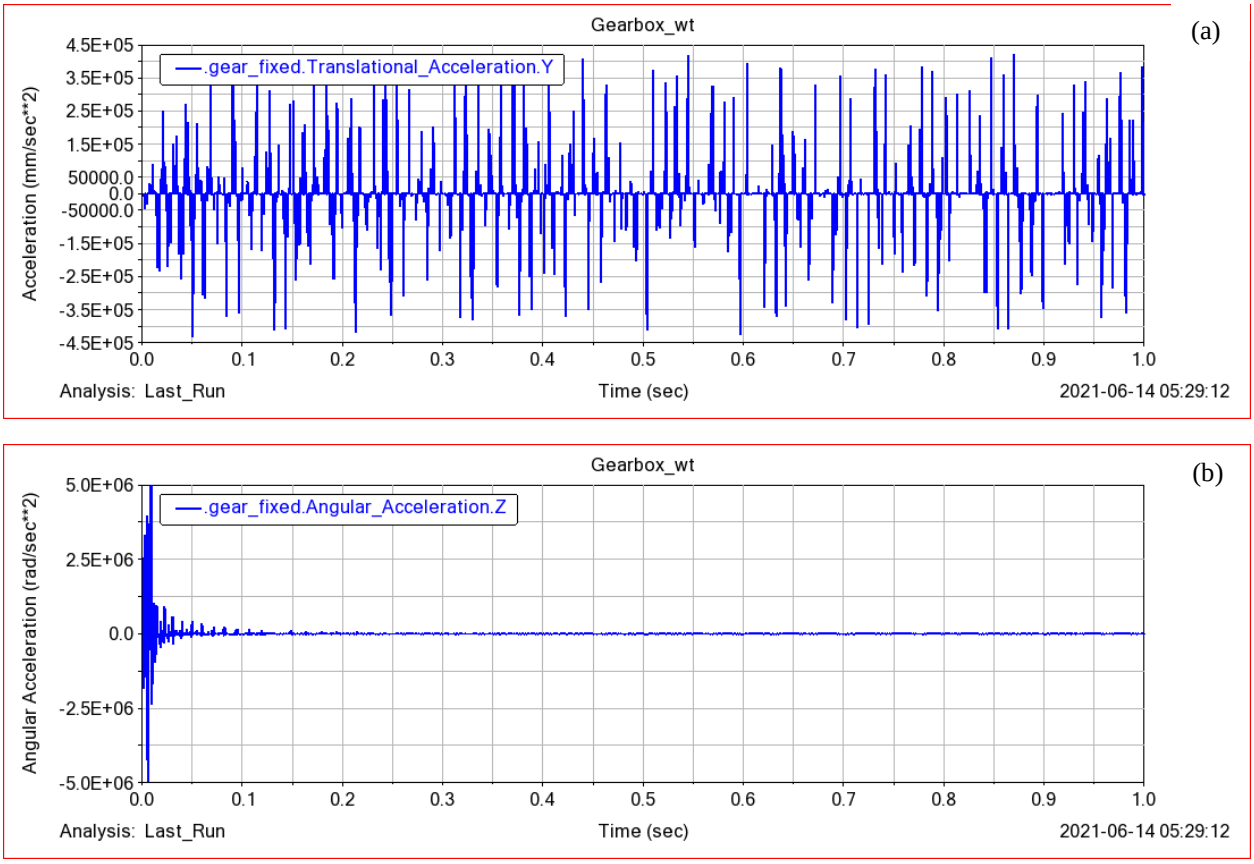

Figure 5.7 The translation acceleration of the planet gear-2 (b) Angular acceleration of the planet gear-2

As shown in figs 5.7(a) the planet gear 2 acceleration is higher because there is high wind speed fluctuation at the input carrier. As depicted in fig 5.7(b), the angular acceleration is also higher at the start and decreases through time.

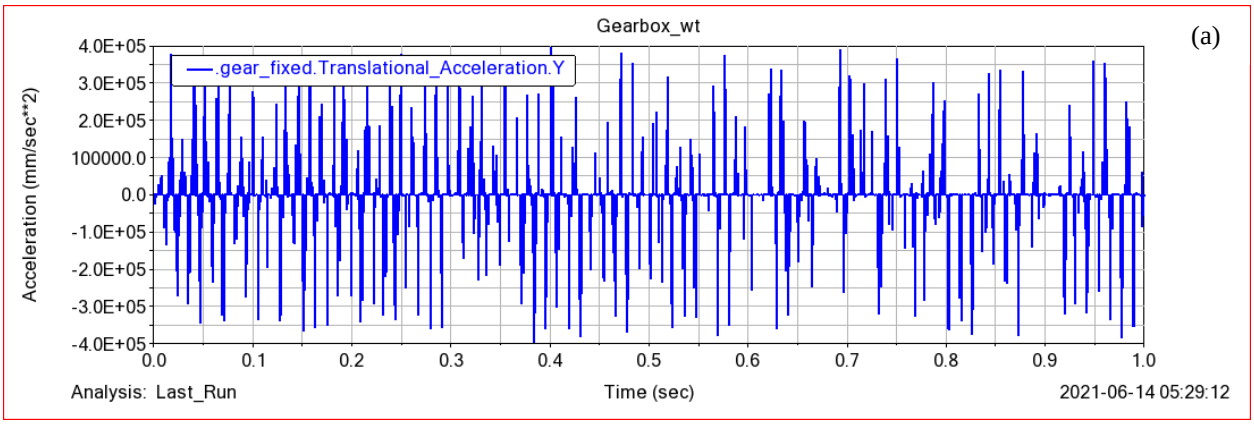

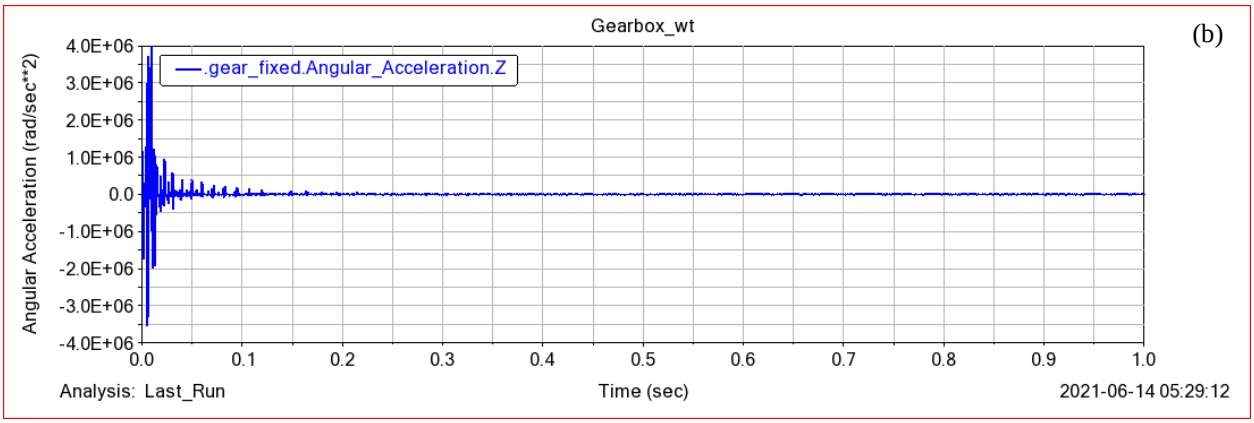

Figure 5.8 The translation acceleration of the planet gear-3 (b) Angular acceleration of the planet gear-3

Fig 5.8(a) and 5.8(b) also show the radial acceleration and angular acceleration vibration signal of the planet gear 3 in the time domain. As shown in Fig. 5.8(a), the angular acceleration of the planet gear 3 at 10 rpm and load case 2 has a maximum point of $3.98 * 10^5\ mm/s^2$ and in fig 5.8(b) the maximum angular acceleration point of the planet gear 3 is $4.0 * 10^6\ rad/s^2$.

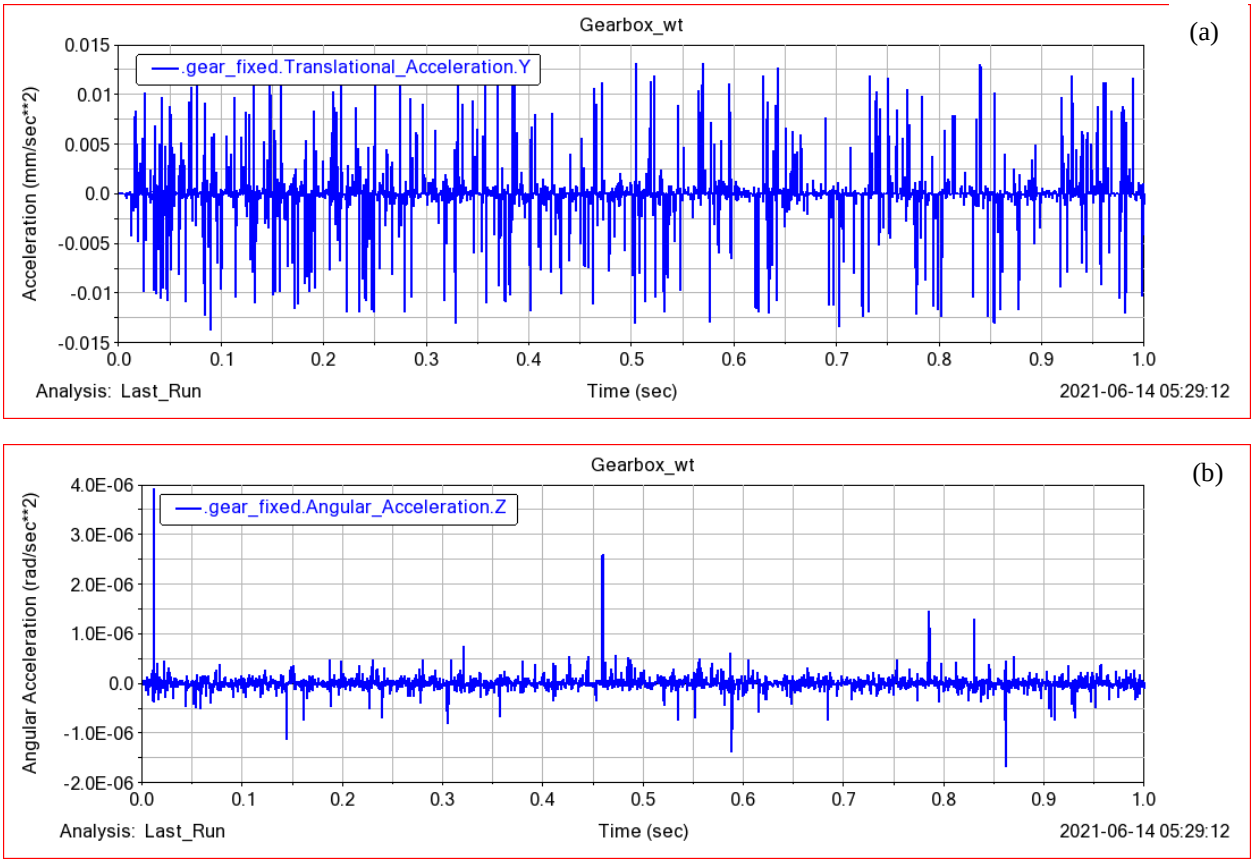

Figure 5.9 (a) The translation acceleration of the sun gear (b) Angular acceleration of the sun gear

As depicted in Fig 5.9(a) and 5.9(b), vibration signal of radial acceleration and angular acceleration of the sun gear in the time domain. As shown in Fig. 5.9(a), the angular acceleration of the sun gear at 15 rpm and case 1 load has a maximum point of $1.31 * 10^{-2}\ mm/s^2$ and in fig 5.9(b) the maximum angular acceleration point of the sun gear is $3.99 * 10^{-6}\ rad/s^2$.

5.2.2 Load Case-2 (rotational wind speed 10 rpm and $\tau_2 = 1.432 * 10^6\ Nm$)

The rotational vibration acceleration of all gears at input rotational speed in the time domain is shown in the following sections. The obtained vibration signals of first stage speed-up gears, second stage speed, and planetary gears are all the output of the ADAMS/ view at the rotational speed of 10 rpm and torque $\tau_2 = 1.432 * 10^6\ Nm$ discussed.

5.2.2.1 First stage speed-up gears

This sub-section shows translation and angular acceleration vibration signals of the first stage of the speed-up gear train at the input rotational wind speed and torque. As shown in Fig. 5.10(a) the translational acceleration of the gear1 increased and decreased periodically with time. The radial acceleration of the first stage gears is shown in Figs. 5.10 (a) and 5.11 (a) respectively while the figures for angular acceleration are also shown in Figs 5.10 (b) and 5.11(b). As given in Fig. 5.10 (a), the first gear with a rotational speed of 10 rpm has maximum translational acceleration ($4.9 * 10^{-8} mm/s^2$) under load case 2 and angular acceleration ($5.9 * 10^{-7} rad/s^2$).

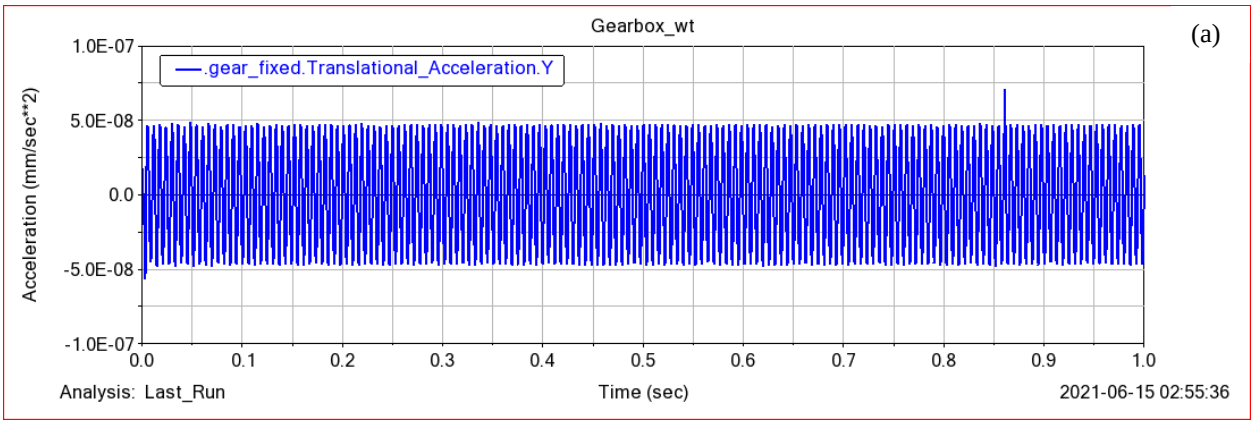

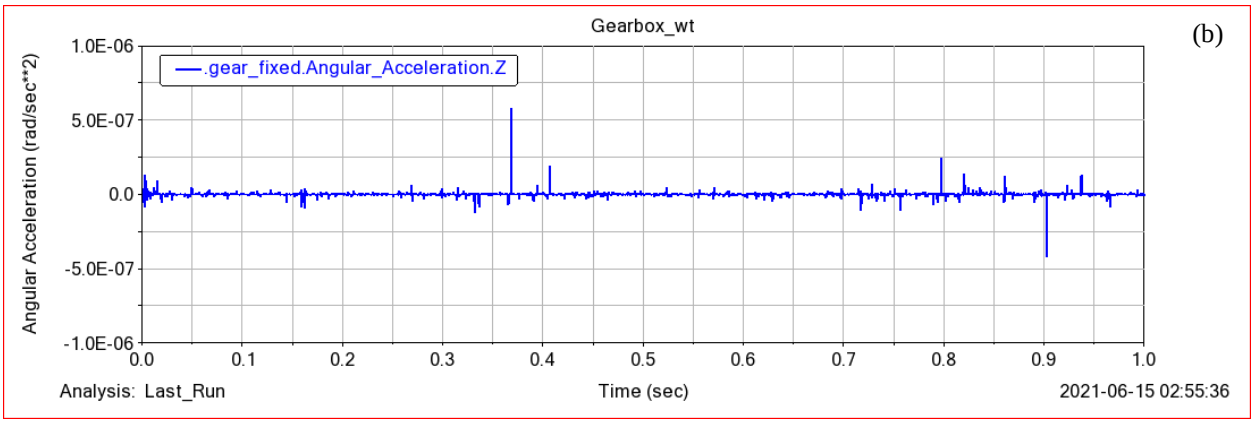

Figure 5.10 (a) The translation acceleration of the gear 1 (b) Angular acceleration of the gear 1

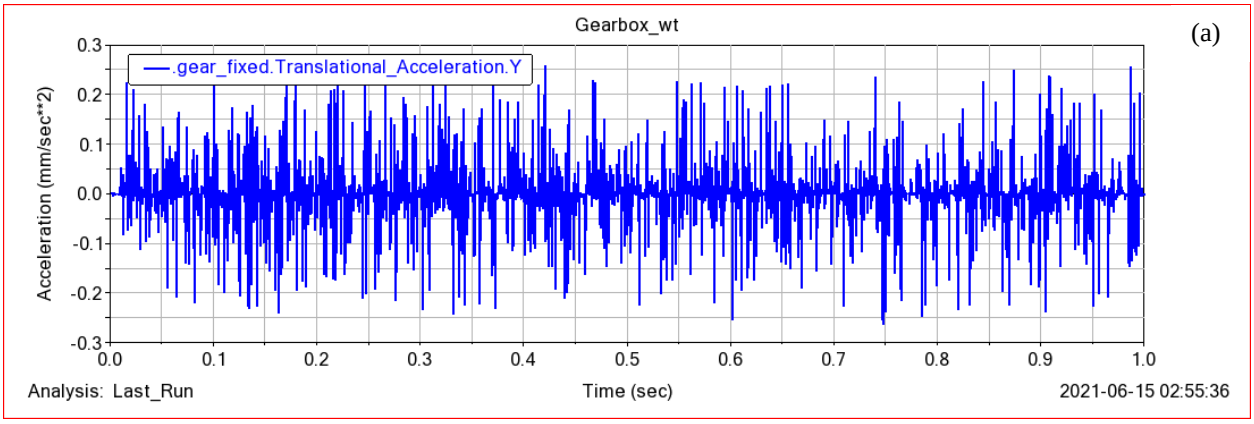

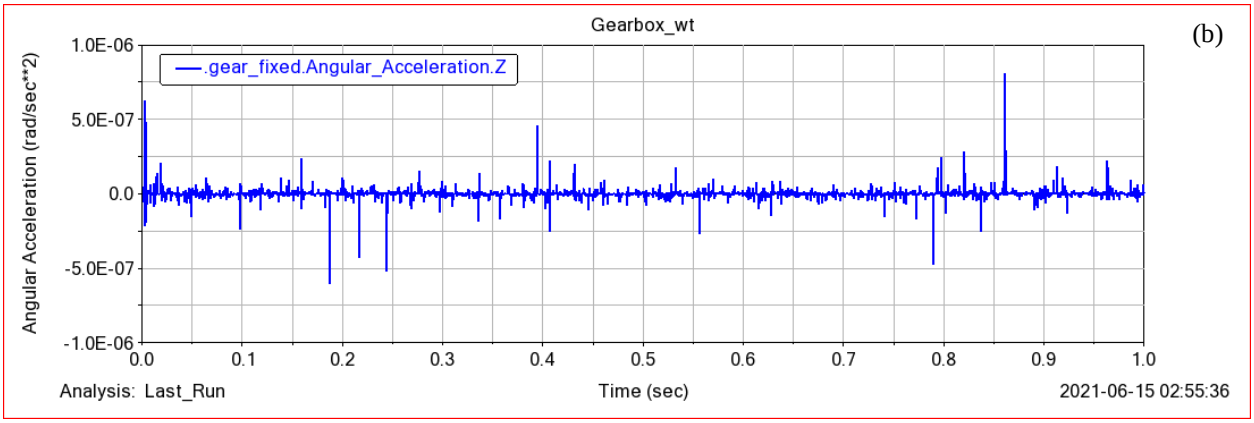

Figure 5.11 (a) The translation acceleration of the gear 2 (b) Angular acceleration of the gear 2

As shown in Figs 5.11 (a) and 5.11 (b) at the 10 rpm and load case 2, the maximum acceleration point is $0.257\ mm/s^2$ and also the second gear (pinion) has a maximum angular acceleration of $6.21 * 10^{-7} rad/s^2$. As the rotational speed of the pinion increase, the angular acceleration is also higher.

5.2.2.2 Second stage speed-up gears

At rotational wind speed 10 rpm and $\tau = 1.432 * 10^6\ Nm$, the second stage of the gearbox vibrational signals are shown in Figs 5.12 and 5.13. As depicted in Fig 5.12(a), the acceleration of gear 3 has a maximum point of $2.25 * 10^{-5}\ mm/s^2$ and maximum angular acceleration of $1.49 * 10^{-6}\ rad/s^2$. The pinion has also higher acceleration $5.37\ mm/s^2$ and angular acceleration $1.5 * 10^{-6}\ rad/s^2$.

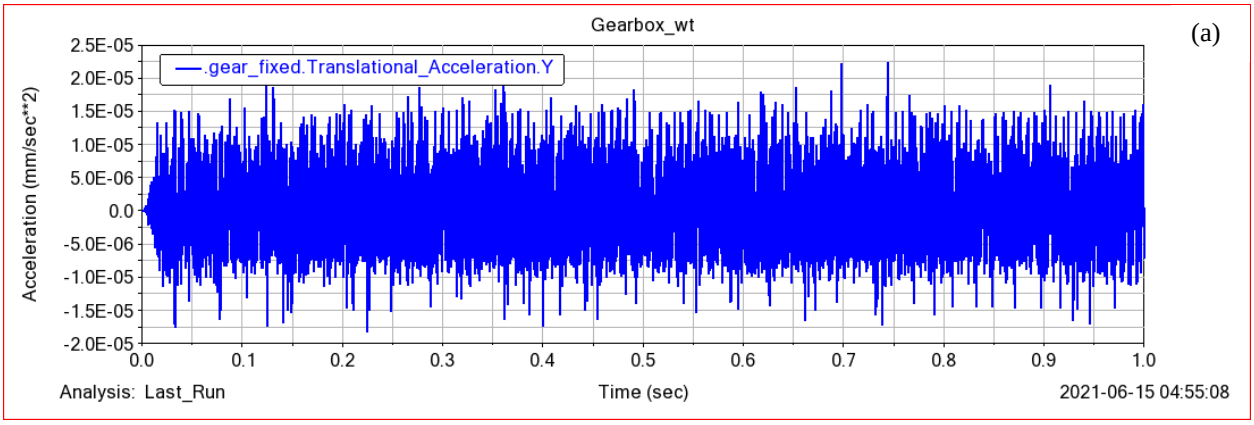

Figure 5.12 (a) The translation acceleration of the gear 3 (b) Angular acceleration of the gear 3

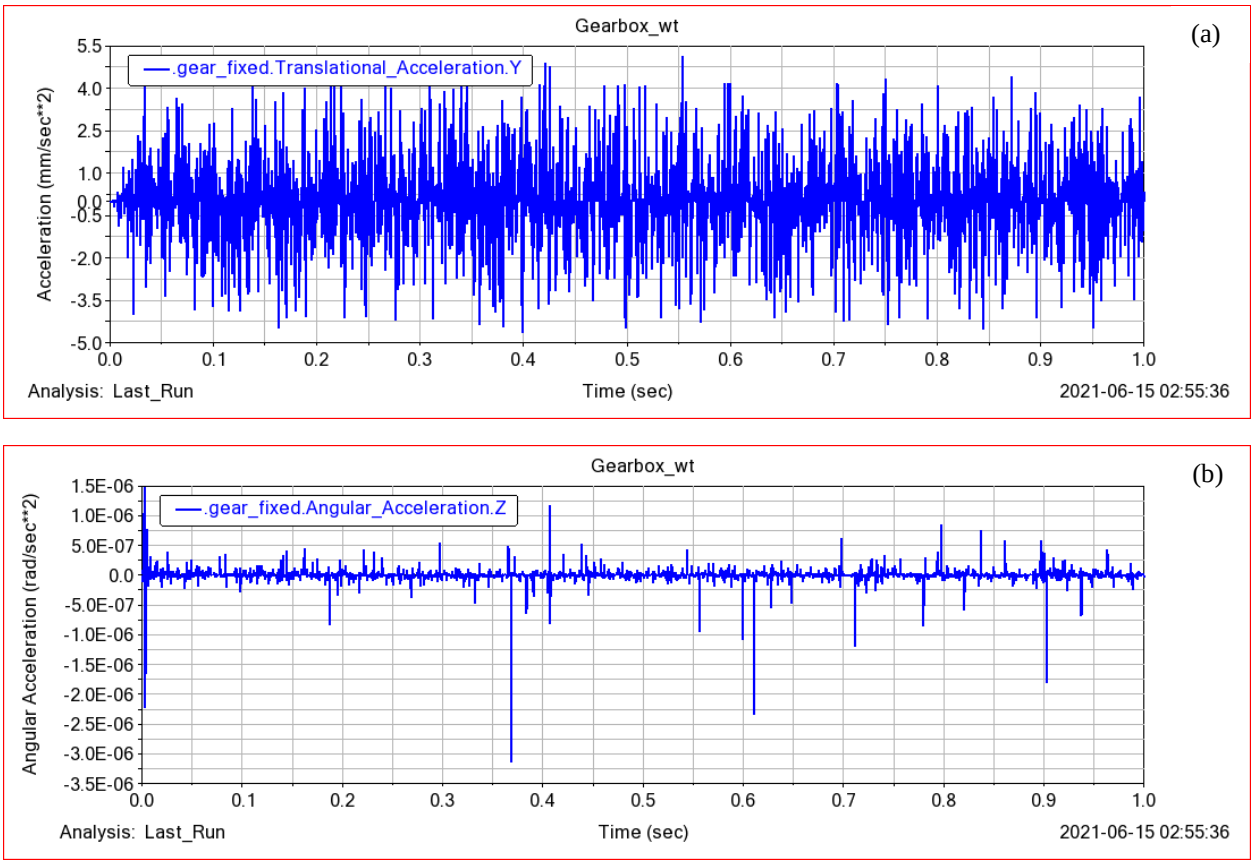

Figure 5.13 (a) The translation acceleration of the gear 4 (b) Angular acceleration of the gear 4

5.2.2.3 Planetary gears

To analyze the dependency of acceleration and angular acceleration vibration signal on the number of input revolutions, in this section, the selected input carrier revolution is 10 rpm and case2 load. The graphs show the three planet gears and sun gear vibration signals. To express the simulation results in this section also the chosen acceleration values are vertical axis y which is perpendicular to the axis of wind turbine gearbox rotation.

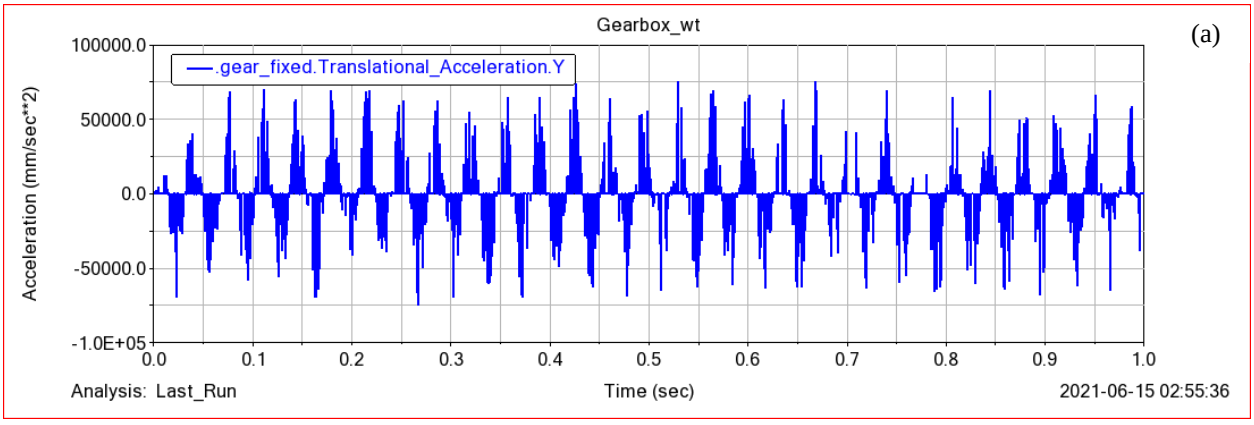

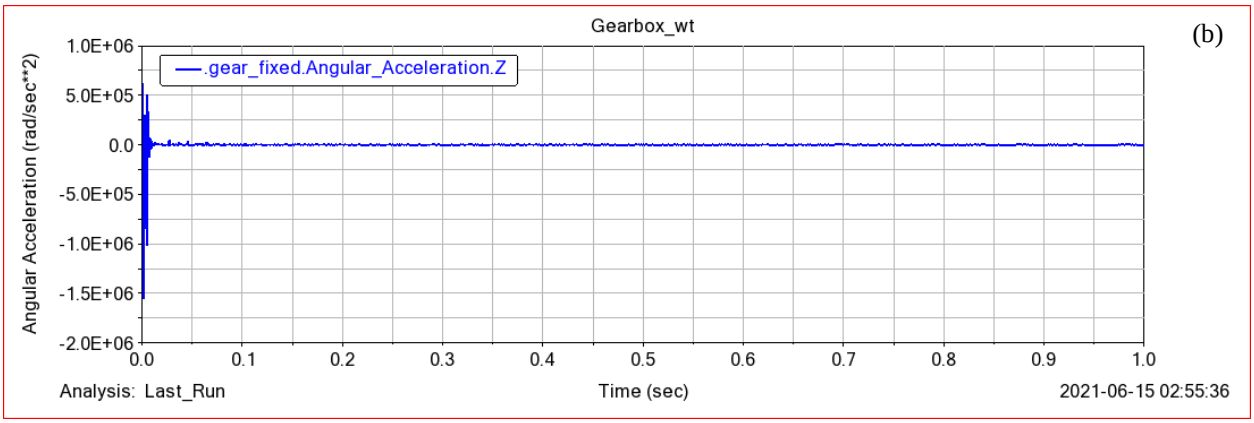

Figure 5.14 (a) The translation acceleration of the planet gear 1 (b) Angular acceleration of the planet gear 1

As shown in Fig 5.14(a) and (b), show the acceleration and angular acceleration vibration signal of the planet gear 3 at case 2. These graphical results have a maximum acceleration point of $8.75 * 10^4\ mm/s^2$ and angular acceleration point $6.1 * 10^5\ rad/s^2$. The angular acceleration is higher at the first rotations and gradually decreases through time.

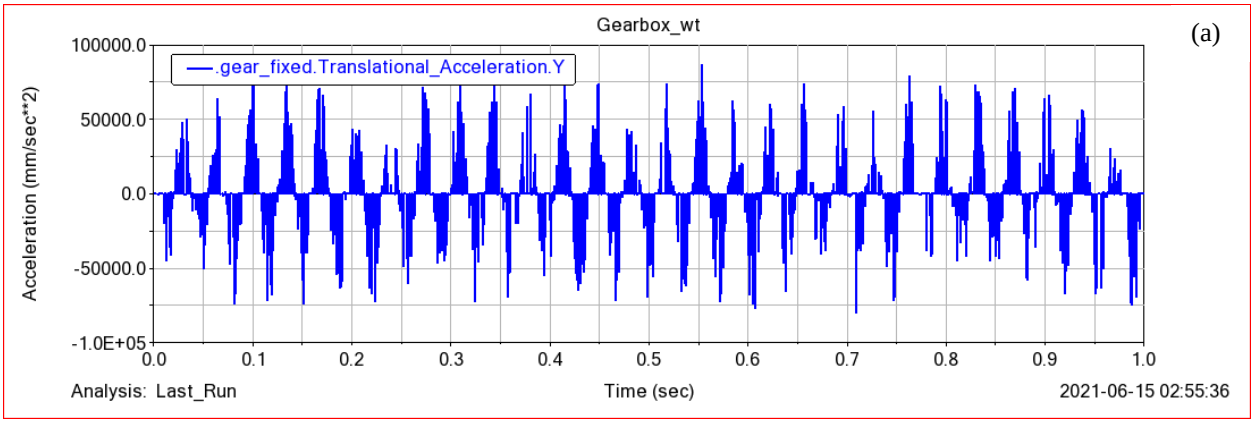

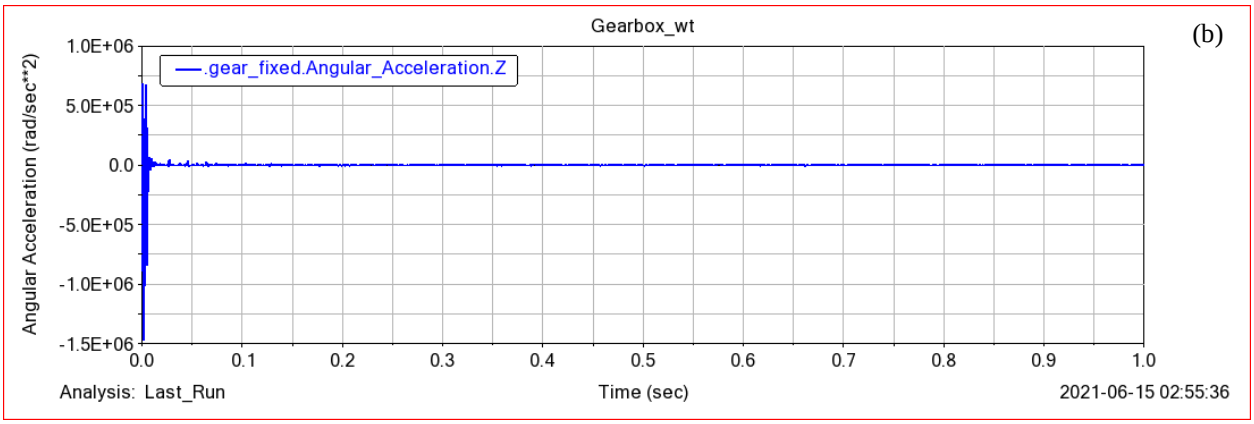

Figure 5.15 (a) The translation acceleration of the planet gear 2 (b) Angular acceleration of the planet gear 2

As shown in Figs 5.15 and 5.16, the vibration signal of acceleration and angular acceleration of the planet gear 2 and 3 respectively. The vibration signals of planet gear 2 and 3 are the same as planet gear 1 due to equal load sharing capacity between planets. In the second case, the planets are subjected to 10 rpm rotational speed and a load of a wind turbine. Though the planet's acceleration is higher due to the load of the turbine.

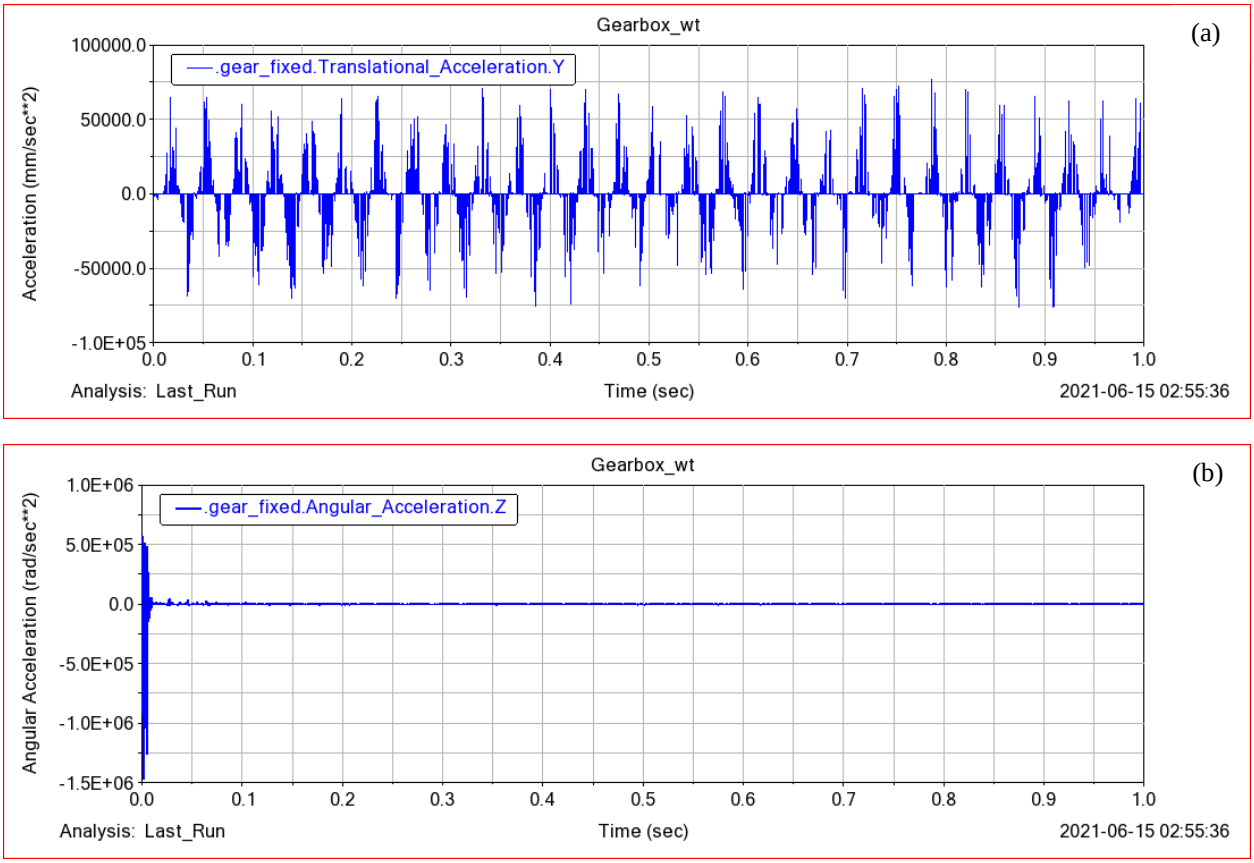

Figure 5.16 (a) The translation acceleration of the planet gear 3 (b) Angular acceleration of the planet gear 3

Figs 5.17(a) and (b) show that the sun gear has a minimum acceleration and angular acceleration vibration signal. The maximum point is $2.57 * 10^{-3}\, mm/s^2$ and $6.53 * 10^{-7}\, rad/s^2$ respectively. In addition, the sun gear is subjected to 10 rpm rotational speed and it meshes with the planet gears that are subjected to a wind turbine load. Though the sun gear accelerates due to the dynamic effect of the planet gears.

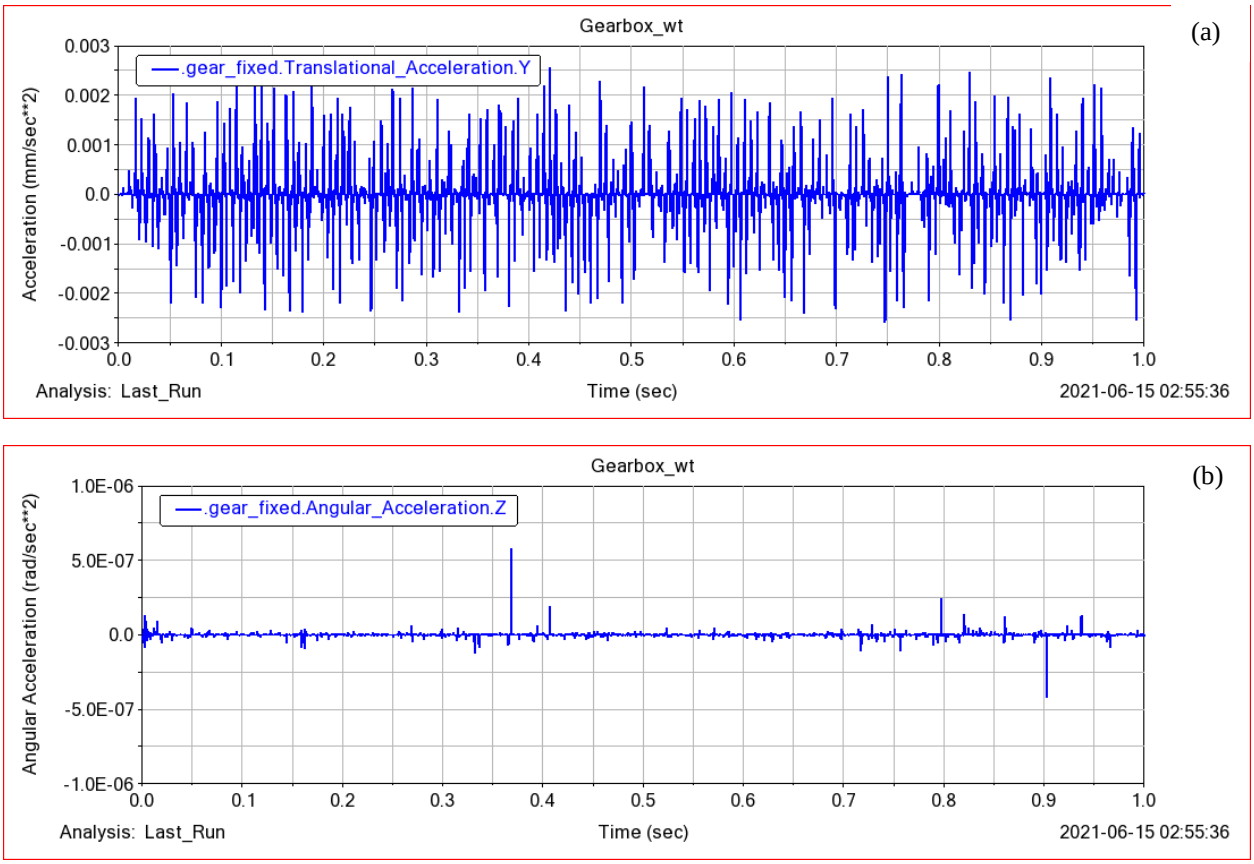

Figure 5.17 (a) The translation acceleration of the sun gear (b) Angular acceleration of the sun gear

5.2.3 Load Case-3 (rotational wind speed 20 rpm and $\tau_3 = 7.54 * 10^5\ Nm$)

In this section, the rotational vibration acceleration of all gears simulated at input rotational speed of 20 rpm and $\tau_3 = 7.54 * 10^5\ Nm$ by using ADAMS/ view. The graphs are shown in the following sections. The obtained vibration signals of first stage speed-up gears, second stage speed, and planetary gears are all in time domain spectra.

5.2.3.1 First stage speed-up gears

This sub-section shows translation and angular acceleration vibration signals of the first stage of the speed-up gear train at the case 3 input rotational wind speed and torque. As depicted in Fig. 5.18(a) the translational acceleration of the gear1 increased and decreased periodically with time. The radial acceleration of the first stage gears is shown in Figs. respectively while the figures for angular acceleration are also shown in fig. As given in Fig. 5.18(b), the first gear with the rotational speed of 20 rpm has maximum translational acceleration ($7.5 * 10^{-7} mm/s^2$) and maximum angular acceleration of $7.71 * 10^{-7} rad/s^2$ under load case 3. The second gear (pinion) also has a maximum acceleration point of $2.1\ mm/s^2$ and angular acceleration $2.85 * 10^{-5} rad/s^2$. As

depicted in graphs of figs 5.18 and 5.19, as the rotational speed of the pinion increase, the angular acceleration also becomes higher.

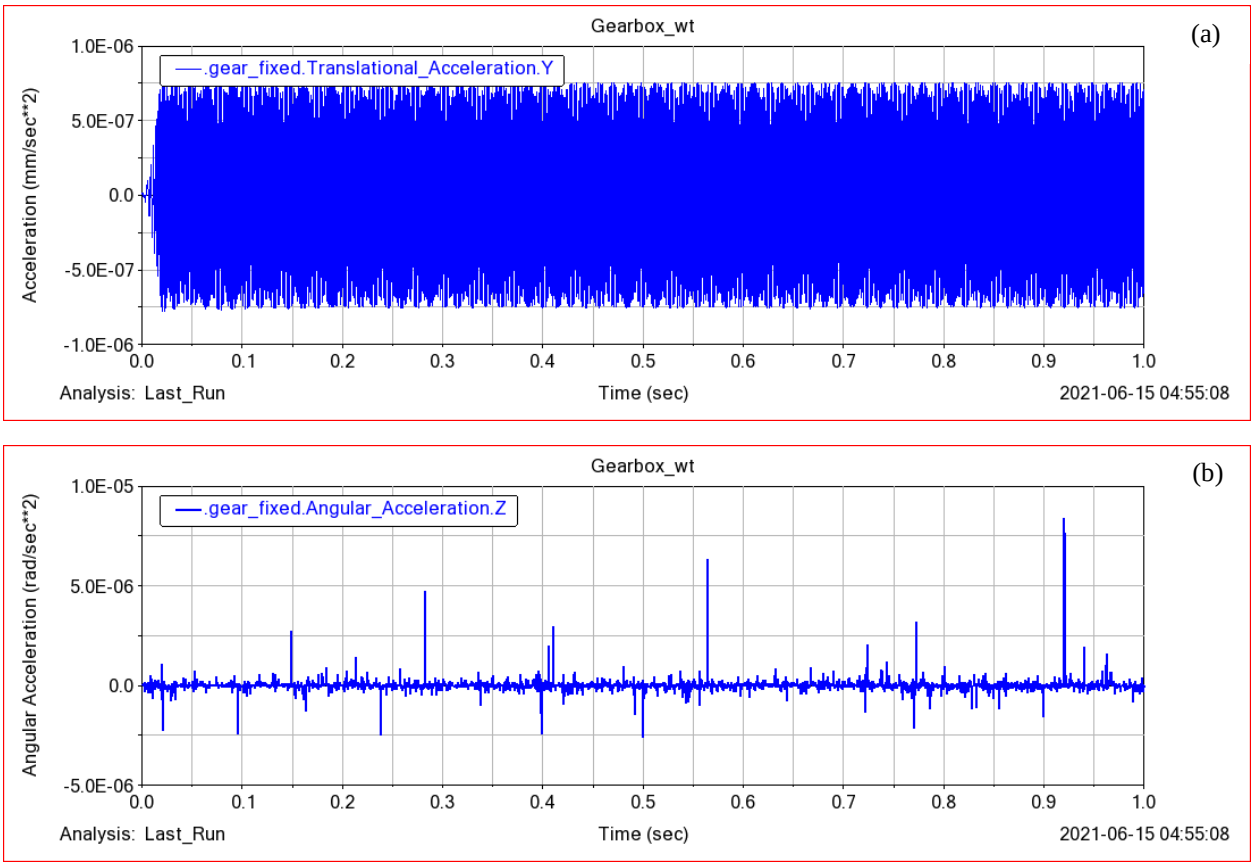

Figure 5.18 (a) The translation acceleration of the gear 1 (b) Angular acceleration of the gear 2

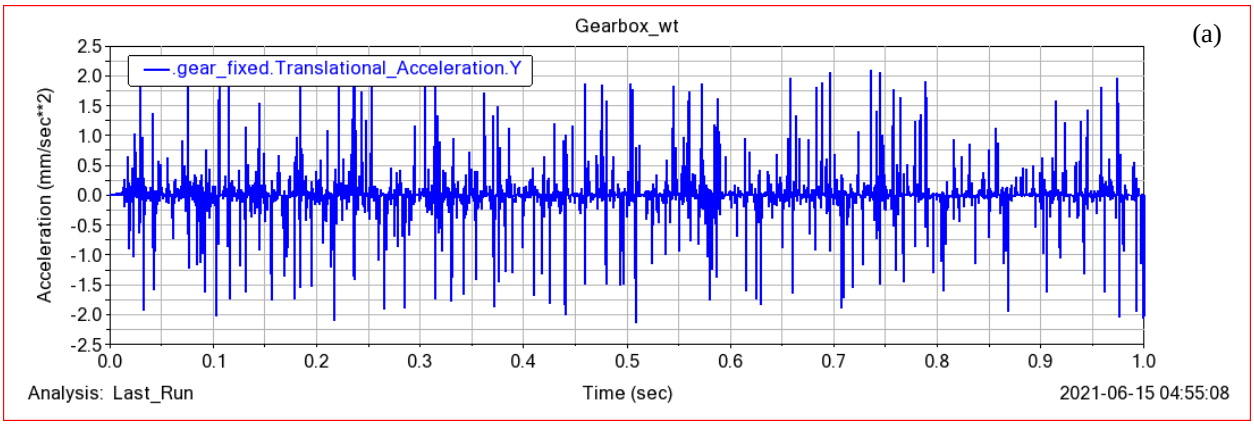

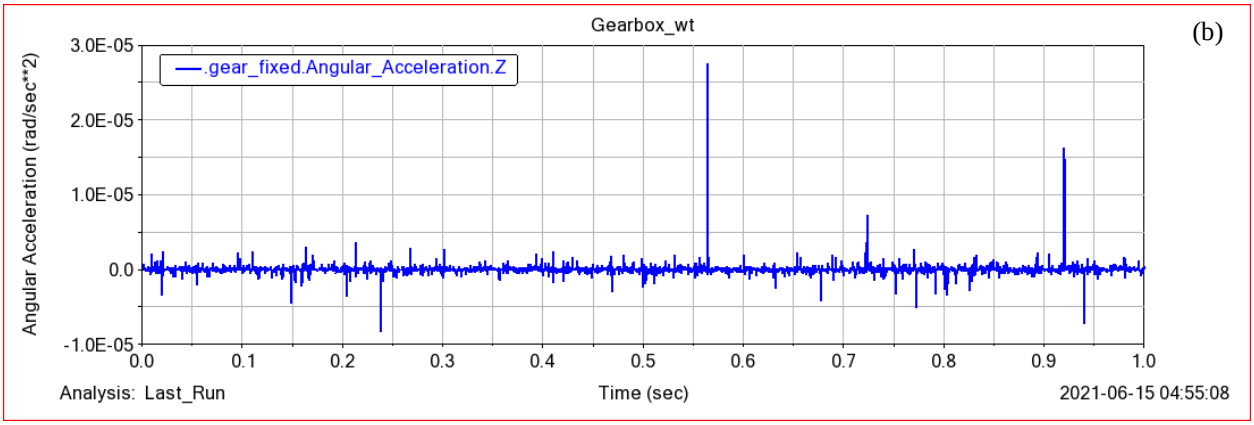

Figure 5.19 (a) The translation acceleration of the gear 2 (b) Angular acceleration of the gear 2

5.2.3.2 Second stage speed-up gears

At rotational wind speed 20 rpm and $\tau_3 = 7.54 * 10^5\ Nm$, the second stage gears vibration signals are shown in Figs 5.20 and 5.21. As depicted in Fig 5.20(a), the acceleration of gear 3 has a maximum point of $5.27\ mm/s^2$ and maximum angular acceleration of $2.78 * 10^{-5}\ rad/s^2$. The pinion has also higher acceleration $41.1\ mm/s^2$ and angular acceleration $1.04 * 10^{-4}\ rad/s^2$.

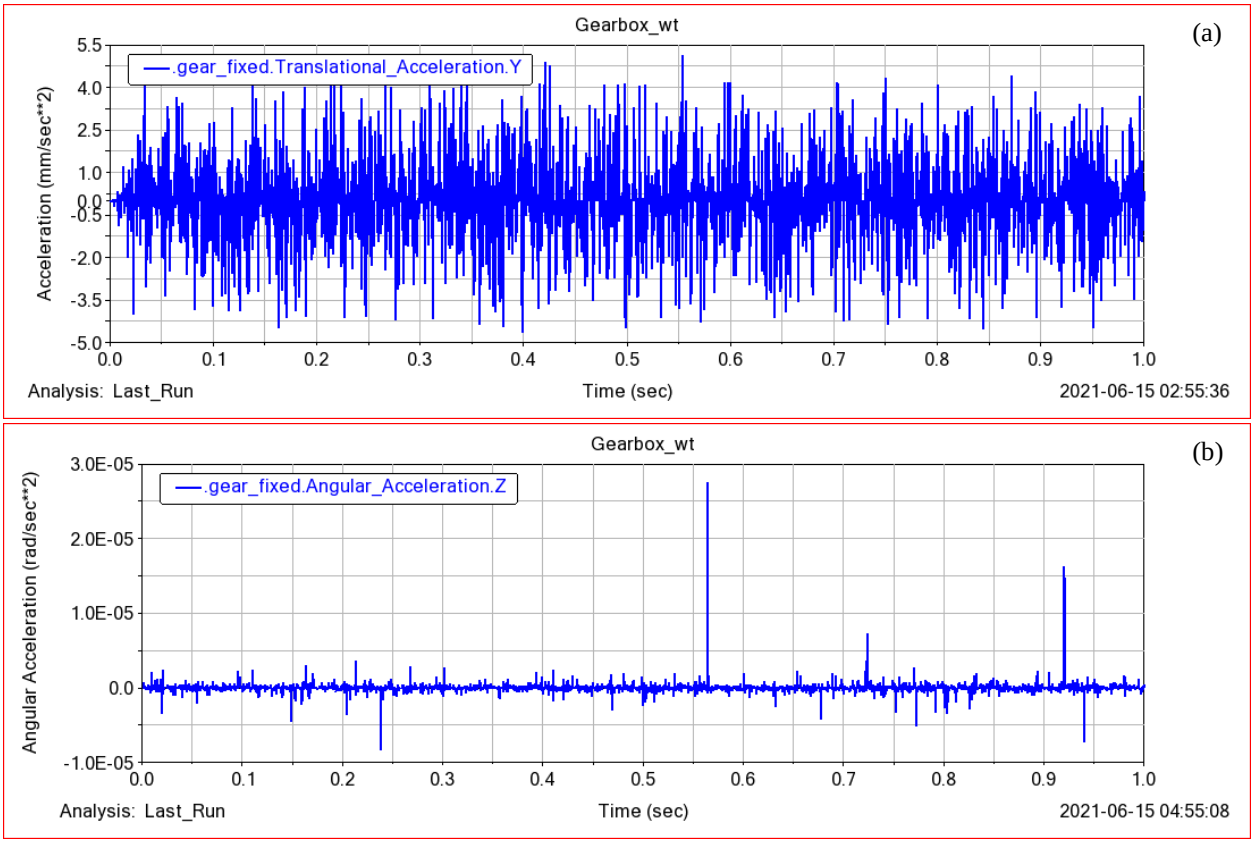

Figure 5.20 (a) The translation acceleration of the gear 3 (b) Angular acceleration of the gear 3

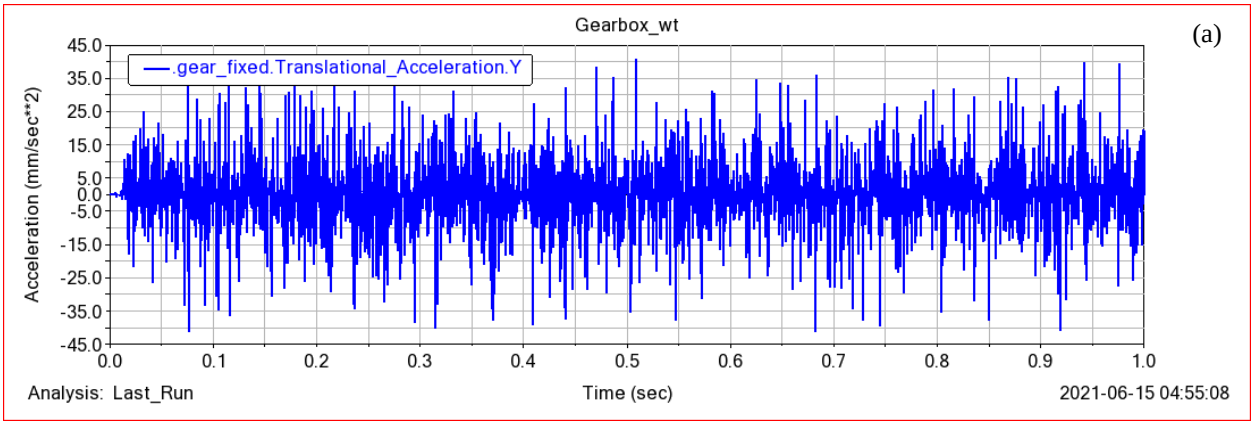

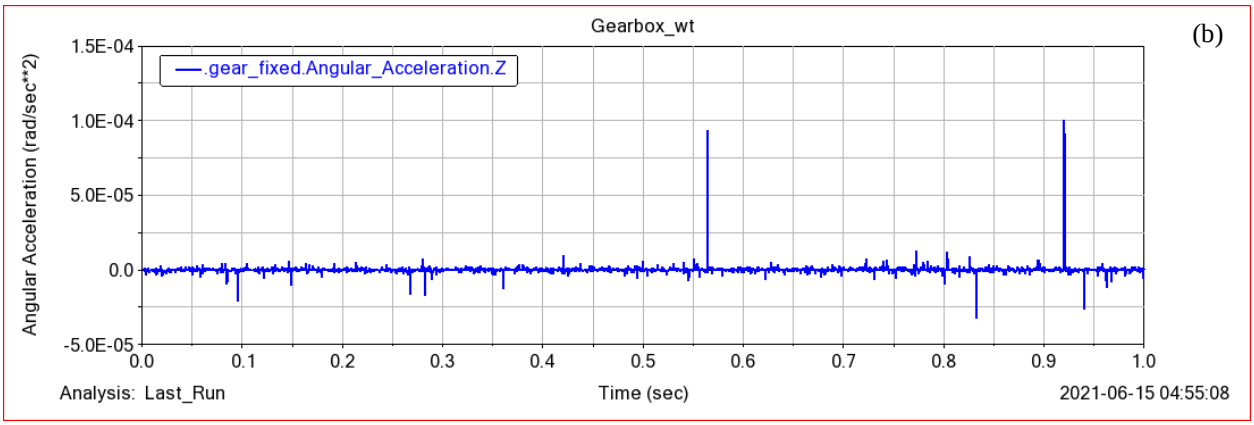

Figure 5.21 (a) The translation acceleration of the gear 4 (b) Angular acceleration of the gear 4

5.2.3.3 Planetary gears

In this sub-section, in case 3 the planetary gear train gears rotational vibration signals are shown in Figs 5.22 to Fig. 5.25. As depicted in Fig 5.22(a) and 5.22(b), the vibration signal of radial acceleration and angular acceleration of the planet gear 1 in the time domain responses. As shown in Fig. 5.22(a), the angular acceleration of the planet gear 1 at 20 rpm and load case 3 has a maximum point of $6.26 * 10^5\ mm/s^2$ and in Fig 5.22(b) the maximum angular acceleration point of the planet gear 1 is $1.0 * 10^7\ rad/s^2$.

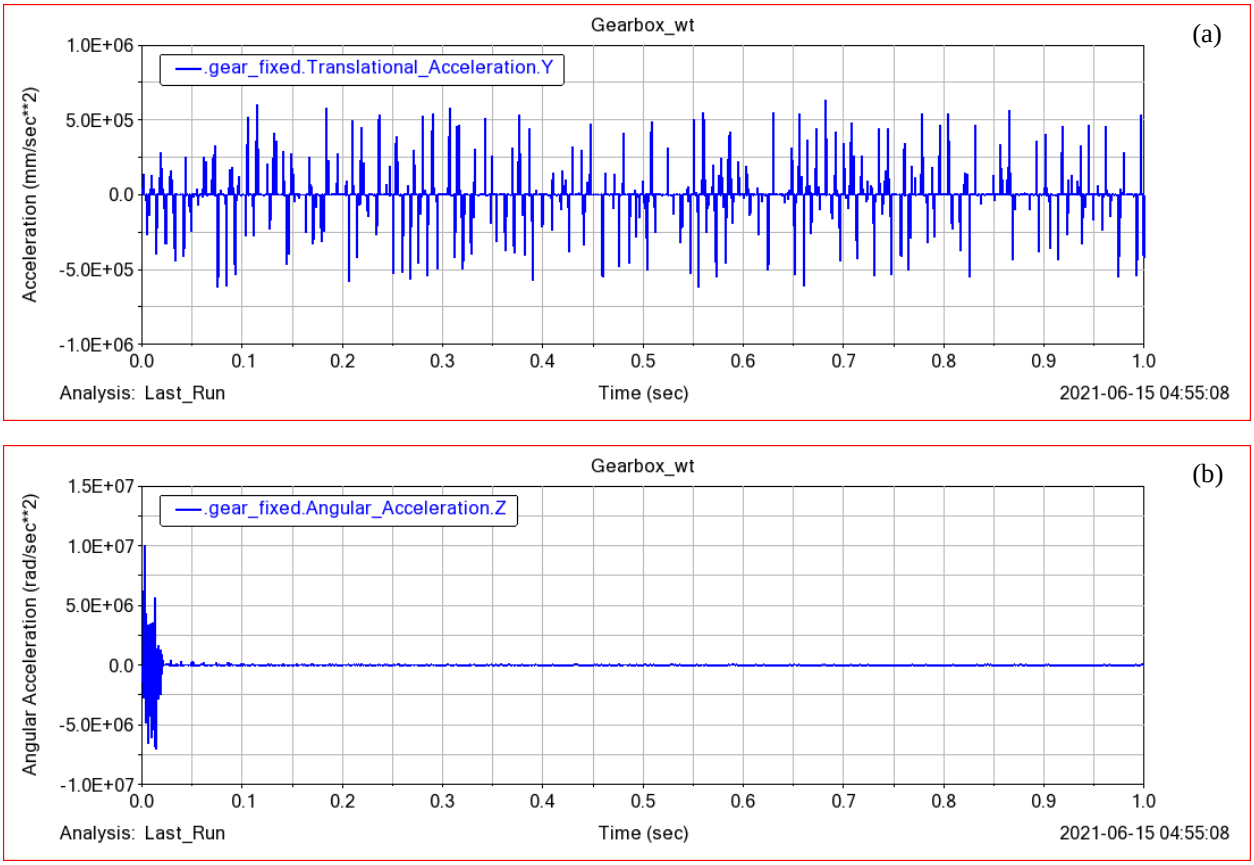

Figure 5.22 (a) The translation acceleration of the planet gear 1 (b) Angular acceleration of the planet gear 1

As shown in Figs 5.23(a) and (b), the vibration signal of acceleration and angular acceleration of the planet gear 2 and 3 respectively. The acceleration vibration signal has maximum point at $6.26 * 10^5\ mm/s^2$ which is equal with planet gear 1. But the angular acceleration vibration signal has a maximum value of $1.127 * 10^7\ rad/s^2$ which is greater than planet gear 1. In this case, the planets are subjected to 20 rpm rotational speed and in case 3 load of wind turbine, the planet gears angular acceleration vibration signal may vary as the input rotation speed increases.

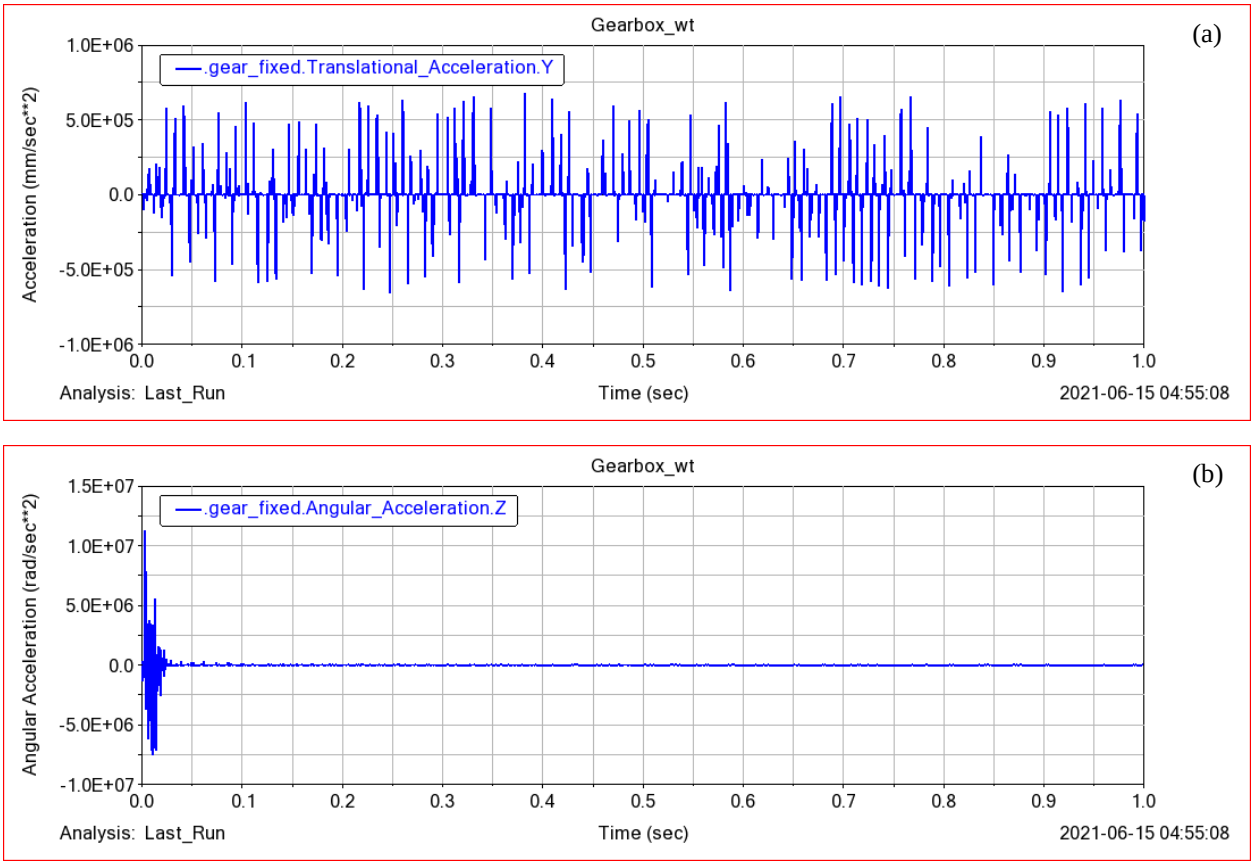

Figure 5.23 (a) The translation acceleration of the planet gear 2 (b) Angular acceleration of the planet gear 2

Figs 5.23(a) and (b) show planet gear 3 vibration signals. The angular acceleration has maximum point at $1.75 * 10^7\ rad/s^2$ at the first rotations and decrease through time. The acceleration vibration signal has maximum point at $6.26 * 10^5\ mm/s^2$ which is the same as planet gear 1 and 2. The acceleration vibration signal has equal values for three planet gears due to equal input rotational speed but the angular acceleration vibration signal may vary between planet gears.

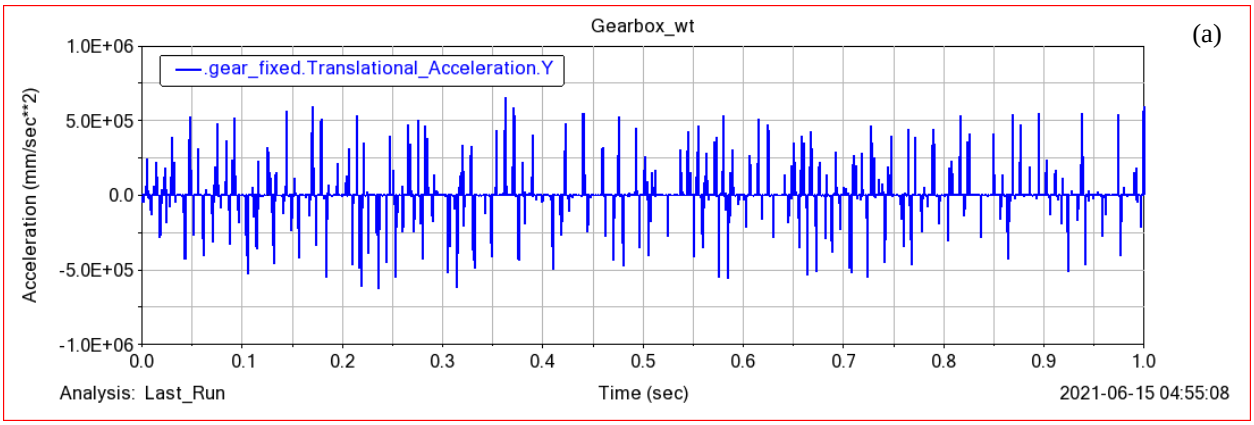

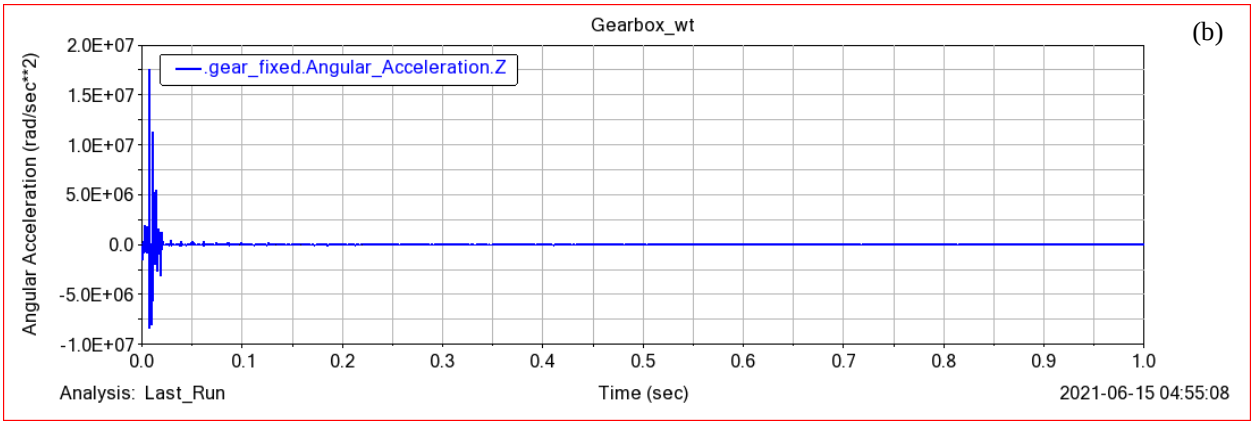

Figure 5.24 (a) The translation acceleration of the planet gear 3 (b) Angular acceleration of the planet gear 3

Figs 5.25 (a) and (b) show that the sun gear's acceleration and angular acceleration vibration signal at case 3. The maximum point is $2.11 * 10^{-2}\ mm/s^2$ and $8.49 * 10^{-6}\ rad/s^2$ respectively. In addition, the same as in other cases the sun gear is subjected to 20 rpm rotational speed and it meshes with the three planet gears that are subjected to a wind turbine load. Though the sun gear accelerates due to the dynamic effect of the planet gears.

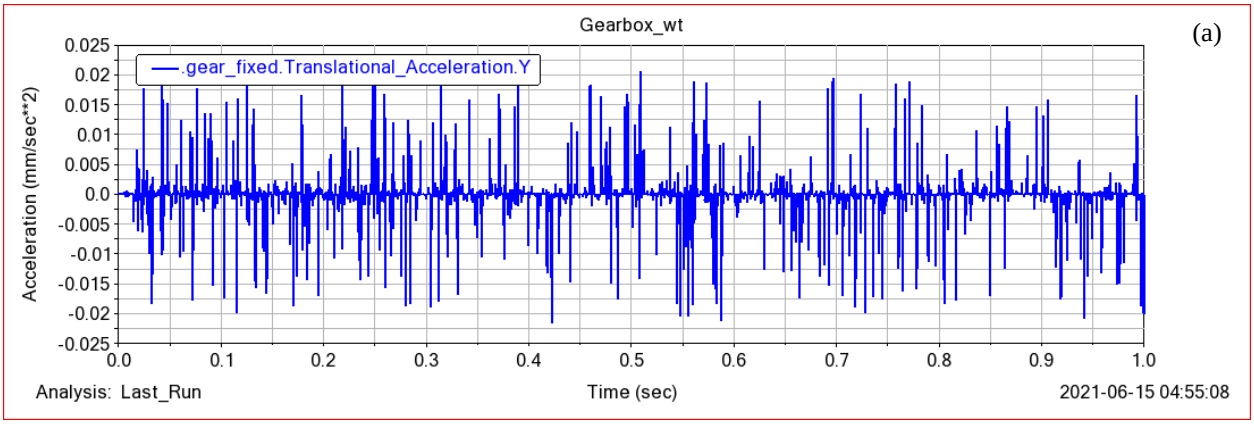

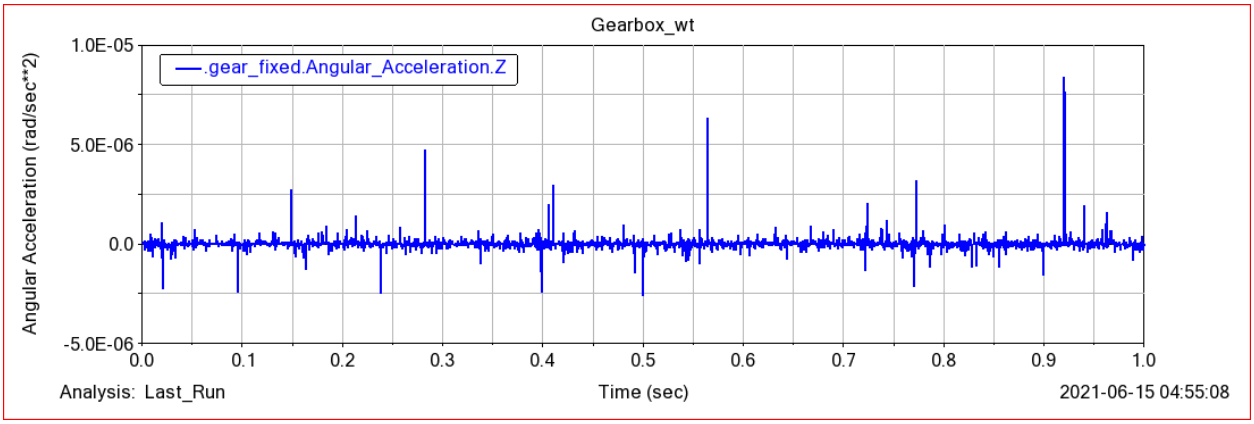

Figure 5.25 (a) The translation acceleration of the sun gear (b) Angular acceleration of the sun gear

5.2.4 Summary of the impact of rotational speed on vibration signal of the gears

In order to analyze the dependence of a vibration signal on the number of revolutions, the selected three input revolutions are 10 rpm, 15 rpm, and 20 rpm with three cases, $\tau_1 = 9.549 * 10^5$ Nm; $\tau_2 = 1.432 * 10^6$ Nm and $\tau_3 = 7.539 * 10^5$ Nm. This number of results are adequate for expressing the dependence. The speed variation is performed so that the vibration signature pattern can be determined for all gears in the drive train. The speeds selected for these three simulations are within the range of operation of the SE7715. A speed of 15 rpm, is in the mid operating range of the SE7715. And an input speed of 10 rpm, this is the initial operating range of the SE7715. An input speed of 20 rpm is within one the high end of the operating range during high-speed operations of the SE7715. As shown in Fig. 5.26, the vibration signal peak points of load case 3 is greater than load case 2 and load case 3, and the case which indicates the vibration signal is dependent on the variation of input rotational speed. As the rotational speed increases the vibrational signal also becomes higher.

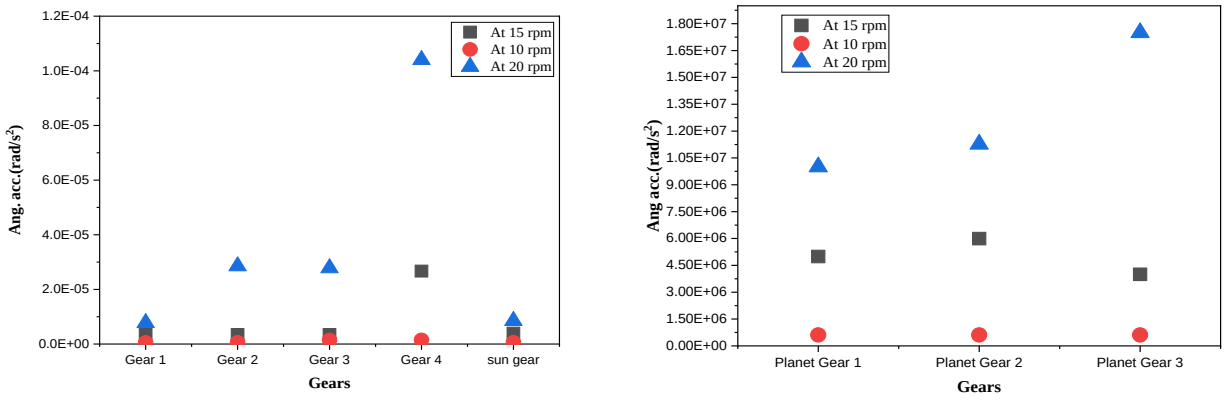

Figure 5.26 Comparison between input rotation speed on the gears angular acceleration

5.3 Impact of Rotational Speed on Gear Force

In this section, the drive train gears force was simulated in three different cases. These three cases are 10 rpm,15 rpm, and 20 rpm rotational speeds with different load cases. All cases are analyzed to determine the impact of rotational speed on the dynamic force of the gears model by the simulation created in Adams/view. The benefit of the wind turbine gearbox model allows for the analysis of the system according to what is expected to be the dynamic behavior of the system instead of using a simple static system approximation. The dynamic force was compared between the three cases at all gears in the drive train. The dynamic force shows variation in different cases.

5.3.1 Load Case-1 (rotational wind speed 15 rpm and $\tau_1 = 9.549 * 10^5\ Nm$)

In this section, the impact of rotational speed on gears dynamic force is simulated at 20 rpm and $\tau_1 = 7.54 * 10^5\ Nm$. All results are the output of ADAMS/view.

5.3.1.1 First stage speed-up gears

As shown in Fig. 5.27(a), the first stage gear has maximum radial force on a point of $1.01 * 10^8\ N$ and there are also some peaks shown to occur when the meshed gear tooth comes into contact with the other rigid pinion. In addition, as depicted in Fig. 5.27(b) the pinion has also a maximum radial force at $1.35 * 10^7\ N$. As the gear tooth meshes, the contact force increases between the gear and pinion but the contact force on the other mesh location decreases.

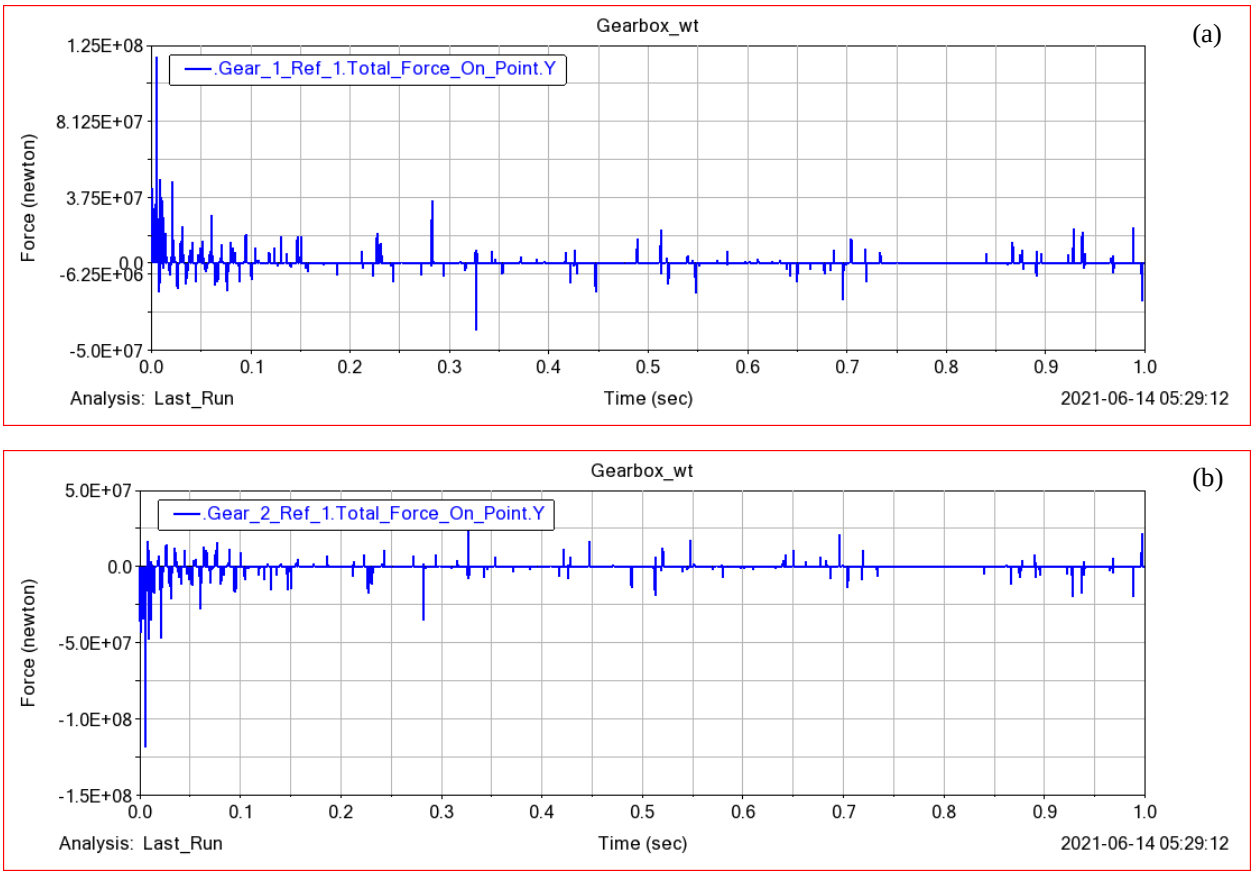

Figure 5.27 (a) Gear 1 radial force on a point (b) Gear 2 radial force on a point

5.3.1.2 Second stage speed-up gears

As depicted in Figs 5.28 (a) and (b) the second stage speed-up gears have more peak points than the first stage gears due to the speed increase creates more gear contact between gear and pinion.

In addition, the plotted graphs show the gear and pinion total force on a point at y-direction, the maximum peak points are $4 * 10^7\ N$ and $4.2 * 10^7\ N$ respectively.

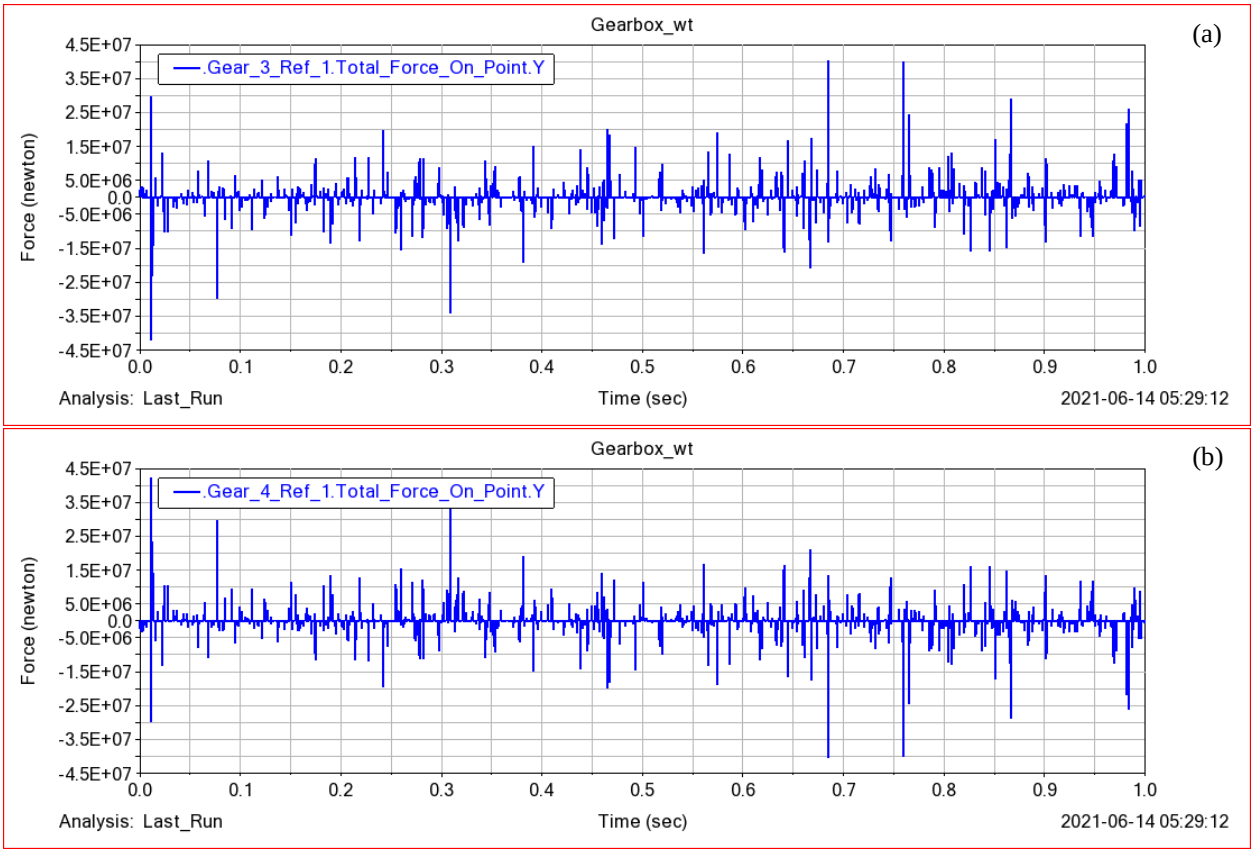

Figure 5.28 (a) Gear 3 radial force on a point (b) Gear 3 radial force on a point

5.3.1.3 Planetary gears

Figs. 5.29 show the contact force over one revolution of the sun and planet gears in the first stage within the drive train. The peaks shown happen when the meshed sun gear tooth comes into contact with the other rigid planets. As the tooth meshes, the contact force increases between the sun gear and that particular planet but the contact force on the other three mesh locations decreases.

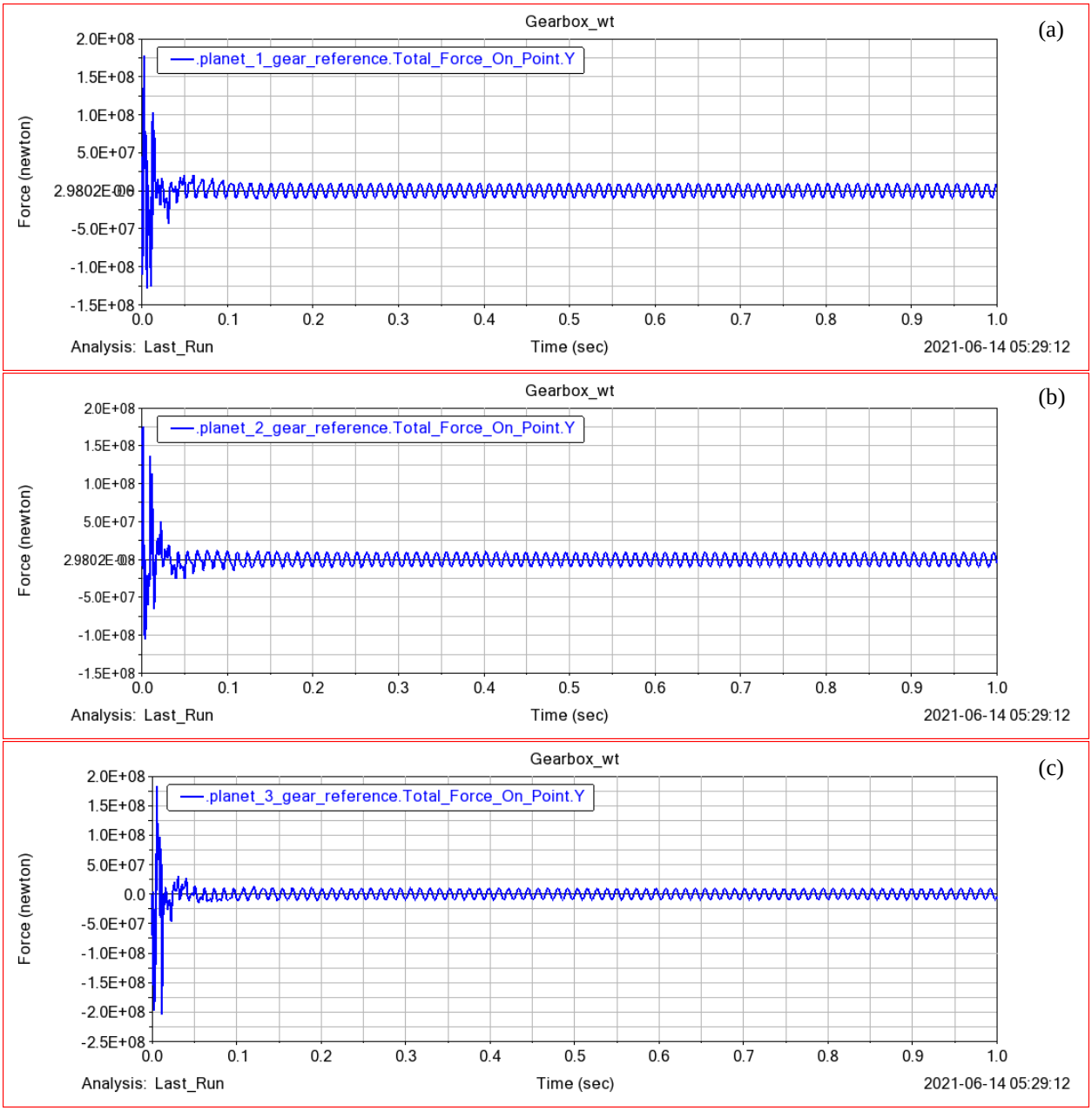

Figure 5.29 (a) Planet gear 1 radial force on a point (b) Planet gear 2 radial force on a point (c) Planet gear 3 radial force on a point

In this case, all planet gears have almost the same maximum total gear force on a point of $1.8 * 10^8\ N$ due to optimum load sharing between them. As depicted in Fig 5.30 the result creates an average force between the contact force ($5.25 * 10^7\ N$) to be relatively the same within the accuracy of the force measurement. The force profile is steady and consistent through a full rotation. This is shown in Fig. 5.30.

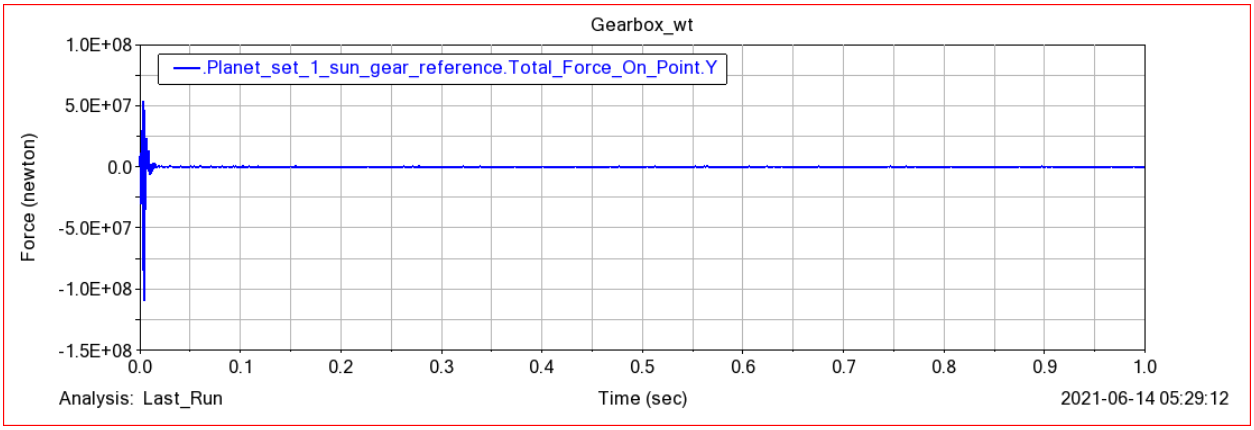

Figure 5.30 Sun gear radial force on a point

5.3.2 Load Case-2 (rotational wind speed 10 rpm and $\tau_2 = 1.432 * 10^6\ Nm$)

In this section, the impact of rotational speed on gears dynamic force is simulated at 10 rpm and $\tau_2 = 1.432 * 10^6\ Nm$. All results are the output of ADAMS.

5.3.2.1 First stage speed-up gears

Fig. 5.32(a) and (b) show the first stage gears' total radial force on a point. The maximum points of gear 1 and gear 2 radial forces are $7.5 * 10^7\ N$ and $1.0 * 10^7\ N$ respectively. There are also some peaks shown to occur when the meshed gear tooth comes into contact with the other rigid pinion. In addition, as depicted in Fig. 5.30 the gear and the pinion have equal and opposite maximum radial force applying on each other. As the same as case 1, gear tooth also meshes the contact force increases between the gear and pinion but the contact force on the other mesh location decreases.

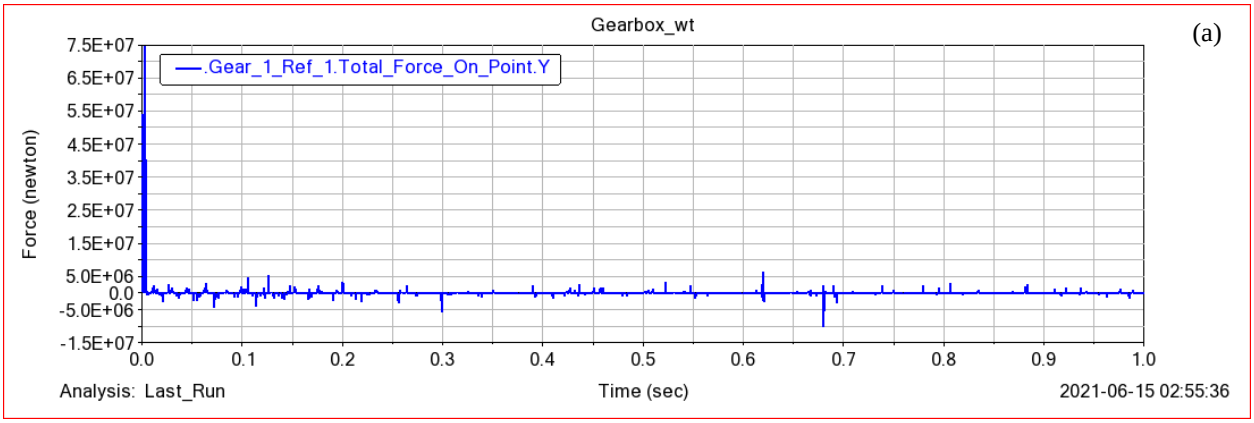

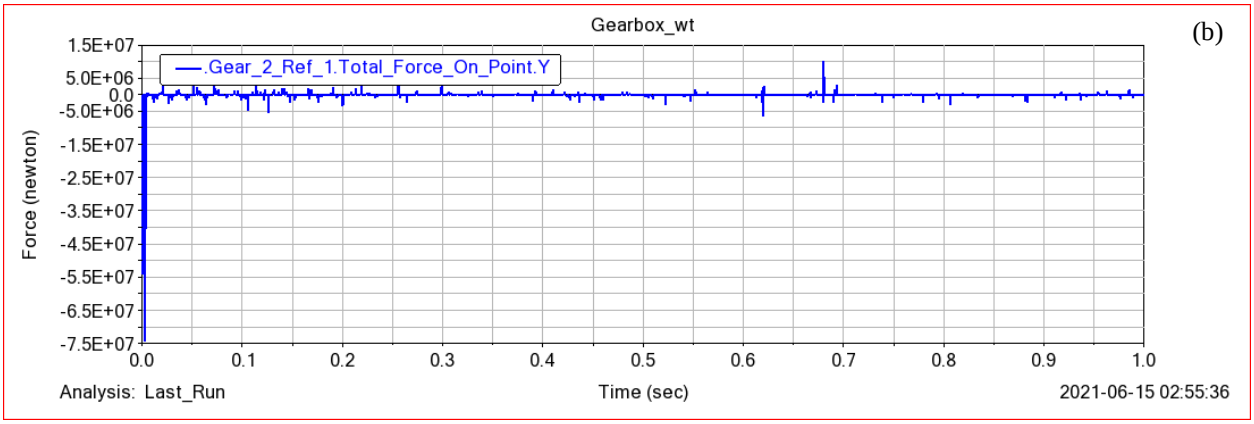

Figure 5.31 (a) Gear 1 radial force on a point (b) Gear 2 radial force on a point

5.3.2.2 Second stage speed-up gears

As shown in Figs 5.32 (a) and (b), in load case 2 the second stage speed-up gears have also more peak points than the first stage gears due to the speed increase creates more gear contacts between the gear and pinion. In addition, the plotted graphs show the gear and pinion maximum (peak) total force on a point at y-direction are $7.1 * 10^6\ N$ and $8.12 * 10^6\ N$ respectively.

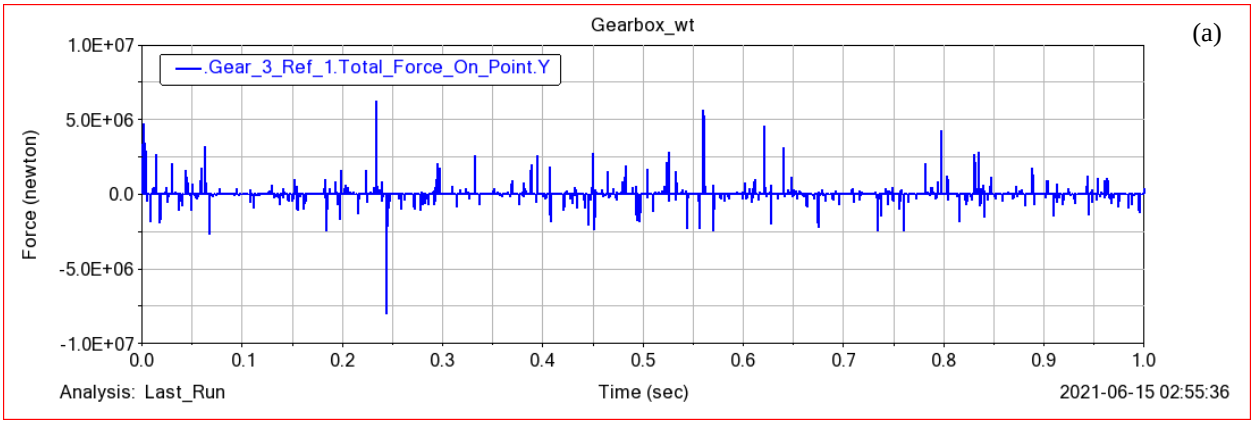

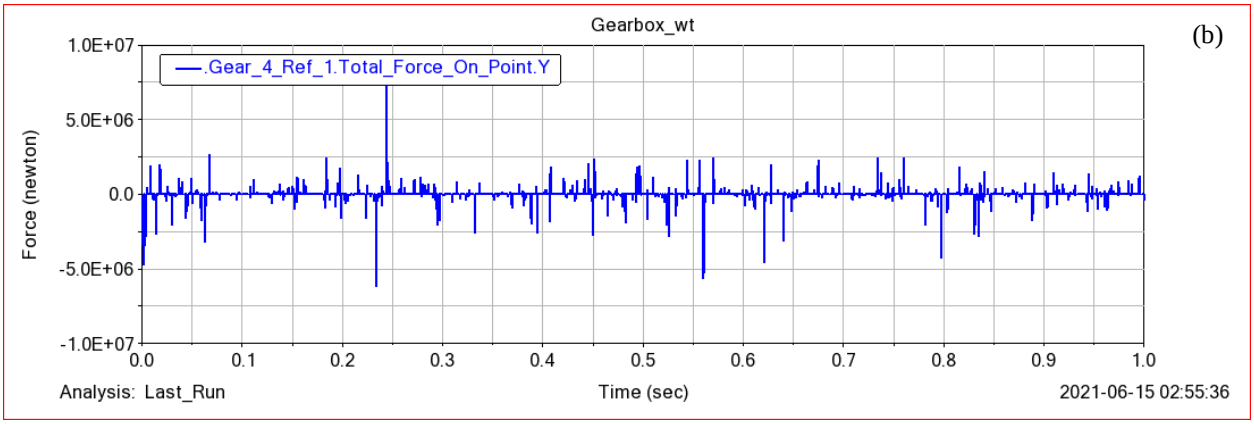

Figure 5.32 (a) Gear 3 radial force on a point (b) Gear 4 radial force on a point

5.3.2.3 Planetary gears

Figs. 5.33 (a), (b), and (c) show the planet gears' total force on point over one revolution of the sun and planet gears in the first stage within the drive train. The same as the other cases the peaks points of the graph are shown to occur when the meshed sun gear tooth comes into contact with the other three rigid planets. The maximum planet gears force happens at the start of rotation and reduces instantly, three planet gears have maximum peak points at $2.0 * 10^8\ N$, $9.1 * 10^7\ N$, and $2.98 * 10^8\ N$ respectively. As the tooth meshes, the contact force increases between the sun gear and that particular planet but the contact force on the other three mesh locations decreases.

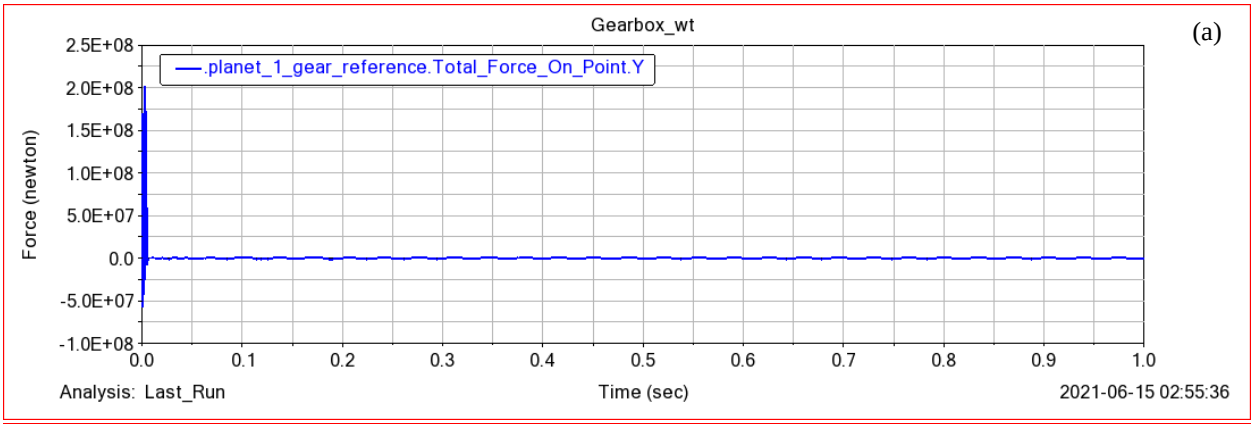

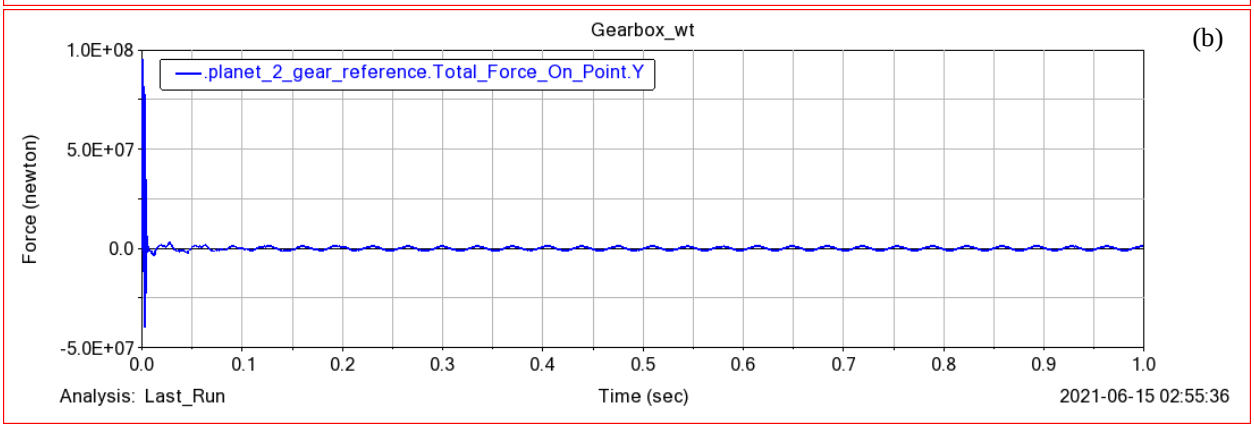

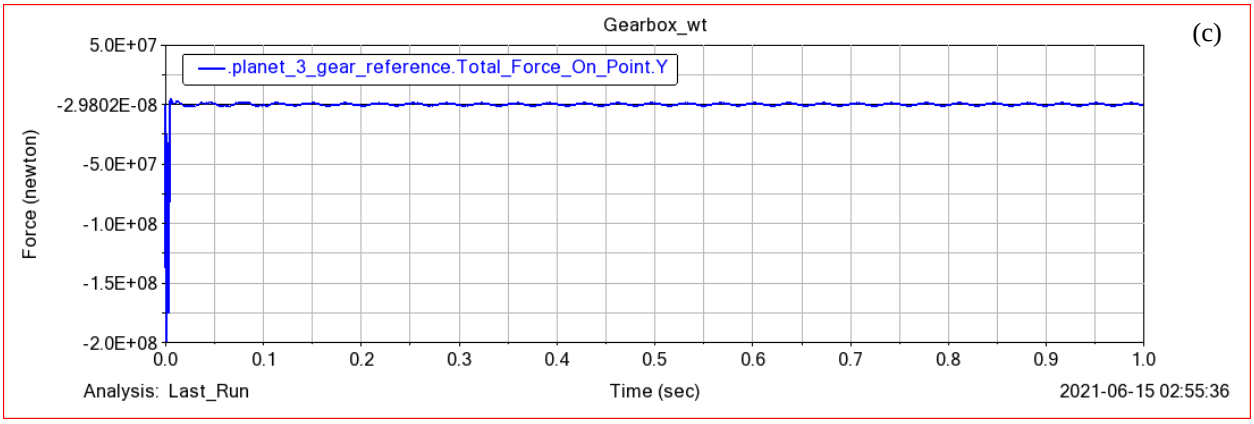

Figure 5.33 (a) Planet gear 1 radial force on a point (b) Planet gear 2 radial force on a point (c) Planet gear 3 radial force on a point

As depicted in Fig 5.34 peaks occur when the meshed sun gear tooth comes into contact with the other rigid planet gears. As the sun gear tooth meshes, the contact force increases between the sun gear and that particular planet but the contact force on the other three mesh locations decreases. The sun gear has maximum total force on a point at $7.01 * 10^6\ N$.

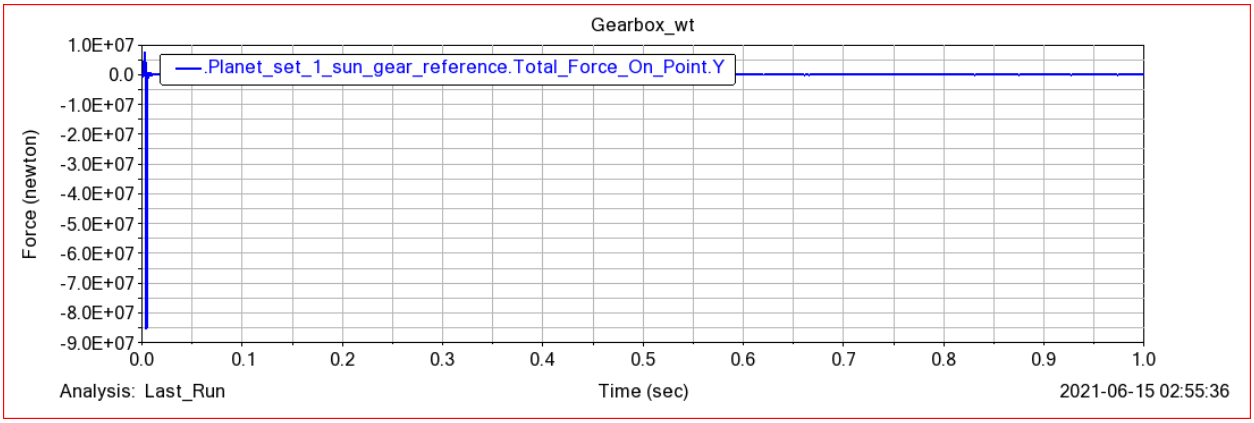

Figure 5.34 Sun gear radial force on a point

5.3.3 Load Case-3 (rotational wind speed 20 rpm and $\tau_3 = 7.54 * 10^5\ Nm$)

In this case, the impact of rotational speed on gears dynamic force is simulated at 20 rpm and $\tau_3 = 7.54 * 10^5\ Nm$. All results are the output of ADAMS/view.

5.3.3.1 First stage speed-up gears

As shown in Fig. 5.35 (a) and (b) the first stage gears total radial force on a point is simulated by ADAMS. The maximum radial force points of gear 1 and gear 2 are $6.124 * 10^7\ N$ and $6.01 * 10^7\ N$ respectively. In this case, there are also some peaks occur when the two meshed gear tooth comes into contact with the other rigid pinion. As depicted in Fig. 5.34 the gear and the pinion have equal and opposite maximum radial force applying on each other. As the same as other cases, gear tooth also meshes the contact force increases between the gear and pinion but the contact force on the other mesh location decreases.

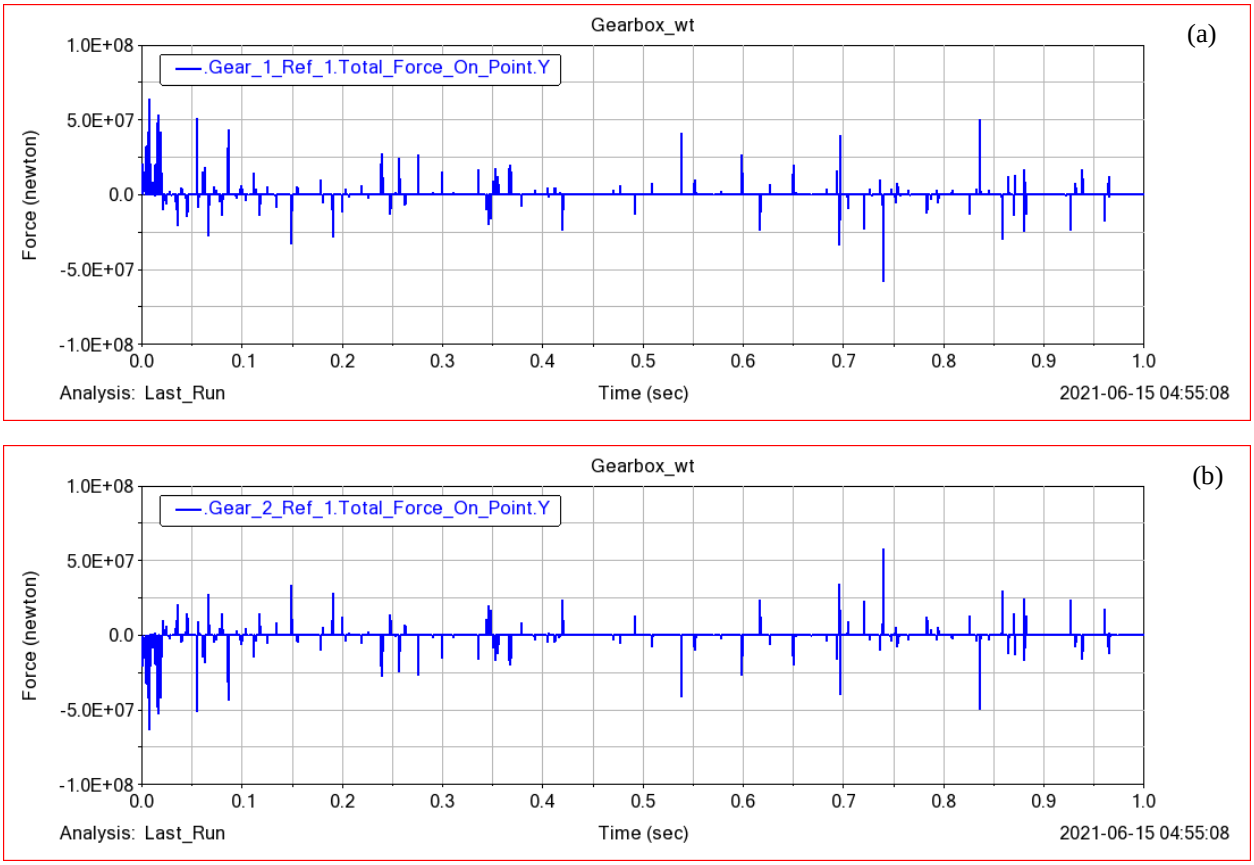

Figure 5.35 (a) Gear 1 radial force on a point (b) Gear 2 radial force on a point

5.3.3.2 Second stage speed-up gears

In Figs 5.36 (a) and (b) the plotted graphs show the second stage gear and pinion have a maximum (peak) total force on a point at a y-direction are $6.9 * 10^7\ N$ and $5.5 * 10^7\ N$ respectively. As the same as other cases, the second stage speed-up gears have more maximum peak points than the first stage gears due to the speed increase creates more gear contacts between the gear and pinion.

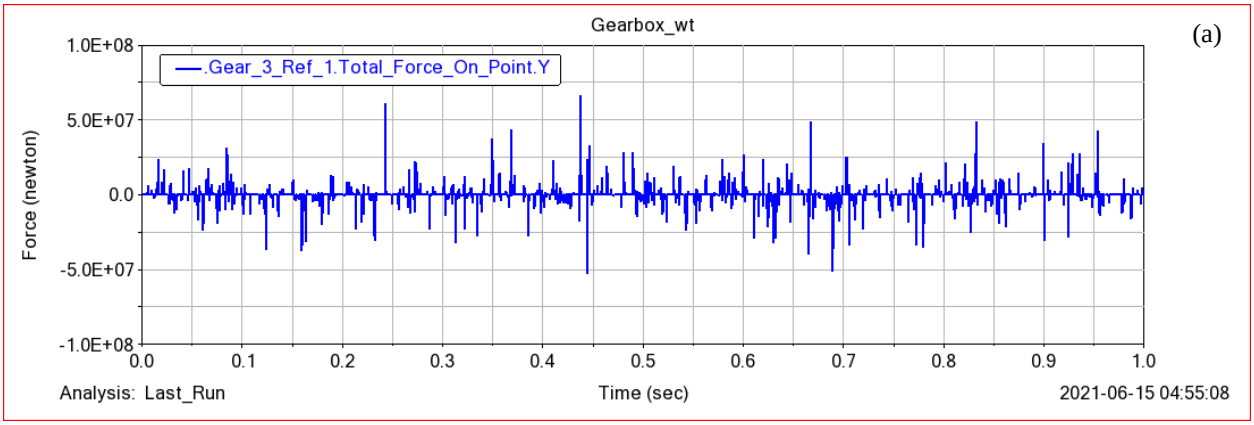

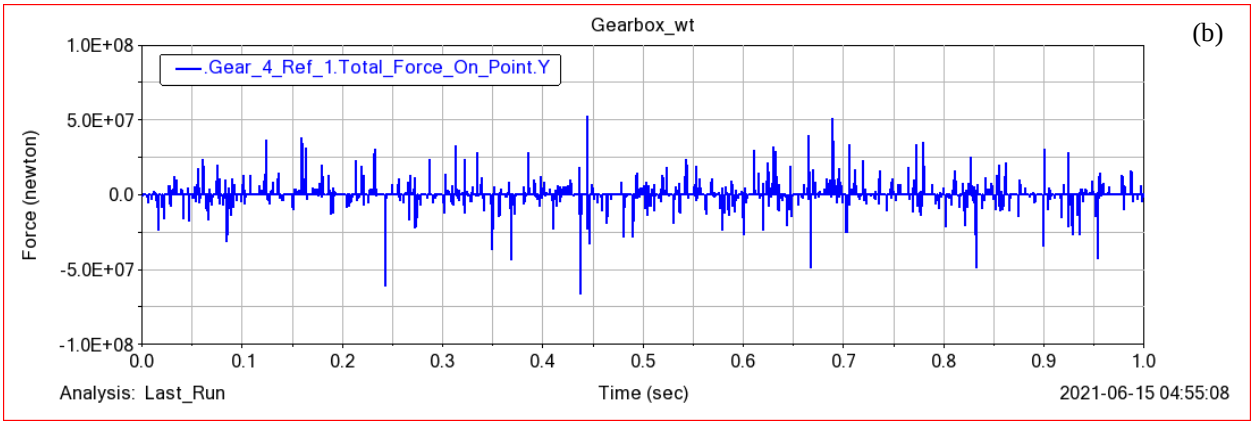

Figure 5.36 (a) Gear 1 radial force on a point (b) Gear 2 radial force on a point

5.3.3.3 Planetary gears

Figs. 5.37 (a), (b), and (c) show the three planet gears total force on a point, maximum peak points are $2.126 * 10^8\ N$, $2.1 * 10^8\ N$, and $2.0 * 10^8\ N$ respectively. These are planet gears' total force on point over one revolution of the sun and planet gears in the first stage within the drive train. The same as the other cases the peak points of the graph are shown to occur when the meshed sun gear tooth comes into contact with the other three rigid planets. The maximum planet gears force happens at the start of rotation and reduces instantly, As the tooth meshes, the contact force increases between the sun gear and that particular planet but the contact force on the other three mesh locations decreases.

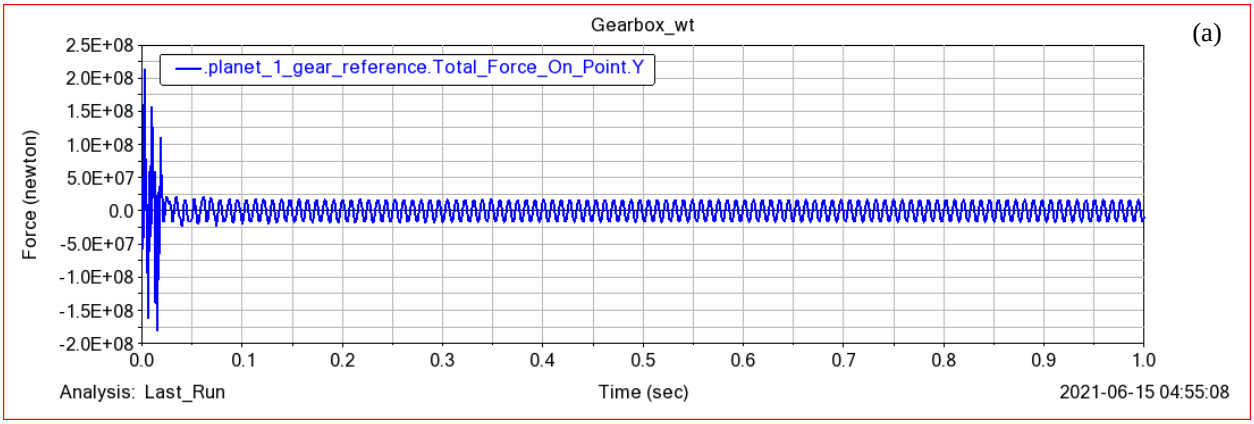

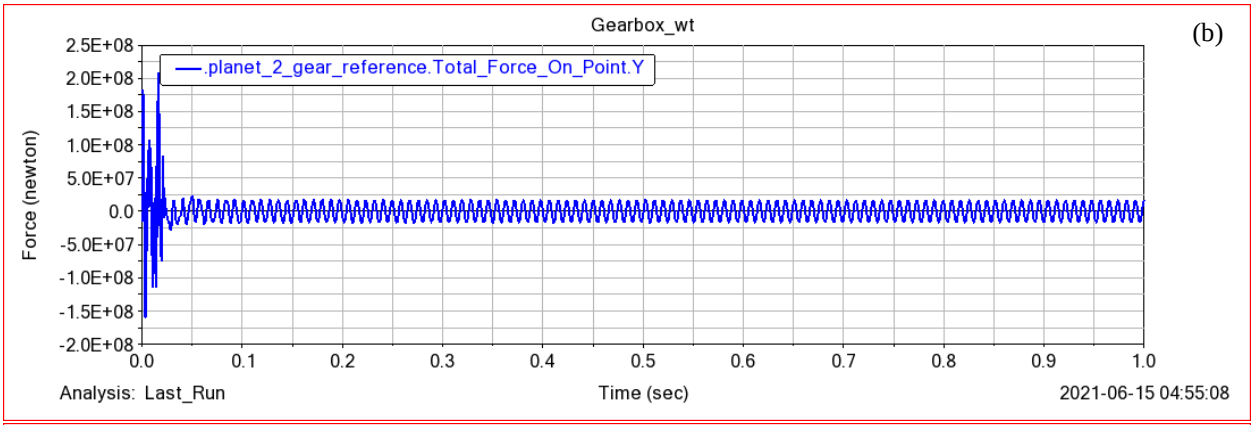

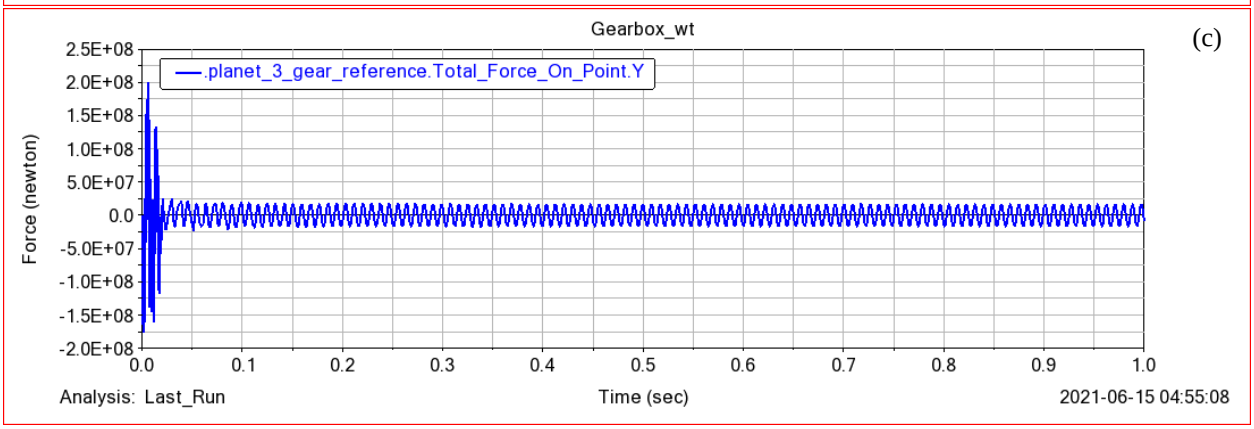

Figure 5.37 (a) Planet gear 1 radial force on a point (b) Planet gear 2 radial force on a point (c) Planet gear 3 radial force on a point

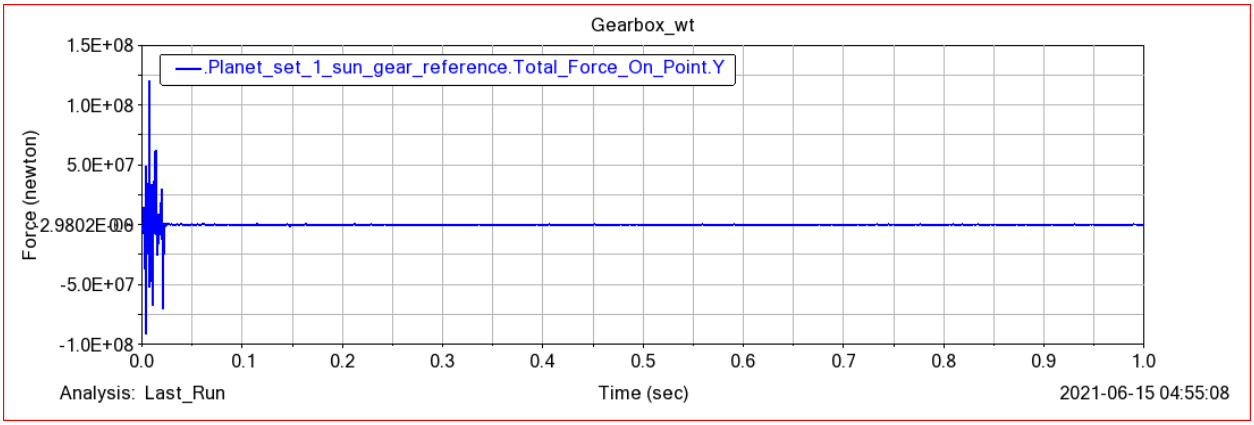

Figure 5.38 Sun gear radial force on a point

The sun gear total force on a point has plotted the series of planet gear contact locations as shown in Fig. 5.38. These include all contact definitions within the Adams model created. The contact force between the sun gear and planet gears teeth is the dynamic force model by the simulation created in Adams. In load case 3 the sun gear has maximum total force on a point at $1.9 * 10^8\ N$.

As the gear tooth meshes, the contact force increases between the sun gear and that particular planet gear but the contact force on the other three mesh locations decreases.

5.3.4 Summary on the impact of input rotational speed variation on gear force

In this sub-section, the speeds selected for these three simulations are within the range of operation of the SE7715. A speed of 1.508 rad/sec is equivalent to 15 rpm, this is in the mid operating range of the SE7715. And an input speed of 1.0053 rad/s is equivalent to 10 rpm, this is the initial operating range of the SE7715. An input speed of 2.0106 rad/sec corresponds to 20 rpm which is within one the high end of the operating range during high-speed operations of the SE7715. This number of results is adequate for expressing the dependence. As shown in Fig. 5.39, The results comparison is expressed by the selected maximum peak points of force values at vertical axis y for all gears with different input rotation speeds. At input rotation of 20 rpm, there are higher maximum peak points than other input rotational speeds. The higher the number of input carrier revolutions, the higher the total gear force on a point of gears.

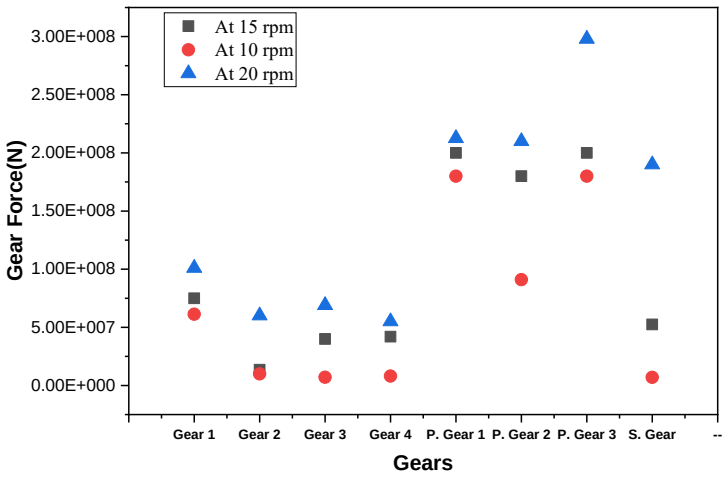

Figure 5.39 Summary of the impact of input rotational speed variation on gear force

CHAPTER SIX

6. Vibration Analysis through FFT

6.1 Introduction

The wind turbine gearbox dynamic simulation graphs are analyzed through Fast Fourier Transform, FFT, which is a method of signal analysis that filters an input signal and outputs its frequency components. An FFT takes an incoming signal, usually a signal in time, and uses a mathematical algorithm to isolate individual sinusoidal signals and display them in frequency space. In this chapter, the first section is about the gear mesh frequencies of components of the gearbox. The second and third section demonstrates the impact of rotational speed on acceleration and force vibration signal. The input rotational speeds are 10-rpm (1.0053 rad/s), the 15-rpm (1.508 rad/s), and 20-rpm (2.0106 rad/s) with three load cases.

6.2 Gear Mesh Frequencies (GMF)

In addition to their fundamental rotational frequencies, meshing gears produce a vibration which is the product of the number of teeth and their rotational frequency and it's also an indication of the gearbox conditions. Generally, GMF also called "tooth mesh frequency" is the rate at which gear teeth mesh together in a gearbox. It is equal to the number of teeth on the gear times the rotation speed of the gear.

$$f_m = N * T \qquad \textit{Eqn.6.1}$$

Where, f_m is gear mesh frequency, N is the rotational speed of the first and second stage speed up gear, T is the number of teeth.

For planetary gear mesh frequency,

$$N_0 = N_s/\left((T_r/T_s) + 1\right) \qquad \textit{Eqn.6.2}$$

$$N_p = N_0(T_r/T_P) \qquad \textit{Eqn.6.3}$$

$$\text{Then, } f_{m1} = T_s(N_s - N_0) = T_r * N_0 = T_p * N_p \qquad \textit{Eqn.6.4}$$

Where N_0, N_s, and N_p are input carrier, sun gear, and planet gear rotational speeds, T_r, T_P, and T_s are the number of teeth of the ring gear, planet gear, and sun gear respectively.

The number of teeth on the drive gear multiplied by the speed of the drive gear must equal the number of teeth on the driven gear times the speed of the driven gear. As the pinion rotates against the driven gear, the individual cycles of the frequency generated are a profile of the individual teeth meshing. Gear mesh frequencies of gears in the gearbox were calculated as follows.

Table 6-1 The GMF at the 10-rpm (1.0053 rad/s) input on the planet carrier

Description	Gear	Number of teeth	Gear mesh frequency values
Planetary gear system	Sun	21	$f_{m1} = 99.54$ Hz
	Planet	39	
	Ring	99	
1st stage gears	Drive gear	82	$f_{m2} = 471$ Hz
	Driven gear	23	
2nd stage gears	Drive gear	76	$f_{m3} = 1556.3$ Hz
	Driven gear	23	

Table 6-2 The GMF at the 15-rpm (1.508 rad/s) input on the planet carrier

Description	Gear	Number of teeth	Gear mesh frequency values
Planetary gear system	Sun	21	$f_{m1} = 149.31$ Hz
	Planet	39	
	Ring	99	
1st stage gears	Drive gear	82	$f_{m2} = 706.53$ Hz
	Driven gear	23	
2nd stage gears	Drive gear	76	$f_{m3} = 2334.5$ Hz
	Driven gear	23	

Table 6-3 The GMF at the 20-rpm (2.0106 rad/s) input on the planet carrier

Description	Gear	Number of teeth	Gear mesh frequency values
Planetary gear system	Sun	21	$f_{m1} = 199.08$ Hz
	Planet	39	
	Ring	99	
1st stage gears	Drive gear	82	$f_{m2} = 942$ Hz
	Driven gear	23	
2nd stage gears	Drive gear	76	$f_{m3} = 3112.6$ Hz
	Driven gear	23	

6.3 Varying input speed vibration signal tests

6.3.1 Speed-up gear stage

The first set of simulations in ADAMS were performed at steady-state conditions using an input velocity at the first stage of 1.0053 rad/sec, 1.508 rad/sec, and 2.0106 rad/sec. The same analysis was performed on the model at three different speeds above and below 1.508 rad/sec. The speeds chosen were 1.0058 rad/sec and 2.0 rad/sec.

The first model to be observed is a first stage and second stage gears model. The model was simulated for one-quarter turn on the input over 1000 steps with an input speed of 1.0053 rad/sec, 1.508 rad/sec, and 2.0106 rad/sec. This input speed corresponds to 10 rpm, 15 rpm, and 20 rpm those remain from the low-side to high-side operating range during its low-speed to high-speed operations. This generates over one full revolution on the output of the gears. The three outputs were plotted and used to generate the FFT for acceleration in the frequency domain. These plots are shown as Fig. 6.1 to Fig. 6.8.

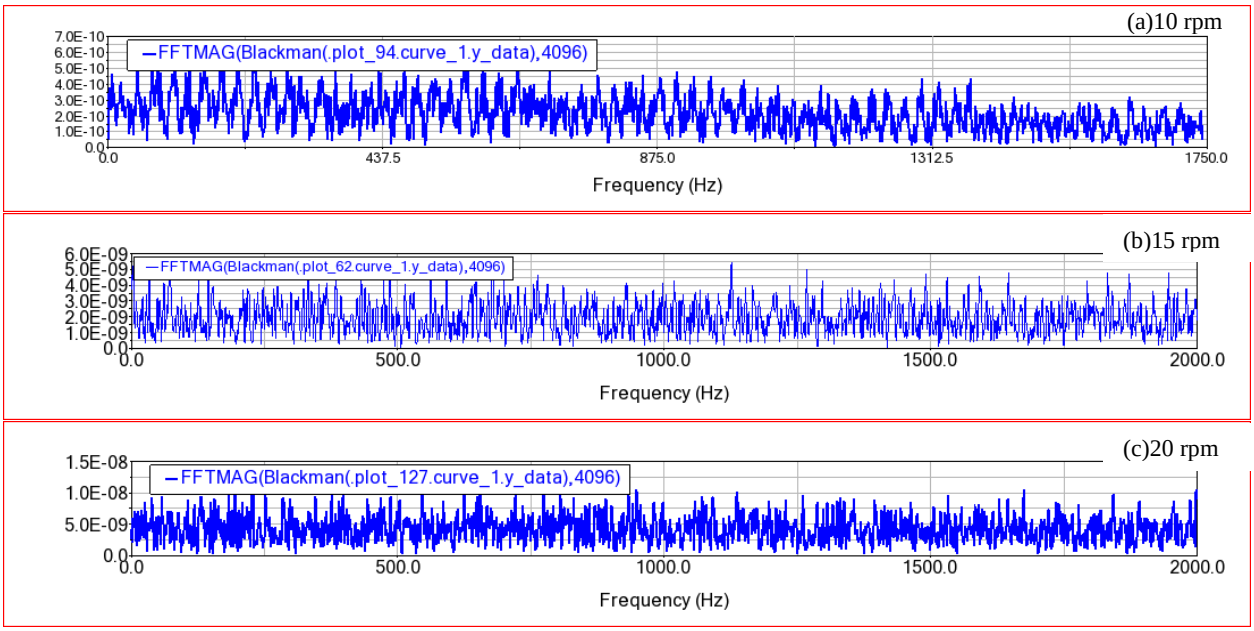

Figure 6.1 Record of a frequency spectrum by the number of revolutions for gear 1

It can be seen in Fig. 6.1 on the above results that it can be hypothesized that the higher the input shaft revolutions, the higher the amplitude in the frequency spectrum. The larges peak occurs at the highest input rotational speed. These were all also calculated from the carrier input speed of

1.0053 rad/sec, 1.508 rad/sec, and 2.106 rad/sec multiplied by the number of teeth on the gear 1, 82 teeth, for the first stage speed-up gears in the drive train.

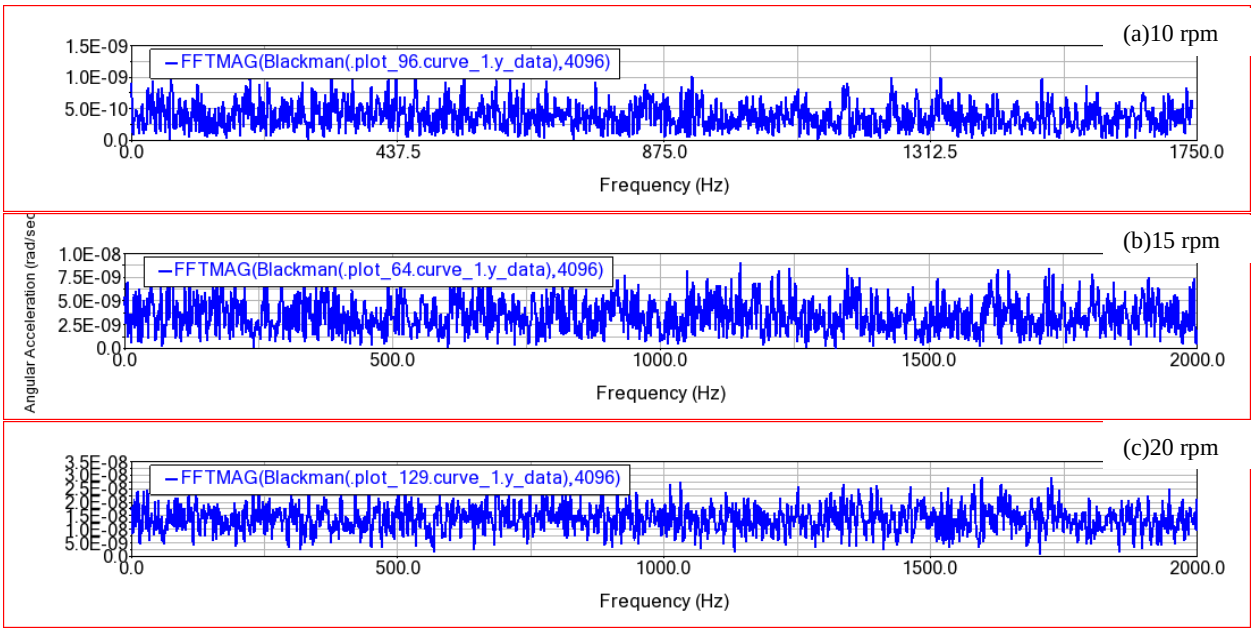

Figure 6.2 Record of a frequency spectrum by the number of revolutions for gear 2

As shown in Fig. 6.2 (a), (b), and (c) the first stage pinion also behaves the same as gear 1. The higher the input speed revolutions, the higher the amplitude in the frequency spectrum. This specific trend is probably the result of the assumption that the higher the number of input speed revolutions, the higher the gearbox oscillation.

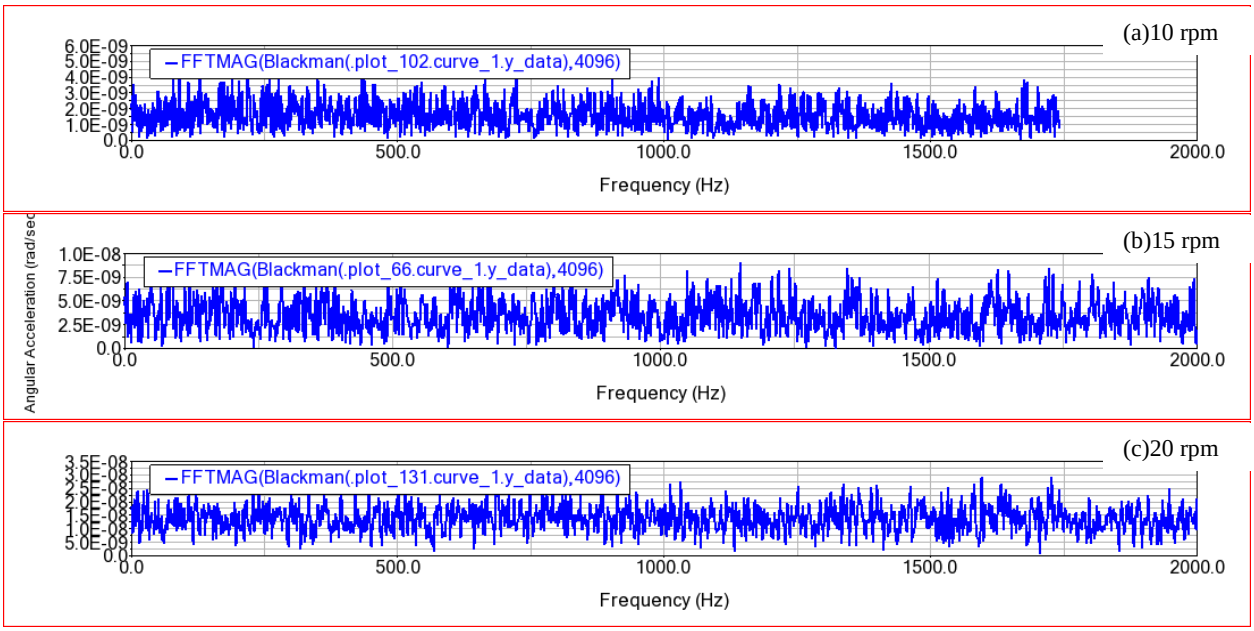

Figure 6.3 Record of a frequency spectrum by the number of revolutions for gear 3

Fig. 6.3 and Fig 6.4 demonstrate frequencies of the vibration pattern generated by such a system at the second speed-up stage of the gearbox. The most significant impact that can be seen visually in figures corresponds to the amplitude change with a change in input rotational speed. As shown in both figures the 20-rpm input speed has the largest peak as well as change in amplitude between the other input speeds.

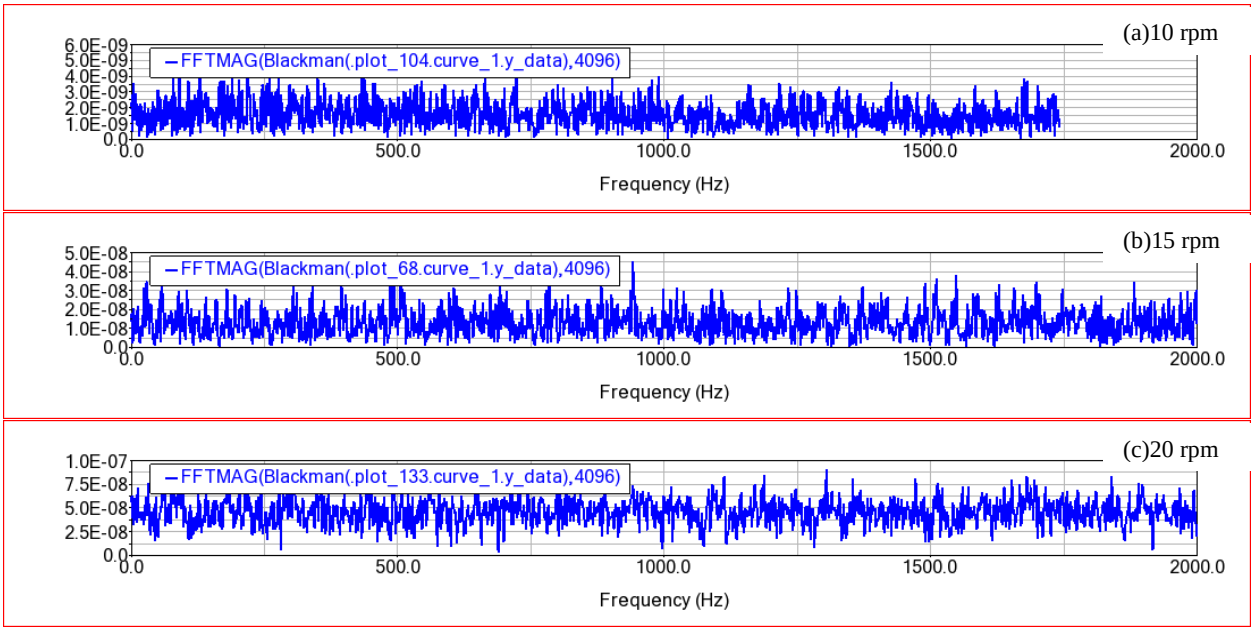

Figure 6.4 Record of a frequency spectrum by the number of revolutions for gear 4

6.3.2 Planetary gear stage vibration analysis

The measurement of gearbox vibration frequency is to simulate an acceleration at each stage on the gearbox system by ADAMS/view. This allows for a measurement of the acceleration of the system over time which can then be input to generate an FFT. Gearbox vibration frequency FFTs can indicate the impact of input rotational speed in the system through a difference in amplitudes. As represented in Fig.6.5 to Fig. 6.8, each different frequency occurrence is associated with a particular input rotational speed difference which includes 10 rpm, 15 rpm, and 20 rpm.

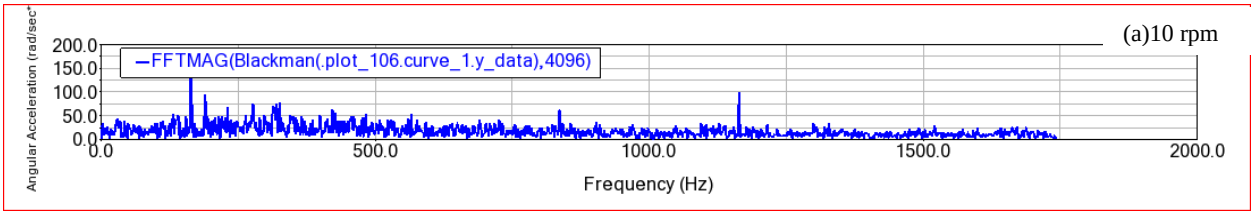

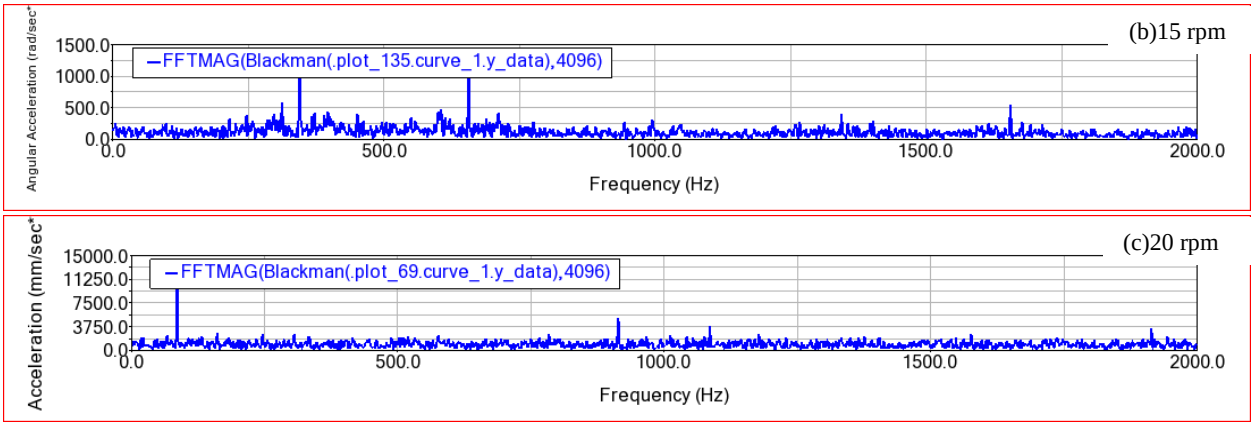

Figure 6.5 Record of a frequency spectrum by the number of revolutions for planet gear 1

Fig. 6.5 shows that the planet gear 1 frequency spectrum at the three different rotational speeds, the higher the input speed revolutions, the higher the amplitude in the frequency spectrum.

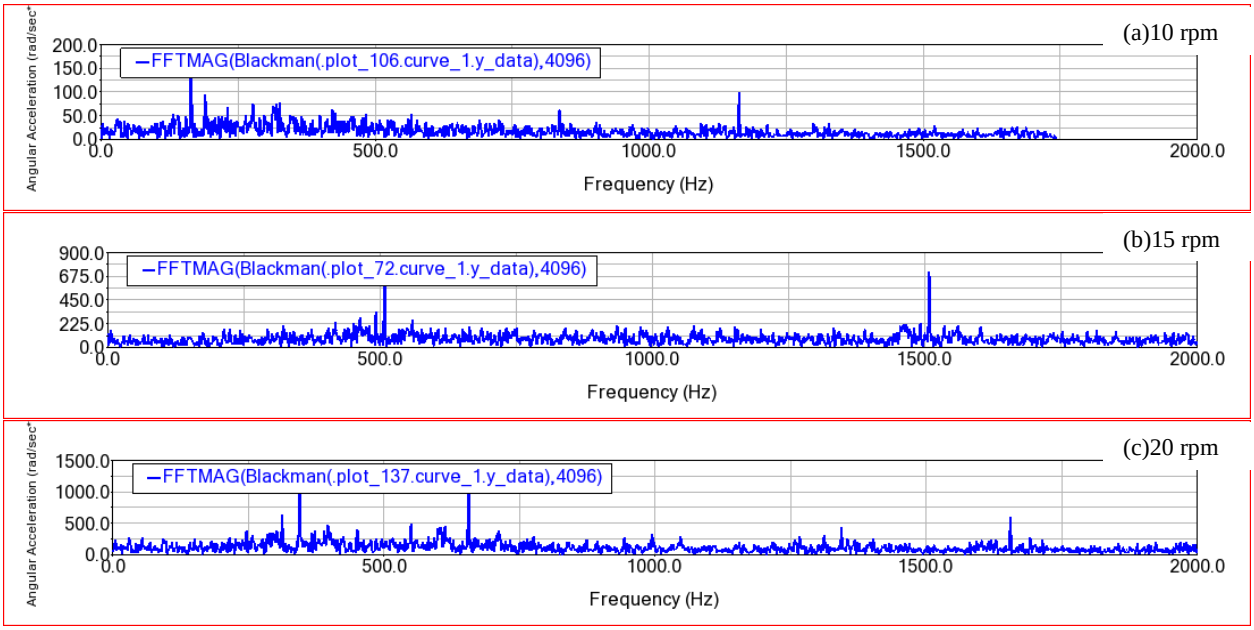

Figure 6.6 Record of a frequency spectrum by the number of revolutions for planet gear 2

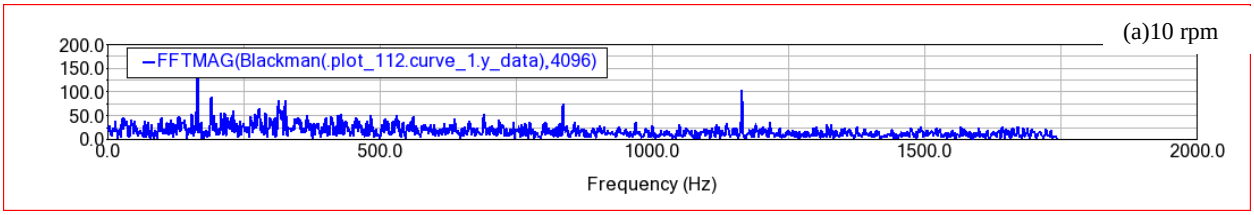

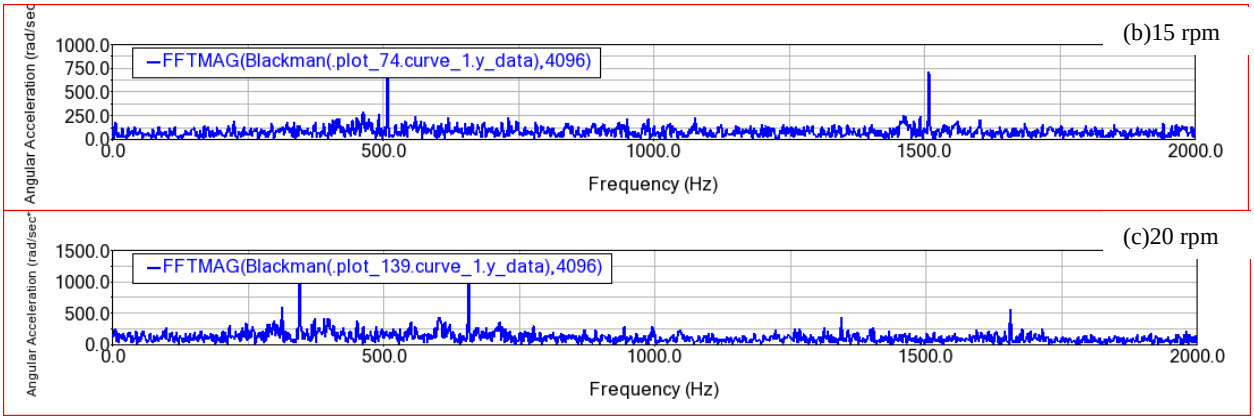

Figure 6.7 Record of a frequency spectrum by the number of revolutions for planet gear 3

As mentioned above the gearbox model was simulated for one-quarter turn on the input over 1000 steps with input speeds of 1.0053 rad/sec, 1.508 rad/sec, and 2.106 rad/sec. These input speeds correspond to 10 rpm, 15 rpm, and 20 rpm. This generates over one full revolution on the sun gear output. The output frequency was plotted and used to generate the FFT for acceleration in the frequency domain. This plot is shown in Fig. 6.8. The largest peak occurs at a higher input speed (20 rpm).

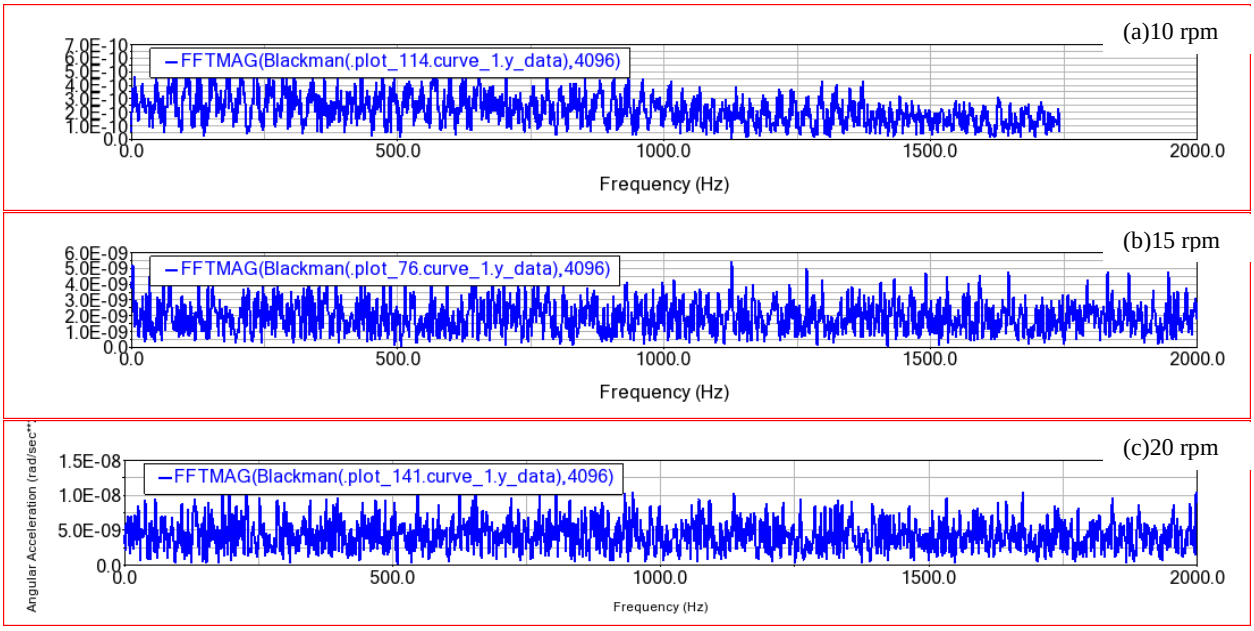

Figure 6.8 Record of a frequency spectrum by the number of revolutions for the sun gear

6.3.3 Summary of the rotational speed variation impact on the angular acceleration of gears

In this section, the dependence of a vibration signal on the number of revolutions is shown in the frequency spectrum by using FFT, the selected three input revolutions are 10 rpm, 15 rpm, and 20 rpm with three cases, τ_3 = 7.54 * 10^5 Nm; τ_1 = 9.549 * 10^5 Nm and τ_2 = 1.432 * 10^6 Nm. The speed variation is performed so that the vibration signature pattern is transformed to the frequency domain for all gears in the drive train.

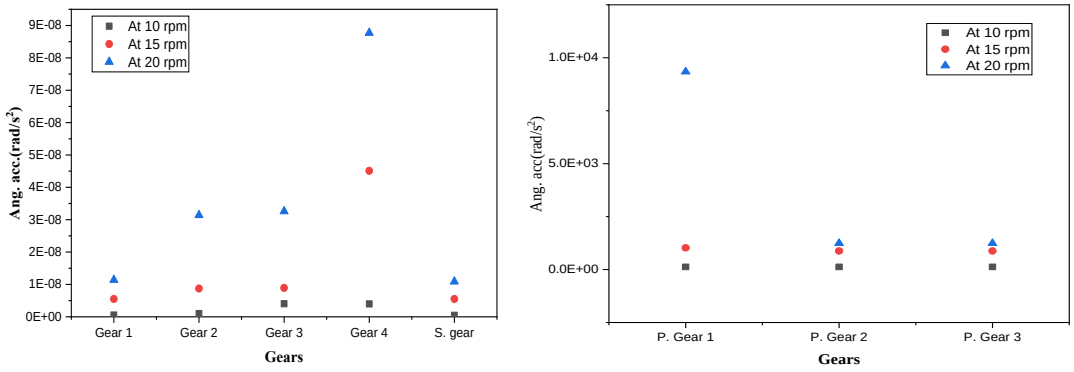

Figure 6.9 Comparison of gears angular acceleration peak points

The speeds selected for these three simulations are within the range of operation of the SE7715. As shown in Fig. 6.9, the angular acceleration vibration signal peak points at 20 rpm have higher amplitudes than other input rotational speeds. At input rotational speed of 10 rpm, the angular acceleration amplitudes are lower. This indicates the vibration signal is dependent on the variation of input rotational speed. As the rotational speed increases the vibrational signal also becomes higher.

6.4 Impact of rotational speed on gear force

6.4.1 Speed-up gear stage

By means of an FFT function on an ADAMS/view the simulated signals are isolated to produce a frequency versus amplitude plot shown as the Fig. 6.10 to 6.13. The practice of FFT in gear condition analysis can be significant since gear contact occurs at specific frequencies unique to the gear system designed. In the simulations used for the following analyses, the FFT plot is created using the contact force between the gears for a specified period. The FFT is used to distinguish the

relationship between the input rotational speed and contact force vibration pattern for the planetary gearbox.

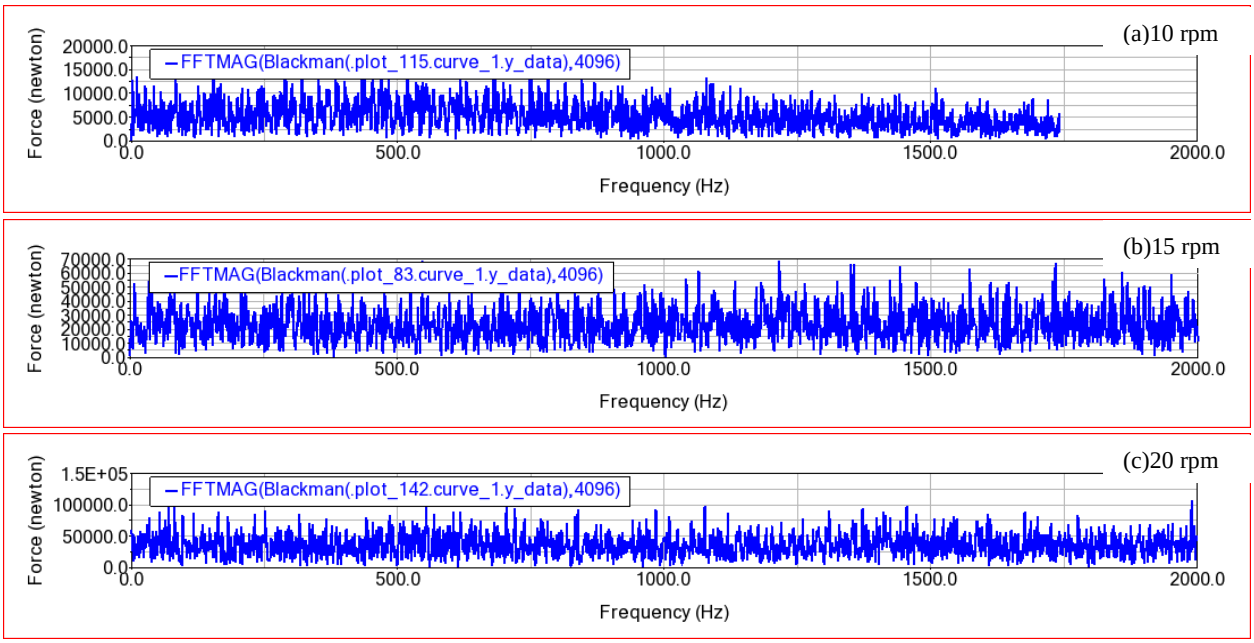

Figure 6.10 Record of a frequency spectrum by the number of revolutions for gear 1

As shown in Fig. 6.10 and 6.11, the first stage gears vibration frequency FFTs can indicate the dependence of rotational speed on the contact force of the system through a difference in amplitudes. Each different frequency occurrence is associated with a particular rotational speed. Based on the first stage figures results, the higher the input shaft revolutions, the higher the amplitude in the frequency spectrum.

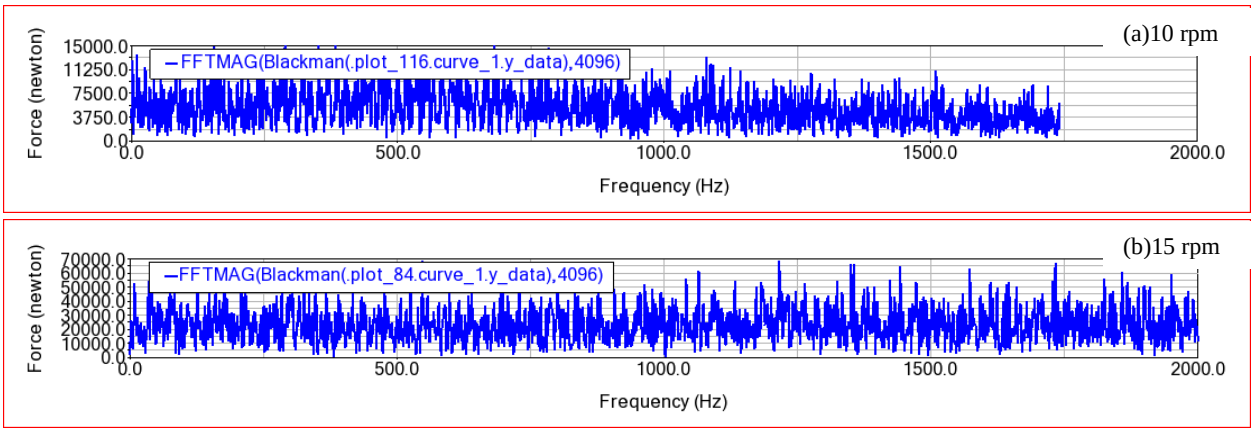

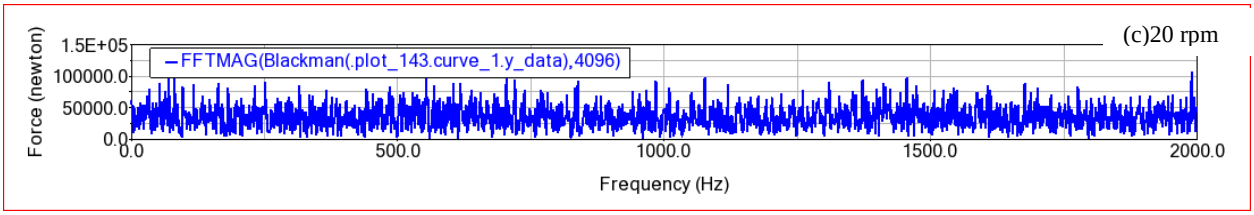

Figure 6.11 Record of a frequency spectrum by the number of revolutions for gear 2

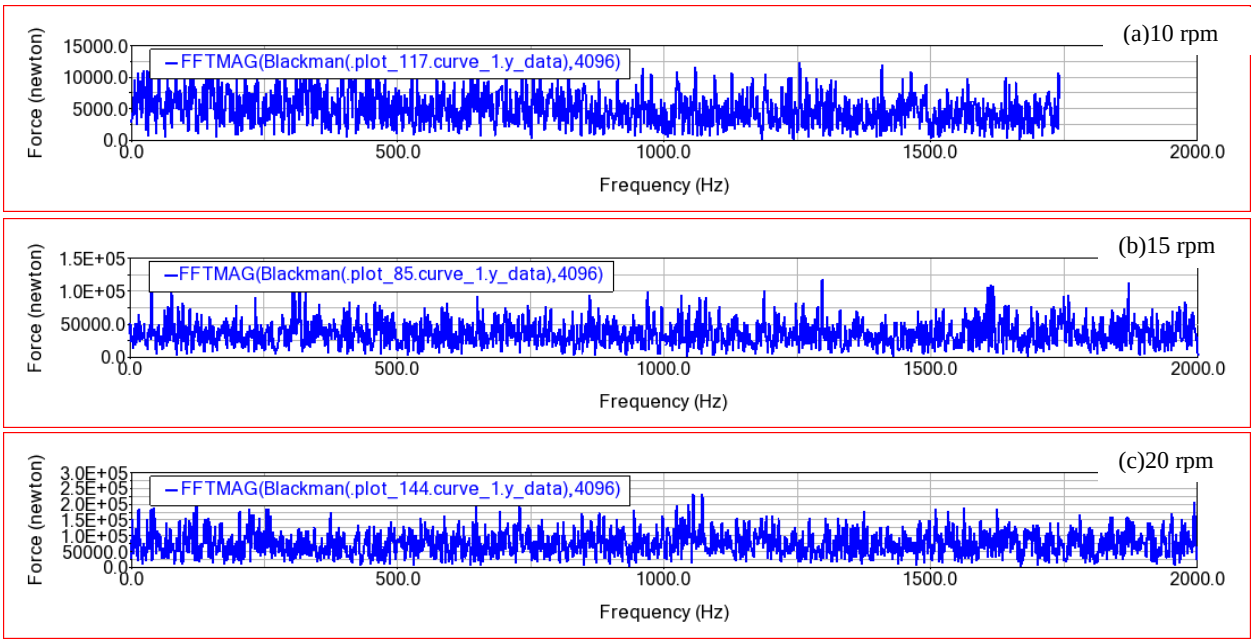

Figure 6.12 Record of a frequency spectrum by the number of revolutions for gear 3

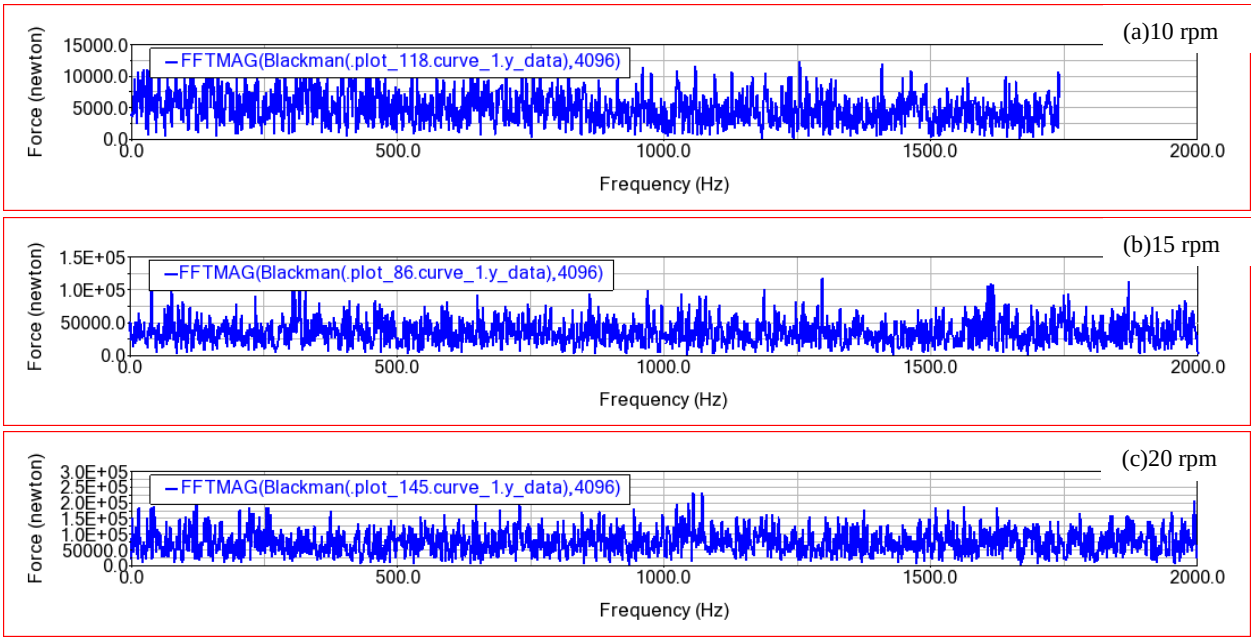

Figure 6.13 Record of a frequency spectrum by the number of revolutions for gear 4

6.4.2 Planetary gear stage vibration analysis

The gearbox model was simulated for one-quarter turn on the input over 1000 steps with input speeds of 1.0053 rad/sec, 1.508 rad/sec, and 2.106 rad/sec. That corresponds with 10 rpm, 15 rpm, and 20 rpm. This generates over one full revolution on the planet and sun gear output. The output force was plotted and used to generate the FFT for force in the frequency domain. These plots are shown in Figs 6.14 and 6.15.

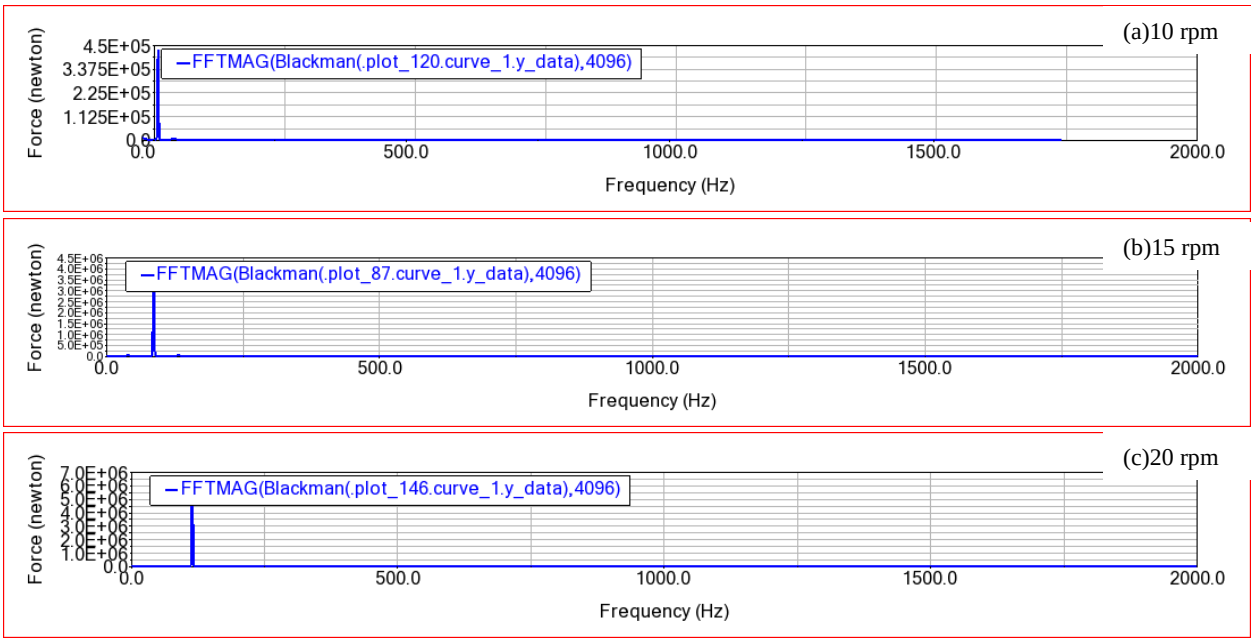

Figure 6.14 Record of a frequency spectrum by the number of revolutions for planet gear 1

It can be seen in Fig. 6.14 that the FFT exhibits a peak at a very specific location throughout the frequency band ranging from 0 to 2000 Hz and the amplitude increases as the input rotational speed increases. The peak occurs at that the expected GMF frequency. The frequencies reveal the vibration pattern created by such a system at the planetary stage of the gearbox. In the case of planet gear 2 and planet gear 3, their frequency spectrum is the same as planet gear 1. The three planet gears FFT contains equal peak points which indicate and are associated with their equal load sharing capacity between them. The planet gear 2 and 3 FFT plot is in Appendix B.

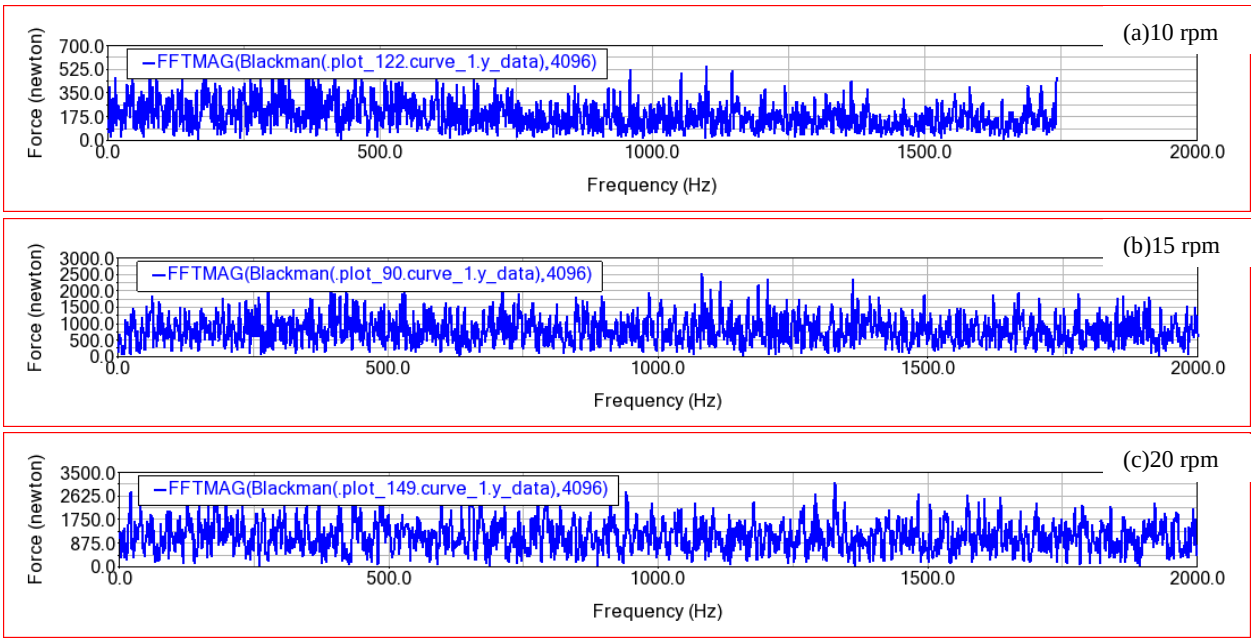

Figure 6.15 Record of a frequency spectrum by the number of revolutions for the sun gear

The input speed at three different simulations corresponds to 10 rpm, 15 rpm, and 20 rpm, those remain on the low to the high-side operating range during its low speed and high-speed operations. This generates over one full revolution on the sun gear output. The output force was plotted and used to generate the FFT for force in the frequency domain. This plot is shown in Fig. 6.15. As depicted in the higher the input shaft revolutions, the higher the force amplitude in the frequency spectrum.

6.4.3 Summary of the rotational speed variation impact on gear force

In this sub-section, the summary of the impact of rotational speed variation on the gear force is discussed in the frequency spectrum. The speeds selected for these three simulations are within the range of operation of the SE7715. A speed of 1.508 rad/sec is equivalent to 15 rpm, this is in the mid operating range of the SE7715. And an input speed of 1.0053 rad/s is equivalent to 10 rpm, this is the initial operating range of the SE7715. An input speed of 2.0106 rad/sec corresponds to 20 rpm which is within one the high end of the operating range during high-speed operations of the SE7715. This number of results is adequate for expressing the dependence.

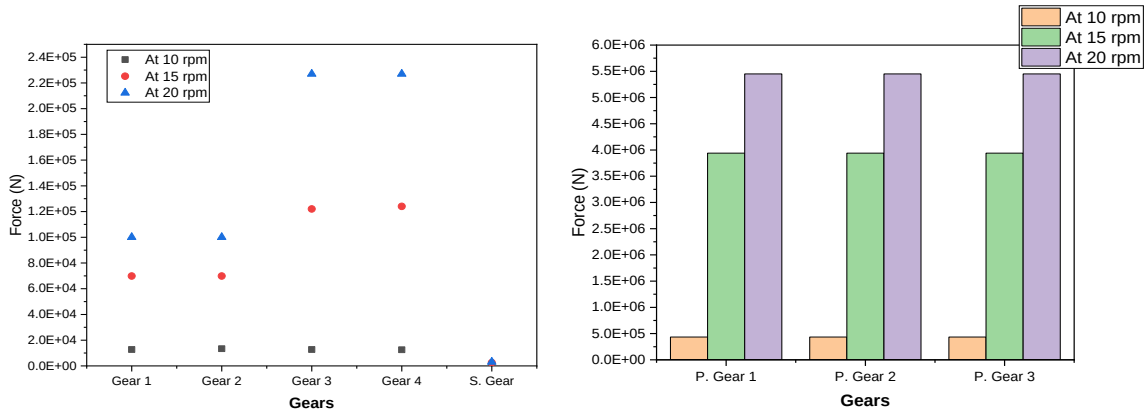

Figure 6.16 Comparison of the impact of rotational speed variation on gear force

As shown in Fig. 6.16, the comparison of the impact of rotational speed variation on gear force is expressed by the selected maximum peak points of gear force on the frequency spectrum. At input rotation of 20 rpm, there are higher maximum peak points than other input rotational speeds (10 rpm and 15 rpm). Therefore, the higher the number of input carrier revolutions, the higher the total gear force on a point of gears.

CHAPTER SEVEN

7. Conclusion and Recommendation

7.1 Conclusion

In this study, the vibration signal of the SE7715 wind turbine gearbox is simulated to monitor the technical conditions of rotating components at three different load cases (at input rotational speeds (10 rpm, 15 rpm, and 20 rpm and torques $\tau_3 = 7.539 * 10^5$ Nm; $\tau_1 = 9.549 * 10^5$ Nm and $\tau_2 = 1.432 * 10^6$ Nm) of Adama wind farm. The gears vibration signal of angular acceleration and gear force are considered in the simulation and the results are analyzed through FFT.

The first process is creating accurate bodies, determining physical values, creating proper motions, setting software for simulation, and presenting the simulation results by using ADAMS. The speed variation is performed and the vibration signature pattern determined for all gears in the drive train. Based on the vibration signal results, at the input speed of 10 rpm, it is recorded the lowest amplitude in time-domain and at the input speed of 20 rpm, there is a higher amplitude in the time-domain. The vibration signal peak points of load case 3 (20 rpm) is greater than load case 2 (10 rpm) and load case 3 (15 rpm), and these cases indicate the vibration signal is dependent on the variation of input rotational speed. As the rotational speed increases the vibrational signal also becomes higher.

The ADAMS is also used to determine the influence of input rotational speed in the gear force at the three load cases. Depending on the simulation results, at the highest input rotation speed (20 rpm), the amplitude of gear force is higher than the other load cases and at 10 rpm input rotational speed, the amplitude is lower than other load cases.

All vibration signals of gears are analyzed by Fourier transform to change the time domain spectrum into frequency domain spectrum. The three sets of simulations in ADAMS were performed at steady-state conditions using an input rotational speed of 10 rpm, 15 rpm, and 20 rpm. As a result of the change in input speed, the GMF of each gear changed accordingly to the expected base GMF for the three systems. At the highest input speed rotation (20 rpm), the recorded force amplitude is higher than the other load cases in the frequency spectrum.

Based on the vibration signal results, it can be concluded that the higher the input speed revolutions of the gearbox, the higher the amplitude in the frequency spectrum. In wind turbines, studying the

dynamic characteristics of the gearbox decreases the pre-failure of the gearbox components. It can help to understand gearbox dynamics. In addition, the study of dynamic characteristics of wind power gearbox works on the prevention of failures in the wind turbine.

7.2 Recommendations

With the methods developed in this thesis, it is hopeful that further research can be conducted into gearbox health monitoring with a variety of different types of conditions and the developed mathematical model can be simulated with other software for further research. The model for the SE7715 gearbox is developed based on specifications of wind turbine with limited information provided, in the expectation of creating a model which can represent the real SE7715 gear system.

Therefore, further works involving more detailed information and validation of the simulation results with real values can improve the developed simulation model. This research work leaves a wide scope for future research work to analyze the dynamic characteristics of wind turbine gearbox. The recommendations for future work include:

- Study the flexible multi-body dynamic analysis of the gearbox and compare the results with this rigid multi-body dynamic analysis.
- Possibility of using the developed mathematical model to simulate with other software for the analysis and compare results.

References

[1] K. T. Megra, “WIND RESOURCE ASSESSMENT AT ADAMA II WIND FARM USING WAsP By : Addis Ababa Institute of Technology School of Industrial and Mechanical Engineering Wind Resource Assessment at Adama II Wind Farm Using WAsP By :,” no. June, 2014.

[2] W. Shi, C. W. Kim, C. W. Chung, and H. C. Park, “Dynamic modeling and analysis of a wind turbine drivetrain using the torsional dynamic model,” *Int. J. Precis. Eng. Manuf.*, vol. 14, no. 1, pp. 153–159, 2013, doi: 10.1007/s12541-013-0021-2.

[3] P. Joris, *Simulation of dynamic drive train loads in a wind turbine*. 2006.

[4] Q. Han, J. Wei, Q. Han, and H. Zhang, *and Vibration Analyses of Gearbox in Wind Turbine*. .

[5] K. Abboudi, L. Walha, Y. Driss, M. Maatar, T. Fakhfakh, and M. Haddar, “Dynamic behavior of a two-stage gear train used in a fixed-speed wind turbine,” *Mech. Mach. Theory*, vol. 46, no. 12, pp. 1888–1900, 2011, doi: 10.1016/j.mechmachtheory.2011.07.009.

[6] H. Plascencia Mora, D. Dąbrowski, and J. Adamczyk, “A multi-body model of gears for simulation of vibration signals for gears misalignment,” *Diagnostyka*, vol. 2, no. 62, pp. 15–22, 2012.

[7] G. Components, “Dynamic Analysis of Wind Turbine Gearbox Components,” 2016, doi: 10.3390/en9020110.

[8] D. Dariusz and A. Natarajan, “Assessment of Gearbox Operational Loads and Reliability under High Mean Wind Speeds,” vol. 80, pp. 38–46, 2015, doi: 10.1016/j.egypro.2015.11.404.

[9] X. Jin, L. Li, W. Ju, Z. Zhang, and X. Yang, “Multibody modeling of varying complexity for dynamic analysis of large-scale wind turbines,” *Renew. Energy*, vol. 90, pp. 336–351, 2016, doi: 10.1016/j.renene.2016.01.003.

[10] H. Dong, C. Zhang, D. Wang, S. Xu, and J. Qiu, “Dynamic characteristics of gear box with PGT for wind turbine,” *Procedia Comput. Sci.*, vol. 109, pp. 801–808, 2017, doi: 10.1016/j.procs.2017.05.331.

[11] C. Zhu, S. Chen, C. Song, H. Liu, H. Bai, and F. Ma, “Dynamic analysis of a megawatt wind turbine drive train †,” vol. 29, no. 5, pp. 1913–1919, 2015, doi: 10.1007/s12206-015-0413-6.

[12] A. R. Nejad, Y. Guo, Z. Gao, and T. Moan, “Development of a 5 MW reference gearbox for offshore,” no. July 2015, pp. 1089–1106, 2016, doi: 10.1002/we.

[13] J. L. M. Peeters, D. Vandepitte, and P. Sas, “Analysis of internal drive train dynamics in a wind turbine,” in *Wind Energy*, Jan. 2006, vol. 9, no. 1–2, pp. 141–161, doi: 10.1002/we.173.

[14] M. Todorov, I. Dobrev, and F. Massouh, “Analysis of Torsional Oscillation of the Drive Train in Horizontal-Axis Wind Turbine,” no. July, pp. 1–3, 2009.

[15] Y. Xing and T. Moan, “Multi-body modelling and analysis of a planet carrier,” 2012, doi: 10.1002/we.

[16] H. Henao and G. A. Capolino, “Planetary Gearbox Effects on Induction Machine in Wind Turbine : Modeling and Analysis,” pp. 1790–1796, 2012.

[17] Z. Li and Y. Chen, “Dynamic Research with Drivetrain Simulation and Modal Analysis of Wind Turbine Gearbox,” vol. 952, pp. 161–164, 2014, doi: 10.4028/www.scientific.net/AMR.952.161.

[18] H. Al-hamadani, T. An, M. King, and H. Long, “System Dynamic Modelling of Three Different Wind Turbine Gearbox Designs under Transient Loading Conditions,” vol. 18, no. 11, pp. 1659–1668, 2017, doi: 10.1007/s12541-017-0194-1.

[19] J. Helsen, F. Vanhollebeke, B. Marrant, D. Vandepitte, and W. Desmet, “Multibody modelling of varying complexity for modal behaviour analysis of wind turbine gearboxes,” *Renew. Energy*, vol. 36, no. 11, pp. 3098–3113, 2011, doi: 10.1016/j.renene.2011.03.023.

[20] C. Zhu, S. Chen, H. Huang, and G. Li, “Dynamic analysis of the drive train of a wind turbine based upon the measured,” vol. 28, no. 6, pp. 2033–2040, 2014, doi: 10.1007/s12206-014-0403-0.

[21] H. Zhai, C. Zhu, C. Song, H. Liu, G. Li, and F. Ma, “Dynamic modeling and analysis for

transmission system of high-power wind turbine gearbox †," vol. 29, no. 10, pp. 4073–4082, 2015, doi: 10.1007/s12206-015-0901-8.

[22] M. Zhao and J. C. Ji, "Nonlinear torsional vibrations of a wind turbine gearbox," pp. 1–23, 2015, doi: 10.1016/j.apm.2015.03.026.

[23] P. Yi, C. Zhang, L. Guo, and T. Shi, "Dynamic modeling and analysis of load sharing characteristics of wind turbine gearbox," 2015, doi: 10.1177/1687814015575960.

[24] J. Tan, C. Zhu, C. Song, and X. Xu, "Study on the dynamic modeling and natural characteristics of wind turbine drivetrain considering electromagnetic stiffness," vol. 134, pp. 541–561, 2019, doi: 10.1016/j.mechmachtheory.2019.01.015.

[25] T. Bruce, H. Long, and R. S. Dwyer-joyce, "Dynamic modelling of wind turbine gearbox bearing loading during transient events," vol. 9, pp. 821–830, 2015, doi: 10.1049/iet-rpg.2014.0194.

[26] W. Shi, C. Kim, C. Chung, and H. Park, "Dynamic Modeling and Analysis of a Wind Turbine Drivetrain Using the Torsional Dynamic Model," vol. 14, no. 1, pp. 153–159, 2013, doi: 10.1007/s12541-013-0021-2.

[27] S. Ana, "MSC Software Introduces Adams Bearing Advanced Technology Solution for Rolling Bearing Modeling & Simulation," 2011.

[28] MD ADAMS, https://www.mscsoftware.com .

[29] https://www.esi-africa.com/153 MW-adama-wind-farm-grows-ethiopia-renewable-energy-plan/No Title." .

[30] SANY, "SANY Global Handbook,": https://www.sanyglobal.com/handbook/WTG.pdf.

[31] D. Hroncová, M. Binda, P. Šarga, and F. Kičák, "Kinematical analysis of crank slider mechanism using MSC ADAMS/View," *Procedia Eng.*, vol. 48, pp. 213–222, 2012, doi: 10.1016/j.proeng.2012.09.507.

[32] Msc, "Building Models in ADAMS / View," p. 512, 2000, [Online]. Available: http://mme.uwaterloo.ca/~me321/BuildingModles.pdf.

APPENDICES

Appendix A. Creation of gearbox components in ADAMS

Planetary gear

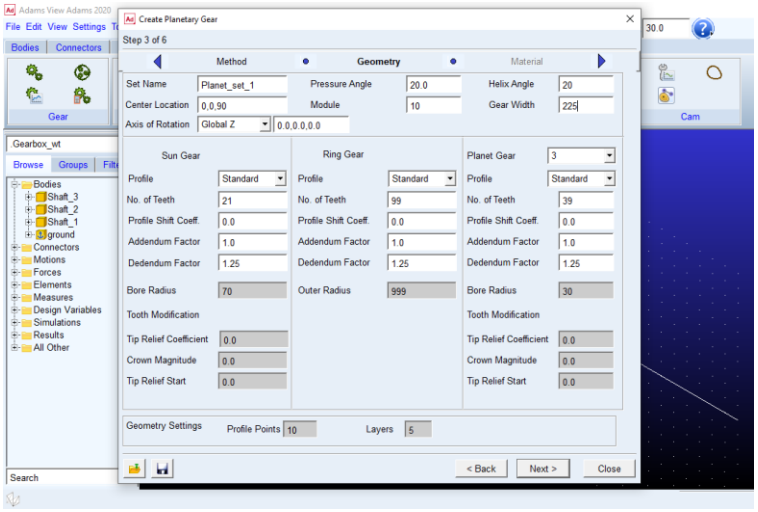

First stage gears

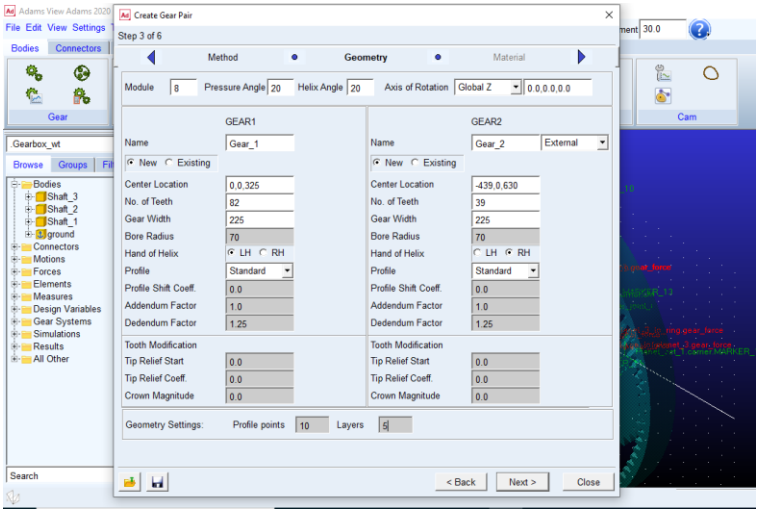

Second stage gears

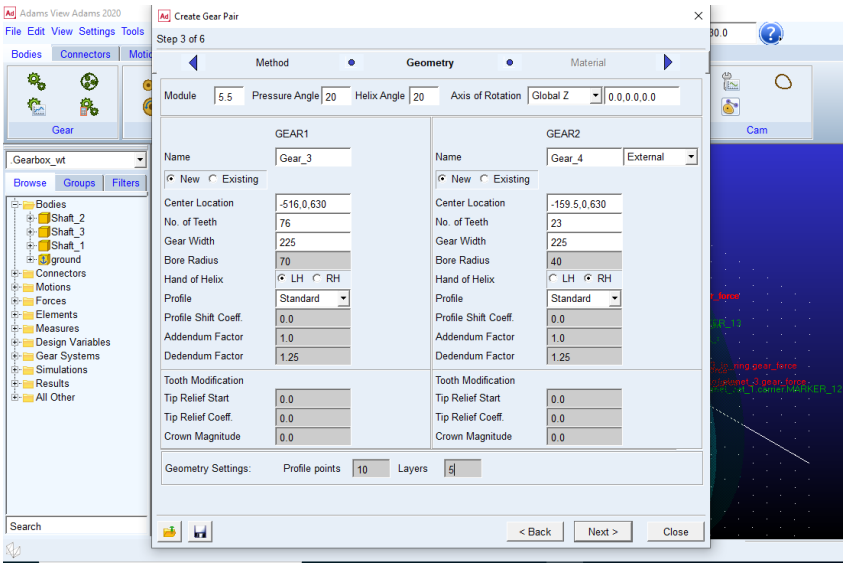

Bearings

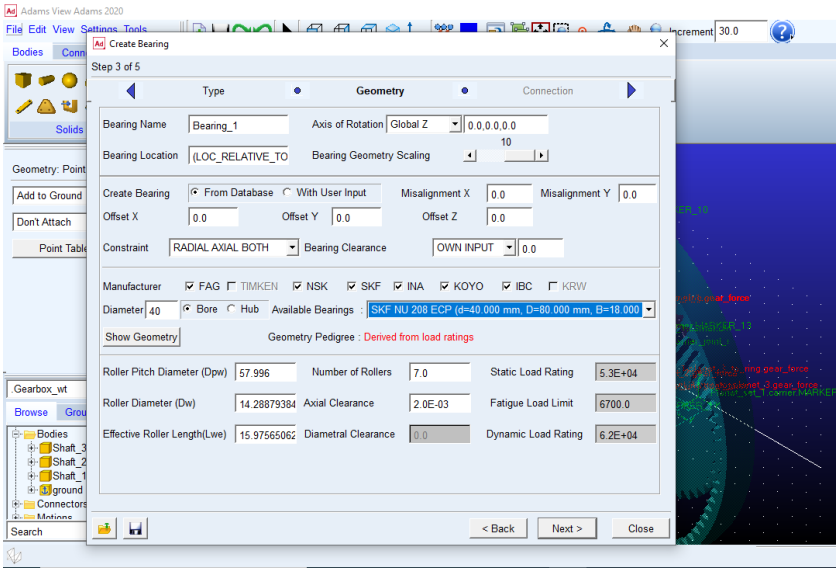

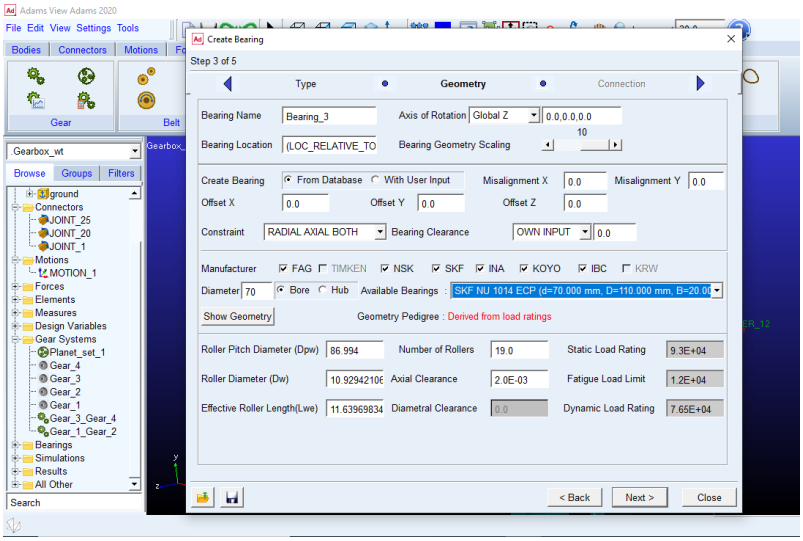
Adams View Adams 2020
File Edit View Settings Tools
Bodies Connectors Motions
Create Bearing
Step 3 of 5
Type Geometry Connection
Bearing Name Bearing_3
Axis of Rotation Global Z 0.0,0.0,0.0
Bearing Location (LOC_RELATIVE_TO
Bearing Geometry Scaling 10
Create Bearing From Database With User Input
Misalignment X 0.0
Misalignment Y 0.0
Offset X 0.0
Offset Y 0.0
Offset Z 0.0
Constraint RADIAL AXIAL BOTH
Bearing Clearance OWN INPUT 0.0
Manufacturer FAG TIMKEN NSK SKF INA KOYO IBC KRW
Diameter 70 Bore Hub
Available Bearings : SKF NU 1014 ECP (d=70.000 mm, D=110.000 mm, B=20.0
Show Geometry
Geometry Pedigree : Derived from load ratings
Roller Pitch Diameter (Dpw) 86.994
Number of Rollers 19.0
Static Load Rating 9.3E+04
Roller Diameter (Dw) 10.9294210
Axial Clearance 2.0E-03
Fatigue Load Limit 1.2E+04
Effective Roller Length(Lwe) 11.63969834
Diametral Clearance 0.0
Dynamic Load Rating 7.65E+04
< Back
Next >
Close

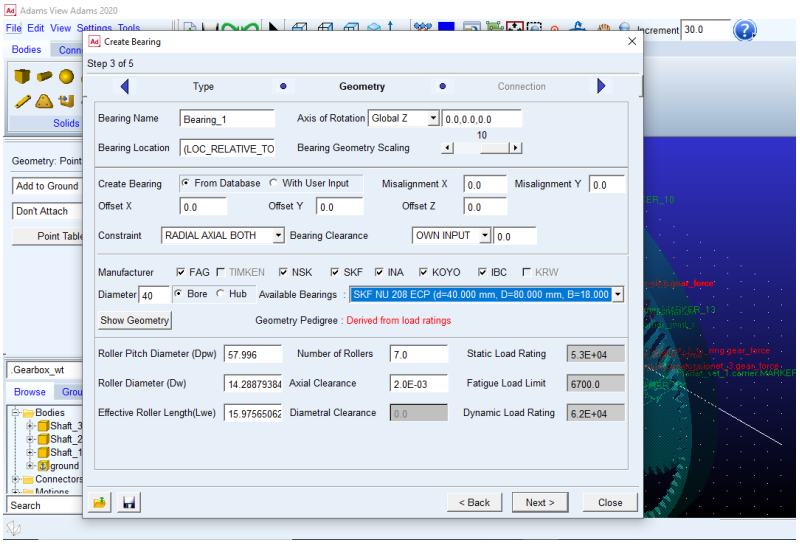
Adams View Adams 2020
Create Bearing
Step 3 of 5
Type Geometry Connection
Bearing Name Bearing_1
Axis of Rotation Global Z 0.0,0.0,0.0
Bearing Location (LOC_RELATIVE_TO
Bearing Geometry Scaling 10
Create Bearing From Database With User Input
Misalignment X 0.0
Misalignment Y 0.0
Offset X 0.0
Offset Y 0.0
Offset Z 0.0
Constraint RADIAL AXIAL BOTH
Bearing Clearance OWN INPUT 0.0
Manufacturer FAG TIMKEN NSK SKF INA KOYO IBC KRW
Diameter 40 Bore Hub
Available Bearings : SKF NU 208 ECP (d=40.000 mm, D=80.000 mm, B=18.000
Show Geometry
Geometry Pedigree : Derived from load ratings
Roller Pitch Diameter (Dpw) 57.996
Number of Rollers 7.0
Static Load Rating 5.3E+04
Roller Diameter (Dw) 14.28879384
Axial Clearance 2.0E-03
Fatigue Load Limit 6700.0
Effective Roller Length(Lwe) 15.97565062
Diametral Clearance 0.0
Dynamic Load Rating 6.2E+04
< Back
Next >
Close

3D model of the geartrain

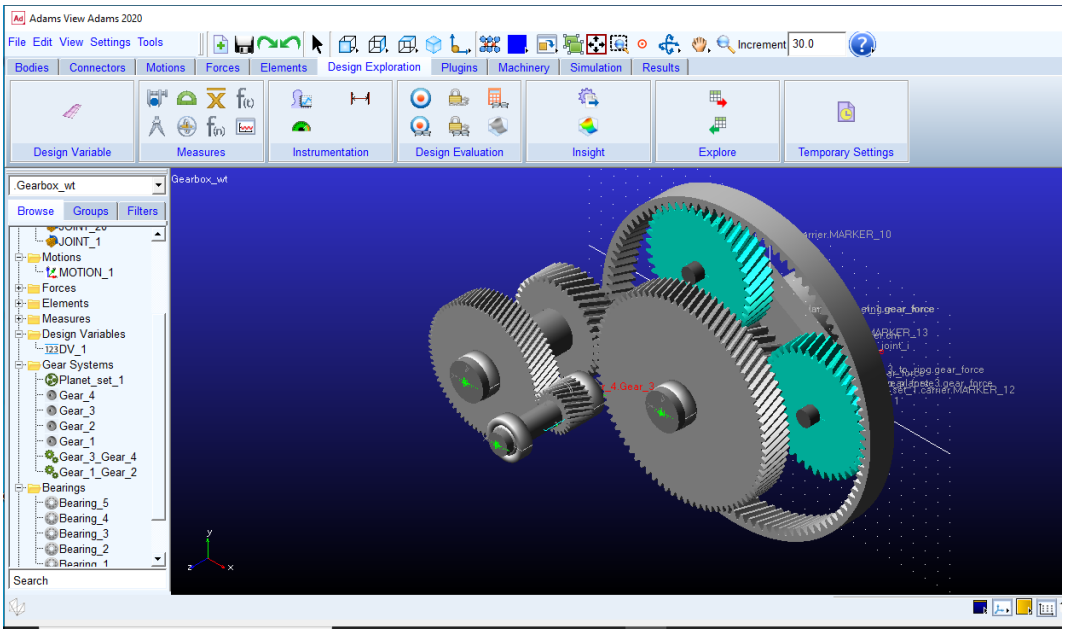

Appendix B. Simulation graphs

1.Record of a frequency spectrum by the number of revolutions for planet gear 2

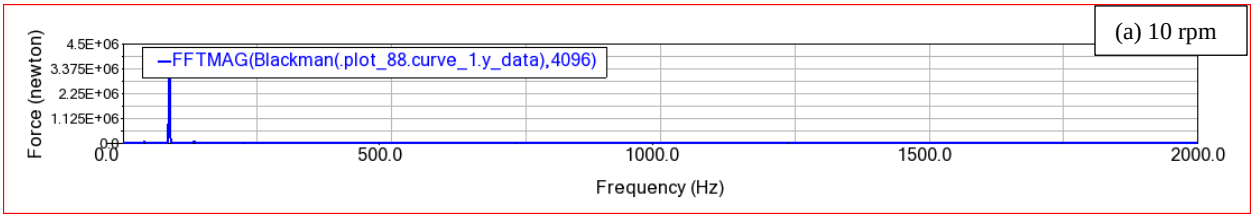

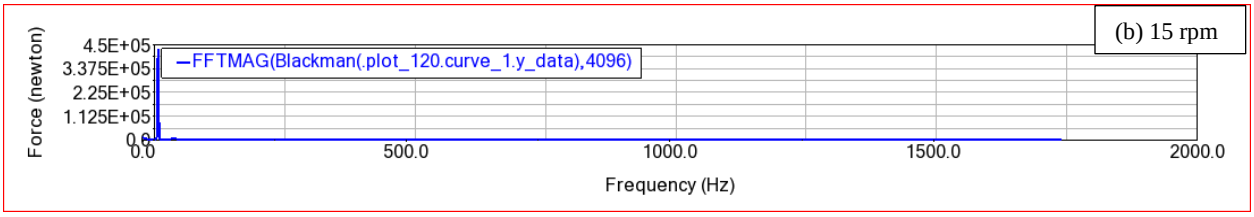

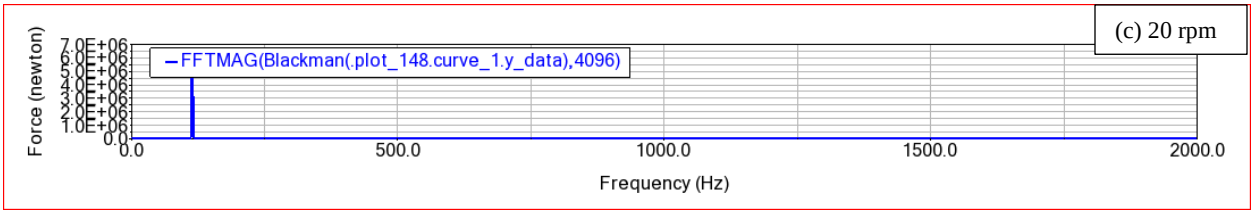

2.Record of a frequency spectrum by the number of revolutions for planet gear 3

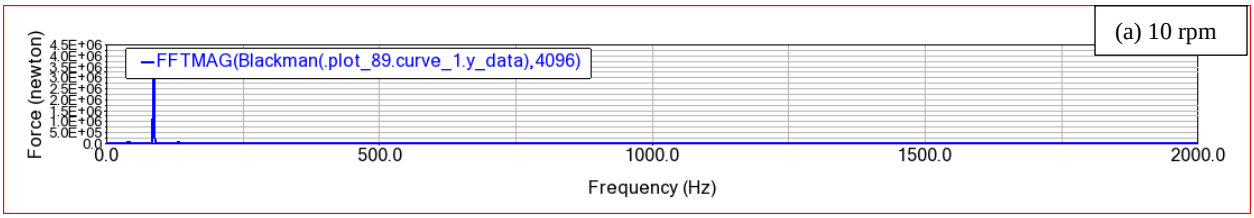

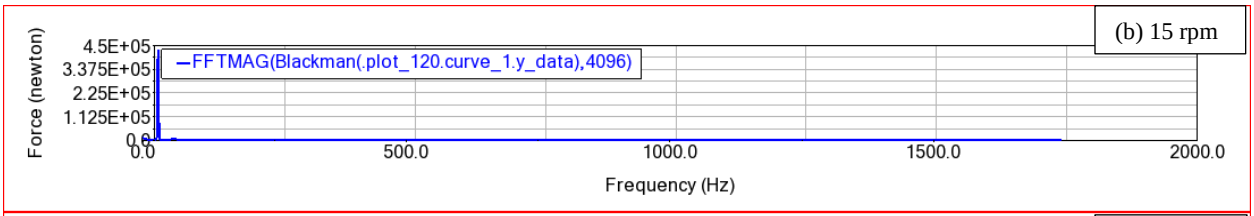
(b) 15 rpm
Force (newton)
4.5E+05
3.375E+05
2.25E+05
1.125E+05
0.0
FFTMAG(Blackman(.plot_120.curve_1.y_data),4096)
0.0
500.0
1000.0
1500.0
2000.0
Frequency (Hz)

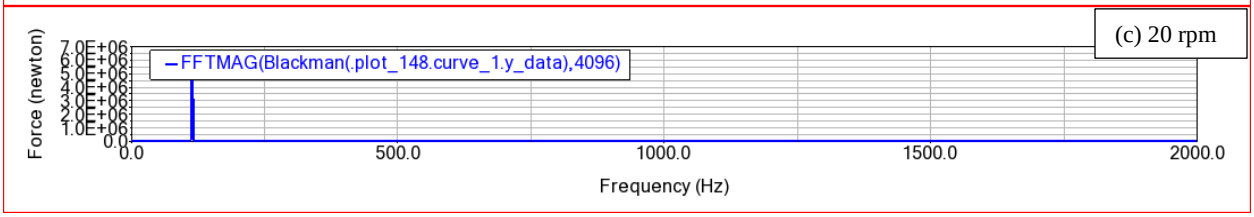
(c) 20 rpm
Force (newton)
7.0E+06
6.0E+06
5.0E+06
4.0E+06
3.0E+06
2.0E+06
1.0E+06
0.0
FFTMAG(Blackman(.plot_148.curve_1.y_data),4096)
0.0
500.0
1000.0
1500.0
2000.0
Frequency (Hz)